

PLUME-RIDGE INTERACTION: SHAPING THE GEOMETRY OF  
MID-OCEAN RIDGES

A DISSERTATION SUBMITTED TO THE GRADUATE DIVISION OF THE  
UNIVERSITY OF HAWAII IN PARTIAL FULFILLMENT OF THE  
REQUIREMENTS FOR THE DEGREE OF

DOCTOR OF PHILOSOPHY

IN

GEOLOGY AND GEOPHYSICS

SEPTEMBER 2008

By  
Eric L. Mittelstaedt

Dissertation Committee:

Garrett Apuzen-Ito, chairperson  
Steve Martel  
Fernando Martinez  
John Sinton  
Marcelo Kobayashi

We certify that we have read this dissertation and that, in our opinion, it is satisfactory in scope and quality as a dissertation for the degree of Doctor of Philosophy in Geology and Geophysics.

DISSERTATION COMMITTEE

---

Chairperson

---

---

---

---

---

## Acknowledgements

First, I would like to thank my advisor, Garrett Ito, for providing numerous hours of discussions, help with problems, someone to bounce ideas off of, paper corrections, and most of all for his consistently positive and supportive attitude. Additionally, I would like to thank the members of my committee for all their help and encouragement over the past few years; Marcelo Kobayashi for insightful comments and discussions; Steve Martel for providing the 2-D boundary element code used in chapter 2 as well as checking my mechanical assumptions; Fernando Martinez for numerous talks during TG's and specifically for discussions about the evolution of the Mariana region; and John Sinton for his insights into the Galapagos and Iceland hotspots. Additionally, I would like to thank R. Hey for discussions on the evolution of the Galápagos Spreading Center, and E. Chapp for insights into the Mariana back-arc system. Maps were made using GMT version 3.4.2 by P. Wessel and W.F. Smith. Funding during work on my dissertation was provided by NSF grants OCE03-7051 and OCE03-51234 and Ito's startup money from SOEST. The computer cluster used for portions of the computations was funded with NSF grant OCE01-36793.

## **Abstract**

Manifestations of plume-ridge interaction are found across the ocean basins. Currently there are interactions between at least 21 hot spots and nearby ridges along 15–20% of the global mid-ocean ridge network. These interactions produce a number of anomalies including the presence of elevated topography, negative gravity anomalies, and anomalous crustal production. One form of anomalous crustal production is the formation of volcanic lineaments between hotspots and nearby mid-ocean ridges. In addition, observations indicate that mantle plumes tend to “capture” nearby mid-ocean ridges through asymmetric spreading, increased ridge propagation, and discrete shifts of the ridge axis, or ridge jumps. The initiation of ridge jumps and the formation of off-axis volcanic lineaments likely involve similar processes and may be closely related.

In the following work, I use theoretical and numerical models to quantify the processes that control the formation of volcanic lineaments (Chapter 2), the initiation of mid-ocean ridge jumps associated with lithospheric heating due to magma passing through the plate (Chapter 3), and the initiation of jumps due to an upwelling mantle plume and magmatic heating governed by melt migration (Chapter 4). Results indicate that lineaments and ridge jumps associated with plume-ridge interaction are most likely to occur on young lithosphere. The shape of lineaments on the seafloor is predicted to be controlled by the pattern of lithospheric stresses associated with a laterally spreading, near-ridge mantle plume. Ridge jumps are likely to occur due to magmatic heating alone only in lithosphere  $\sim 1$  Myr old, because the heating rate

required to jump increases with spreading rate and plate age. The added effect of an upwelling plume introduces competing effects that both promote and inhibit ridge jumps. For models where magmatic heating is controlled by melt migration, repeat ridge jumps are predicted to occur as the plume and ridge separate, but only for restricted values of spreading rate, ridge migration rate, and heating rate. Overall, the results suggest that the combined effect of stresses and magmatism associated with plume-ridge interaction can significantly alter plate geometry over time.

## Table of Contents

Acknowledgments .....	iii
Abstract.....	iv
List of Figures.....	vii
List of Symbols Used .....	ix
Chapter 1: Introduction.....	1
Chapter 2: Volcanic Lineaments.....	4
Chapter 3: Ridge-jumps Associated with Plume-Ridge Interaction.....	41
Chapter 4: Repeat Ridge Jumps.....	73
Appendix A: Elastic Equations along a Curved Mid-Plane.....	119
Appendix B: Governing Equations of Stress Resultants in a Plate of Varying Thickness .....	122
Appendix C: Equations and Benchmarks for Melt Transport Equations.....	124

# **List of Figures**

## **Chapter 1.**

1. Maps of Volcanic Lineaments.....	6
2. Conceptual Model of Volcanic Lineament Formation .....	9
3. Plume Flow and Forces on the Lithosphere .....	15
4. Lithospheric Strength Envelopes and Integrated Plate Strength .....	17
5. Components of the Lithospheric Stress Field Associated with Plume-Ridge Interaction .....	21
6. Model Prediction of Lineament Length versus Plume-Ridge Distance .....	22
7. Predictions of Lineament Length versus the Differential Remote Stress .....	25
8. Interaction of a Plume and a Ridge-Transform-Ridge.....	28
9. Comparison of Stress Trajectories the Galápagos Lineaments .....	33
10. Lineament Observations at 23 Hotspots .....	36

## **Chapter 2**

1. Maps of the Galápagos and Iceland Hotspots .....	42
2. Conceptual Model of Off-Axis Magmatic Heating.....	44
3. Divergence and Lithospheric Thickness .....	50
4. Evolution of Models .....	51
5. Illustration of the Parameters used to Scale Model Results .....	54
6. Model Results and Scaling .....	56
7. The Effect of Heating Zone Width on the Time to Complete a Ridge-Jump .....	58
8. Results for a Migrating Heating Zone .....	61

9. Comparison of Model Results to Galápagos and Iceland .....	64
10. Seafloor and Magma Flux Required to Initiate a Ridge Jump .....	65

### **Chapter 3**

1. Conceptual Model of Plume-Lithosphere Interaction .....	108
2. Model Geometry .....	109
3. Parameters Controlling the Melt Migration and Melt Flux .....	110
4. Evolution of Stationary and Migrating Ridge Jumps.....	111
5. Results and Scaling of Model Results for Cases of Type 1 .....	112
6. Results and Scaling of Model Results for Cases of Type 2 .....	114
7. Plume-Ridge Separation Distance versus Time .....	115
8. Effects of a Hot Upwelling Plume on the Time to Complete a Ridge Jump .....	116
9. Comparison of Observed Ridge Jumps and Model Predictions .....	117

### **Appendix C**

1. Comparison of Analytical and Numerical Solutions of Melt Transport .....	134
2. The Effect of Peclét Number on Melt Flow .....	136
3. The Effect of $L_0$ on Magma Flux through the Lithosphere .....	138
4. The Effect of $S$ on Magma Flux through the Lithosphere .....	139
5. The Effect of $D$ on Magma Flux and Porosity .....	141

## List of Symbols

### Chapter 1

Parameter	Description	Value	Units
$b_i$	total loads on plate	-	N
E	Young's Modulus	$7 \times 10^9$	Pa
$\epsilon_{ij}$	strain	-	-
G	shear modulus	$3 \times 10^{10}$	Pa
h	plate thickness	-	m
$h_p$	plume flow thickness	-	m
$\kappa$	thermal diffusivity	$1 \times 10^{-6}$	$m^2/s$
L	1/2 width of lineament extent along ridge axis	-	m
$N_{ij}$	stress resultants	-	GN/m
$q_s$	load due to plume shear	-	N
$q_g$	load due to gravitational body forces	-	N
q	total load on the plate due to the plume	-	N
r	radial distance from plume center	-	m
$R_p$	radius of radially dominated plume flow	$3.5 \times 10^5$	m
u	velocity of plume spreading	-	m/s
$x_p$	plume-ridge separation distance	-	m
$x_1, x_2, x_3$	coordinate directions	-	-
$\mu$	viscosity	$10^{18} - 10^{19}$	Pa s
$\Delta\rho$	density deficit of plume material	20	$kg/m^3$
$\bar{\sigma}_{ij}$	average stress	-	Pa
v	Poisson's ratio	0.25	-
$\Delta N_f$	$(N_{f11} - N_{f22})$ , far-field differential stress	-	GN/m
$\Delta N_p$	$(N_{p11} - N_{p22})$ , plume differential stress	-	GN/m

## Chapter 2

Parameter	Description	Value	Units
$a$	scaling exponent	2.68	-
$c_p$	specific heat	1000	kJ/kg
$D$	width of lithospheric thinning	-	m
$M$	scaling constant	$3.4 \times 10^{-3}$	$\text{kJ}^{-1.68} \text{m}^{1.68} \text{s}^{1.68}$
$q_{\text{hotspot}}$	hotspot magmatic heating rate at a point	-	$\text{J m}^{-3} \text{s}^{-1}$
$q_{\text{ridge}}$	ridge heating rate at a point	-	$\text{J m}^{-3} \text{s}^{-1}$
$Q_{\text{hotspot}}$	integrated hotspot heating rate	-	$\text{kJ m}^{-1} \text{s}^{-1}$
$Q_{\text{in}}$	heat advected into lithospheric heating zone	-	$\text{kJ m}^{-1} \text{s}^{-1}$
$Q_{\text{out}}$	heat advected out of lithospheric heating zone	-	$\text{kJ m}^{-1} \text{s}^{-1}$
$Q_{\text{ridge}}$	integrated ridge heating rate	-	$\text{kJ m}^{-1} \text{s}^{-1}$
$Q_{\text{thin}}$	integrated advected heating rate at the time of a jump	-	$\text{kJ m}^{-1} \text{s}^{-1}$
$Q_{\text{ratio}}$	ratio of $Q_{\text{in}} - Q_{\text{ridge}}$ to $MQ_{\text{thin}}^a$	0-25	-
$R(t)$	ridge axis divergence rate	0-6	$\text{cm yr}^{-1}$
$t$	time	-	s
$t_{\text{cross}}$	time to cross $D$ at the spreading rate	-	s
$t_{\text{jump}}$	time from the initiation of a hotspot to formation of a ridge jump	-	s
$T$	temperature	-	C
$T_{\text{asth}}$	maximum temperature of asthenosphere	1300	C
$U$	half spreading rate	1-3	$\text{cm yr}^{-1}$
$U_{\text{mig}}$	hotspot migration rate (relative to ridge)	1-3	$\text{cm yr}^{-1}$
$w$	width of magmatic heating zones	2	km
$x$	horizontal coordinate	-50 - 100	km
$\Delta x$	distance from heating zone center (ridge or hotspot)		km
$z$	depth	0-50	km
$z_{\text{crust}}$	depth to the base of the crust	6	km
$z_{\text{max}}$	maximum depth of lithosphere	-	km
$\beta$	magnitude of magmatic heating rate	$(1-44) \times 10^{-10}$	$\text{s}^{-1}$
$\kappa$	thermal diffusivity	$3 \times 10^{-6}$	$\text{m}^2 \text{s}^{-1}$
$\rho$	density of crust, mantle	2900, 3300	$\text{kg m}^{-3}$
$\sigma$	standard deviation of Gaussian describing the variation of heating in the magmatic heating zones	850	m

## **Chapter 3**

Parameter	Description	Value	Units
$A_0$	Constant in the lithospheric permeability	-	Pa
$B_0$	Dimensional sensitivity of lithospheric porosity to magma damage	-	Pa m <sup>-1</sup>
$C_0$	Constant in function of lithospheric porosity	-	-
$c_p$	Heat capacity of mantle at constant pressure	1250	J °C <sup>-1</sup> kg <sup>-1</sup>
$D$	Constant in non-dimensional porosity of the lithosphere	0.625	-
$E$	Activation Energy	180	kJ mol <sup>-1</sup>
$F$	Melt fraction	-	-
$g$	Acceleration of gravity	9.81	m s <sup>-2</sup>
$H_r, H_0$	Time-integrated "reduced" magma flux, reference integrated magma flux	-, 1000	m
$k_0$	Reference permeability	1x10 <sup>-10</sup>	m <sup>2</sup>
$L_0$	Sensitivity of dimensionless lithospheric porosity to damage	0.005	-
$N_0$	Constant in mantle viscosity	-	-
$n$	Exponent on porosity in the permeability	2	-
$P$	Pressure	-	Pa
$Pe$	Peclet number	0.2	-
$Q_{hotspot}, Q_{thin}$	Integrated heating rates	-	J m <sup>-1</sup> s <sup>-1</sup>
$q$	Heating rate at a point due to magma penetrating the lithosphere	-	J m <sup>-3</sup> s <sup>-1</sup>
$S$	Healing rate scale	3x10 <sup>-4</sup>	m <sup>3</sup> s <sup>-1</sup>
$\Delta S$	Entropy change associated with converting a solid to a liquid	200	J K <sup>-1</sup> kg <sup>-1</sup>
$t_{age}$	Age of the lithosphere where a ridge jump occurs	-	Myr
$t_{jump}$	Time between initiation of magmatic heating and completion of a jump	-	Myr
$T$	Temperature	-	°C
$T_{asth}$	Asthenospheric temperature	1300	°C
$\Delta T_p$	Excess plume temperature	300	°C
$u_{rate}$	Half-spreading velocity	10-30	km Myr <sup>-1</sup>
$u$	Melt flux parallel to the solidus	-	m s <sup>-1</sup>
$u_z^s$	Solid vertical velocity	-	m s <sup>-1</sup>
$w_{l0}$	Scale parameter for the melt flux through the lithosphere	1x10 <sup>-14</sup>	m s <sup>-1</sup>
$w_{m0}$	Scale parameter for the melt supply from the mantle	8x10 <sup>-8</sup>	m s <sup>-1</sup>
$w_{mantle}, w_{lith}$	Melt flux from below, melt flux through the lithosphere	-	-
$w_{lith}^{max}$	Maximum melt flux through the lithosphere before a ridge jump	-	-
$w_{l0}/w_{m0}$	Ratio of scale of melt supply from below to scale of lithospheric melt flux	8x10 <sup>4</sup>	-
$x, z$	Horizontal and vertical coordinates	-	m
$x', z'$	Coordinates parallel and perpendicular to the top of the melting region	-	m
$\Delta x$	Distance between initial rifting and the current ridge axis	-	m
$Z_{solidus}, Z_{max}$	Top and bottom depths of the melting region	-	m
$\alpha$	Coefficient of thermal expansion	3.5x10 <sup>-5</sup>	J °C <sup>-1</sup> kg <sup>-1</sup>
$\beta$	Magmatic heating rate scale	(0.9-10)x10 <sup>-5</sup>	m <sup>-1</sup>
$\gamma$	Coefficient of static friction	0.6	-
$\epsilon, \epsilon_p, \epsilon_{crit}$	Strain, accumulated plastic strain, critical strain for weakening equation	-	-
$\dot{\epsilon}_1, \dot{\epsilon}_3$	Maximum and minimum principal strain rates	-	s <sup>-1</sup>
$\eta, \eta^{old}$	Mantle viscosity, viscosity from previous time-step	10 <sup>18-24</sup>	Pa s
$\eta_0$	Reference mantle viscosity	2.2x10 <sup>19</sup>	Pa s
$\mu_m$	Melt viscosity	1	Pa s
$\theta$	Angle of the solidus measured clockwise from the horizontal	-	-
$\kappa$	Thermal diffusivity	3x10 <sup>-6</sup>	m <sup>2</sup> s <sup>-1</sup>
$\rho, \rho_m$	Solid density, melt density	3300, 2800	kg m <sup>-3</sup>

### Chapter 3

Parameter	Description	Value	Units
$\Delta\rho$	Difference between solid and melt densities	500	$\text{kg m}^{-3}$
$\sigma_1, \sigma_3$	Maximum and minimum principal stresses	-	Pa
$\sigma_p, \sigma_{p0}$	Melt pressure beneath the solidus, melt pressure at reference porosity	$-, 2e7$	Pa
$\sigma_{ys}$	Yield stress	-	Pa
$\sigma_{coh}, \sigma_c$	Cohesion in weakening, inherent strength of lithosphere (constant)	-	Pa
$\varphi, \varphi_0, \varphi_{coh}$	Porosity along the solidus, reference porosity, lithospheric strength scale	$-, 0.1$	-
$\varphi_{coh}$	Scaled lithospheric strength	2.2	-
$\Phi, \Phi_{max}$	Characteristic porosity of the lithosphere, maximum lithospheric porosity	-	-
$(dT/dF)_p$	Change in temperature due to a change in melt fraction	850	$^{\circ}\text{C}$

# **Chapter 1**

## **Introduction**

In the mid-1900's, the recognition of seafloor spreading and plate tectonics [e.g. *Hess*, 1962] revolutionized the study of geology and geophysics. Phenomena such as subduction zones, back-arc basins, transform plate boundaries and mid-ocean ridges can now be explained as consequences of the motion of the tectonic plates. However, despite our improved understanding of the nature of plate tectonics, there are still many aspects of these phenomena that are not well understood. The geometry of mid-ocean ridges is one such phenomenon and is the primary focus of this dissertation.

Mid-ocean ridges are one of the most prominent features of the seafloor with a total length of ~70,000 km, but the processes that control their geometry are not well known. Ridges mark the location where two tectonic plates diverge and thus their geometry controls the shape and evolution of the tectonic plates. To first order, they are linear features offset by ridge-perpendicular transform faults, but a closer look reveals that they are offset at almost all spatial scales and show variability in their geometry through time [*Macdonald et al.*, 1988; *Macdonald et al.*, 1991; *Canales et al.*, 1997; *Macdonald*, 1998; *Jones*, 2003]. This variability is likely controlled by several processes. One possibility is that the interaction of a ridge and a nearby hotspot alters the geometry of some ridges through time.

A hotspot is a portion of the seafloor that is anomalously shallow and experiences anomalous volcanism (larger than normal volumes of magma along a ridge or volcanism occurring off-axis). Many hotspots are found on the seafloor near ridges

[e.g. *Jellinek et al.*, 2003]. For some hotspots, the general consensus is that they are the manifestation of an upwelling plume of hot material that passes through the mantle, melts and spreads laterally beneath the lithosphere [e.g. *Morgan*, 1971].

The interaction of mid-ocean ridges and nearby mantle plumes (hotspots) causes numerous changes along the ridge, above the plume, and on the seafloor in between them. Along a hotspot affected ridge, geochemical observations show variations in noble gas and isotope ratios and trace element concentrations [*Hanan et al.*, 1986; *Taylor et al.*, 1995; *Hanan et al.*, 2000; *Keller et al.*, 2000; *Detrick et al.*, 2002; *Ito et al.*, 2003] while geophysical observations find evidence of elevated topography, increased crustal production, and negative gravity anomalies [*Richards et al.*, 1988; *Olson*, 1990; *Sinton and Detrick*, 1992; *White et al.*, 1992; *Ito and Lin*, 1995; *Nadin et al.*, 1995; *Ito et al.*, 2003]. Between the ridge-axis and the plume, there is often excess volcanism in the form of volcanic lineaments [*Morgan*, 1978; *Harpp and Geist*, 2002; *Harpp et al.*, 2003]. Above the plume center, hotspot islands form and often show similar geochemical signatures to those found along the ridge [e.g. *Harpp and White*, 2001]. Plume-ridge interaction is suggested to cause large-scale changes to plate shape and motion through asymmetric spreading [*Muller et al.*, 1998], increased ridge propagation [*Hey*, 1977; *Wilson and Hey*, 1995], and discrete shifts of the ridge axis, or ridge jumps [e.g. *Hardarson et al.*, 1997], but the physical mechanisms behind these changes are yet to be explored.

The primary focus of this dissertation is to examine changes to the geometry of mid-ocean ridges due to mechanisms associated with plume-ridge interaction. To accomplish this, the work was split into three parts. First, to investigate perturbations to

the lithospheric stress field due to plume-ridge interaction, the processes that control the formation of volcanic lineaments are explored. The next chapter examines the initiation of ridge jumps due to lithospheric heating associated with hotspot magma passing through the plate. Finally, chapter 4 investigates ridge jumps due to the effects of a hot, upwelling mantle plume and magmatic heating controlled by melt migration along the top of the melting zone.

## **Chapter 2:**

# **Plume-ridge interaction, lithospheric stresses, and the origin of near-ridge volcanic lineaments**

## **1. Introduction**

### *1.1 Mantle Plume-Ridge Interaction*

A well studied form of magmatic process involves hot spot-ridge interaction. Current interactions between at least 21 hot spots and nearby ridges produce geophysical and geochemical anomalies along 15-20% of the global mid-ocean ridge network [Ito *et al.*, 2003]. Geochemical anomalies show variations in noble gas and isotope ratios and trace element concentrations [Hanan *et al.*, 1986; Taylor *et al.*, 1995; Hanan *et al.*, 2000; Keller *et al.*, 2000; Detrick *et al.*, 2002; Ito *et al.*, 2003; Sinton *et al.*, 2003]. Geophysical observations demonstrate the presence of elevated topography, negative gravity anomalies [Richards *et al.*, 1988; Olson, 1990; Ito and Lin, 1995; Nadin *et al.*, 1995], and anomalous crustal production [Sinton and Detrick, 1992; White *et al.*, 1992; Ito *et al.*, 2003]. Together, these observations not only reveal the importance of hot spot-ridge interaction on the structure and composition of the oceanic lithosphere, but they also support the notion that many of these systems involve interaction with mantle plumes.

Manifestations of plume-ridge interaction are found across the ocean basins. Asymmetric spreading and ridge reorientations at many hot spot-ridge systems including Iceland, Kerguelen, the Galapagos, Shona and Louisville [Small, 1995; Wilson and Hey, 1995; Hardarson *et al.*, 1997] suggest changes in large scale plate

shape and plate motion [Muller *et al.*, 1998]. Also, formation of volcanic lineaments between off-axis hot spot centers and nearby ridges leads to the creation of new islands and seamounts [Harpp and Geist, 2002; Harpp *et al.*, 2003]. The origin of these lineaments is a poorly understood expression of hot spot-ridge interaction and their presence provides an opportunity to extend the general understanding of asthenosphere-lithosphere dynamics.

### *1.2 Near-Ridge Lineaments*

At many hot spot-ridge systems, volcanic lineaments extend from off-axis hot spots to nearby mid-ocean ridges (*Fig. 1*). Examples include Louisville [Lonsdale, 1988; Small, 1995; Vlastelic *et al.*, 1998], Kerguelen [Small, 1995], Reunion [Morgan, 1978; Dymment, 1998], Tristan de Cunha, Musicians [Kopp *et al.*, 2003], the Galapagos [Morgan, 1978; Harpp and Geist, 2002; Harpp *et al.*, 2003; Sinton *et al.*, 2003], the Line Islands (Mid-Pac Mountains), and possibly the Discovery and Shona hotspots [Small, 1995]. Morphologies range from continuous ridges at Rodrigues, Hollister, and Genovesa ridges, to aligned but distinct seamounts and islands at the Wolf-Darwin lineament and Tristan de Cunha. Lineaments show arcuate to nearly linear patterns that, in the cases of Galapagos [Sinton *et al.*, 2003], Kerguelen and possibly the Line Islands (Mid-Pac Mountains) and Tristan, fan out toward ridges from a focus zone near the hot spot (*Fig. 1*). Most lineaments of this type occur on young, weak lithosphere and may be the result of magma exploiting the lithospheric stress pattern associated with plume-ridge interaction [Harpp and Geist, 2002; Harpp *et al.*, 2003; Sinton *et al.*, 2003].

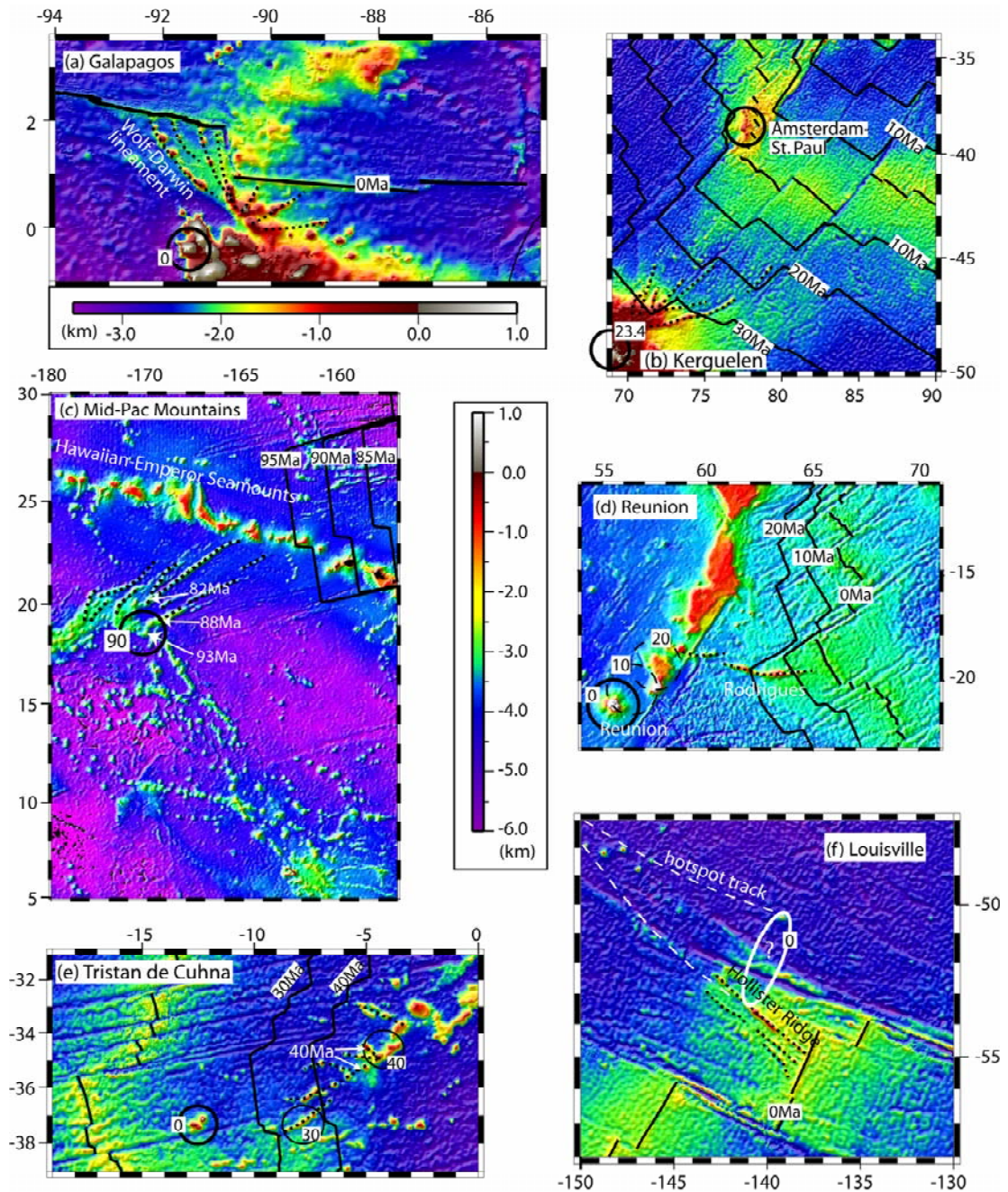


**Figure 1.** (a) Volcanic lineaments are seen at several hot spots including the Galapagos, (b) Kerguelen, (c) Line Islands/Mid-Pacific Mountains, (d) Reunion, (e) Tristan de Cuhna, and (f) Louisville (white dashed lines and ellipse indicate possible hot spot track and current plume center locations). Predicted bathymetry from satellite altimetry [Smith and Sandwell, 1997]. Seamount ages, plume locations and plate reconstructions from Coffin *et al.* [2002], Davis *et al.* [2002], Geli *et al.* [1998], Muller *et al.* [1997], O'Connor and Roex [1992], O'Connor and Duncan [1990], Wessel and Kroenke [1997]. Black circles indicate the approximate center of volcanism at the labeled times (Ma). Seafloor isochrons show approximate mid-ocean ridge geometries

at the labeled times. Plume-ridge separation is the distance between the circles and the ridge at the appropriate age.

### *1.3 Galapagos Lineaments*

Recent studies have focused on the origin and characteristics of off-axis lineaments found near the Galapagos archipelago [Harpp and Geist, 2002; Harpp et al., 2003]. I focus on the Galapagos region because extensive morphological [Sinton et al., 2003], geochemical [Geist et al., 1986; Cullen and McBirney, 1987; Sinton et al., 1996; Geist et al., 1999; Detrick et al., 2002; Harpp and Geist, 2002; Harpp et al., 2003; Schilling et al., 2003], and geophysical investigations [Schubert and Hey, 1986; Feighner and Richards, 1994; Wilson and Hey, 1995; Canales et al., 1997; Ito et al., 1997; Werner et al., 2003] provide better constraints on models of lineament formation than currently possible at other hotspot systems.

A series of approximately seven volcanic chains arrayed in a distinctly fan-shaped pattern, emanate from a focal zone just north of Santiago Island [Sinton et al., 2003] toward the Galapagos Spreading Center (GSC) between  $\sim 92^{\circ}30'W$  and  $89^{\circ}W$  (Fig. 1a). The majority of these volcanic lineaments are concave toward the GSC and curve to meet the ridge at nearly right angles both to the west and east of the large ( $\sim 100$  km offset) transform at  $91^{\circ}W$  [Sinton et al., 2003]. Many researchers have speculated as to the origin of the most prominent of these volcanic chains, the Wolf-Darwin Lineament (WDL). Originally, Morgan [1978] proposed that Wolf and Darwin Islands near Galapagos, and Rodrigues Island near Reunion, are examples of "a second type of hotspot island," formed by an asthenospheric channel connecting the off-axis hotspots to the ridge axis. Enhanced volcanism at the intersection of the channel and

the ridge creates seamounts and islands which are subsequently rafted away by plate motion. This hypothesis predicts that ages along the lineaments should increase away from the ridge, equal to the age of the underlying crust. Volcanic rocks sampled on the WDL, however, do not reveal this simple age progression and lineament ages are 1-5 m.y. younger on the WDL [*White et al.*, 1993; *Sinton et al.*, 1996] and 10-15 m.y. younger on Rogrigues [*Bonneville et al.*, 1988] than *Morgan* [1978] predicts. The gravity analysis of *Feighner and Richards* [1994] suggests that the WDL occurs near the boundary of a discontinuity in effective elastic plate thickness where a lithospheric fault may have occurred allowing magma to reach the surface.

Influence of the 91°W transform fault on lineament formation is suggested by the increasingly transform-parallel lineament trend [*Sinton et al.*, 2003] and decrease in curvature as the lineaments approach the transform. *Harpp and Geist* [2002] and *Harpp et al.* [2003] hypothesize that the WDL and Genovesa ridge are consequences of lithospheric tension associated with the 91°W transform fault along the GSC. The transform model proposed by *Harpp and Geist* [2002], however, predicts a lineament curvature opposite to that observed and increasing curvature near the transform corner (See [*Gudmundsson*, 1995]). Alternatively, *Sinton et al.* [2003], suggest that plate parallel gravitational stresses due to lithospheric uplift from an impinging plume will produce a radial pattern of least tension promoting radial dike orientations [*Ernst and Buchan*, 1997]. This hypothesis predicts the radiating volcanic lineaments to be straight rather than curved and, as noted by *Sinton* [2003], predicts them to radiate from the center of the plume whereas the Galapagos lineaments radiate from an area on the northern edge of the archipelago. Both the prediction of transform induced stresses and

plume induced stresses individually fail to adequately explain the formation of the Galapagos lineaments. I propose that lithospheric stresses due to the combined effects of the plume and segmented ridge can explain the general lineament pattern, focus location, and decreasing curvature near the transform fault.

The goal of this paper is to explore how hot spot-ridge interaction can influence the lithospheric stress field and thus the pattern of volcanic lineaments. This study includes quantitative tests of the hypotheses of *Harpp et al.* [2003], *Harpp and Geist* [2002] and *Sinton et al.* [2003]. I assume that the aforementioned hot spot-ridge systems involve buoyant asthenosphere rising and spreading beneath the lithosphere. In this context I refer to these interactions as “plume”-ridge interactions. I calculate two dimensional (2-D), plan-view, depth-integrated stresses in a plate of varying thickness subject to loads due to plume shear, plate parallel gravitational body forces and boundary tractions along both a straight ridge and a ridge-transform-ridge system. Based on the model results, I address the implications for near, but off-ridge volcanism for the particular case of the Galapagos as well as other oceanic hot spots.

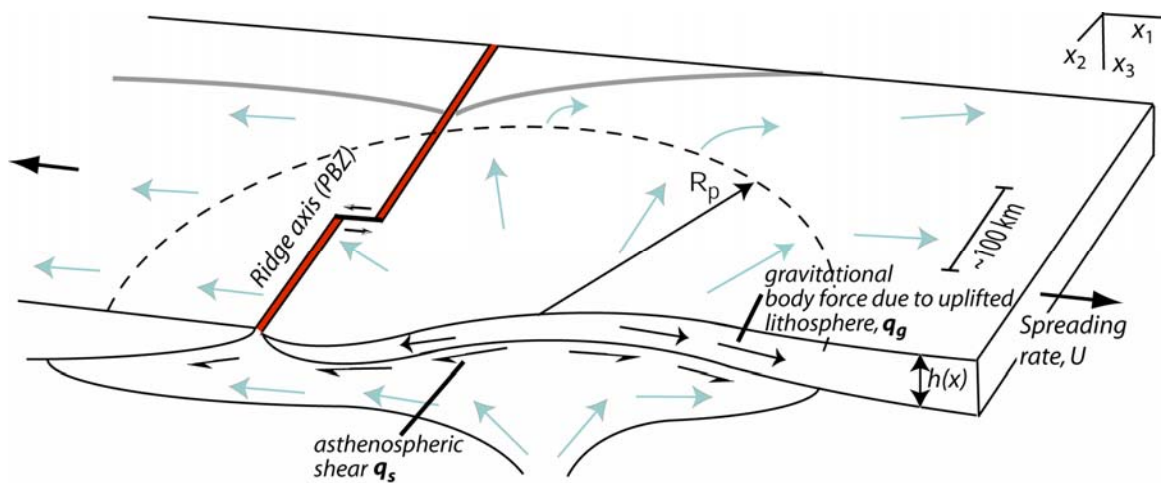


**Figure 2.** Conceptual model. Red line along the ridge axis represents the plate boundary zone (PBZ) of magmatism and non-elastic deformation, with small black

arrows showing sense of motion across the transform fault. Anomalously buoyant (mantle plume) asthenosphere uplifts the plate causing plate parallel gravitational forces ( $\mathbf{q}_g$ ). Large pale blue arrows show flow of buoyant asthenosphere, which introduces shear along the base of the plate  $\mathbf{q}_s$ .  $R_p$  denotes extent over which plume flow is assumed to remain nearly radial. At radii greater than this plume flow deviates due to plate motion. Both plume uplift and asthenospheric shear introduce tension in the plate.

## 2. Conceptual and Mathematical Model

### 2.1 Conceptual Model

Figure 2 illustrates a conceptual model of plume-ridge interaction. I approximate the lithosphere as an elastic plate and treat the zone of rifting near the ridge axis and the region of strike-slip motion along transform faults as an internal boundary subject to normal and shear tractions. I refer to this region of non-elastic deformation along the ridge as the plate boundary zone, PBZ (Figure 2). The stress field in the plate is a function of all body forces and tractions acting on the plate boundaries. These include tractions along the PBZ and the distal plate boundaries, the pull of gravity (which includes the deepening with seafloor age) as well as asthenospheric shear tractions on the base of the plate [Forsyth and Uyeda, 1975]. Indeed the state of stress near mid-ocean ridges varies from region to region, ridge to ridge [Reinecker *et al.*, 2004]. To make these models general and to focus on the local effects of plume-ridge interaction, I treat the effects of all of the distal stresses as a uniform far-field stress and then calculate the perturbations caused by plume-ridge interaction. First, I consider a case of an isotropic far field stress state, with the far-field normal stresses equal in magnitude to the imposed normal tractions (either tensile or compressive) along the plate boundary zone (i.e. the ridge). Ridge-normal compression could be caused by topographic stresses at the ridge axis, while ridge-normal tension could be caused by

seafloor spreading and is evident by extensive normal faulting in the PBZ. Second, I illustrate the effects of a non-isotropic far field stress. Finally, I consider a PBZ stress that is more tensile than the far field isotropic stress.

The stress pattern near a plume-affected ridge will be perturbed by plume-induced stresses. The plume-induced loads on the plate are excess asthenospheric shear ( $\mathbf{q}_s$ , bold terms denote vector quantities), caused by buoyant asthenospheric material (mantle plume) spreading radially beneath the lithosphere, and the pull of gravity ( $\mathbf{q}_g$ ) down the slope of the anomalously uplifted lithosphere [Westaway, 1993]. The combination of these loads creates horizontally varying lithospheric stresses. I assume magma will penetrate the lithosphere and erupt along lineaments perpendicular to the direction of most tensile resultant stress, as integrated through the thickness of the plate.

## 2.2 Mathematical Method

The lateral extent of the lithosphere is large compared to its thickness, therefore, I use thin shell theory to develop the 2-D governing equations of an elastic plate. To describe stresses in the plate I use non-lithostatic, depth-integrated stresses, or stress resultants,  $N_{ij}$ , (see appendix A)

$$N_{ij} = \int_0^h \sigma_{ij} dx_3, \quad (1)$$

( $i, j = 1, 2$  for the lateral directions) where  $\sigma_{ij}$  are stresses throughout the lithosphere,  $h$  is lithosphere thickness, and  $x_3$  is depth in the model where  $x_3 = 0$  is the surface of the plate (Figure 2).

Strictly, the geometry of the lithosphere is a curved “shell” due to the deepening of mantle isotherms with the square-root of distance from the ridge, however, scaling

arguments show that a flat plate (used here) provides a good approximation to this problem (see appendix A). For a flat plate of uniform thickness, static equilibrium is solved by a balance of laterally varying stress resultants,  $N_{ij}$ , and plume-induced loads, which behave mathematically as body forces ( $\mathbf{q} = \mathbf{q}_s + \mathbf{q}_g$ )

$$\frac{\partial N_{ij}}{\partial x_i} + q_j = 0 \quad (2)$$

(summation over  $i$  is implied). The constitutive relation of stress resultants to strain along the mid-plane of the plate ( $\varepsilon_{ij}$ ) is given by *Novozhilov* [1959]

$$\begin{bmatrix} N_{11} \\ N_{22} \\ N_{12} \end{bmatrix} = \begin{bmatrix} Eh(1-\nu^2)^{-1} & Eh\nu(1-\nu^2)^{-1} & 0 \\ Eh\nu(1-\nu^2)^{-1} & Eh(1-\nu^2)^{-1} & 0 \\ 0 & 0 & Eh(1+\nu)^{-1} \end{bmatrix} \begin{bmatrix} \varepsilon_{11} \\ \varepsilon_{22} \\ \varepsilon_{12} \end{bmatrix} \quad (3)$$

where  $E$  is Young's modulus and  $\nu$  is Poisson's ratio (see Table 1 for values used). The compatibility relation is [*Novozhilov*, 1959]

$$(1-\nu) \left[ \frac{\partial^2 N_{11}}{\partial x_2^2} + \frac{\partial^2 N_{22}}{\partial x_1^2} \right] - \nu \left[ \frac{\partial^2 N_{22}}{\partial x_2^2} + \frac{\partial^2 N_{11}}{\partial x_1^2} \right] = 2 \frac{\partial^2 N_{12}}{\partial x_1 \partial x_2} \quad (4)$$

and when combined with (2) yields

$$\nabla^2 (N_{11} + N_{22}) = -\frac{1}{(1-\nu)} \left[ \frac{\partial q_1}{\partial x_1} + \frac{\partial q_2}{\partial x_2} \right]. \quad (5)$$

Lithospheric cooling increases plate thickness,  $h$ , with distance from the ridge, and ridge segmentation introduces age discontinuities across the fracture zones. For laterally varying elastic parameters ( $Eh(x_1, x_2)$ ) the equations of equilibrium and compatibility can be expressed as (see appendix B)

$$\frac{\partial \bar{\sigma}_{ij}}{\partial x_i} + b_j = 0 \quad (6)$$

and

$$(1-\nu)\left[\frac{\partial^2 \bar{\sigma}_{11}}{\partial x_2^2} + \frac{\partial^2 \bar{\sigma}_{22}}{\partial x_1^2}\right] - \nu\left[\frac{\partial^2 \bar{\sigma}_{22}}{\partial x_2^2} + \frac{\partial^2 \bar{\sigma}_{11}}{\partial x_1^2}\right] = 2\frac{\partial^2 \bar{\sigma}_{12}}{\partial x_1 \partial x_2}, \quad (7)$$

respectively. Combining (6) and (7) yields the single governing equation

$$\nabla^2(\bar{\sigma}_{11} + \bar{\sigma}_{22}) = -\frac{1}{(1-\nu)}\left[\frac{\partial b_1}{\partial x_1} + \frac{\partial b_2}{\partial x_2}\right]. \quad (8)$$

In (6) – (8),  $\bar{\sigma}_{ij}$  ( $= N_{ij}/h$ ) are depth-averaged stresses and  $b_i$  are the combined loads due to uplift and plume shear,  $\mathbf{q}$ , as well as “fictitious” body force terms arising due to lateral changes in  $h$  (see appendix B)

$$b_i = \frac{q_i}{h} + \frac{\partial h}{\partial x_j} \frac{\bar{\sigma}_{ij}}{h} \Big|_{i \neq j} + \frac{\partial h}{\partial x_i} \frac{\bar{\sigma}_{ii}}{h}. \quad (9)$$

The form of equations (6) – (8) is identical to the form of the equations of plane stress and allows solutions to be found using an Airy stress function formulation. The plane stress approximation requires that  $\sigma_{33} = \sigma_{13} = \sigma_{23} = 0$ . Here, we examine non-lithostatic, depth-averaged stresses for which, in steady state,  $\sigma_{33}=0$ . Additionally, although plume spreading introduces shear tractions on the base of the plate, we restrict our attention to their effect on depth-averaged normal stresses parallel to the plate.

At straight ridge axes, lithospheric thickness is assumed to vary only perpendicular to the ridge and as such, the fictitious body forces will only include terms with gradients of  $h$  in the ridge normal direction ( $x_1$ ). Near a transform, gradients in thickness parallel and perpendicular to the ridge axis will exist. Though (8) and (9) are formulated in terms of mean stress,  $\bar{\sigma}_{ij}$ , I will show results in terms of depth integrated stresses, or stress resultants,  $N_{ij}$ .

### 2.3 Plume Forces, Lithospheric Strength, and Plate Boundary Conditions

In this model, loads are introduced by the buoyant plume asthenosphere and along the ridge PBZ. These loads perturb the local stress pattern. The loads introduced by the plume on the lithosphere,  $\mathbf{q}$ , include plume shear (treated as introducing a plate-parallel load within the plate),  $\mathbf{q}_s$ , and the plate-parallel pull of gravity due to plate uplift,  $\mathbf{q}_g$ . In order to calculate  $\mathbf{q}$ , I approximate the plume spreading beneath the plate as an axisymmetric viscous gravity current.

The flow of plume material near a ridge is controlled by plate-driven corner flow, gravity-driven plume expansion and flow along the slope of the lithosphere [*Ribe*, 1996]. For simplicity, I restrict consideration to the axisymmetric buoyant “self spreading” term of the equation described by *Ribe* [1996]. Thus the radius of the plume is not the full extent of the plume beneath the lithosphere or along the ridge axis, but the region where axisymmetric flow dominates (Figure 2). Outside of this radial zone, plume flow departs from axisymmetry, but the flow is slower than in the radial zone and is not considered here.

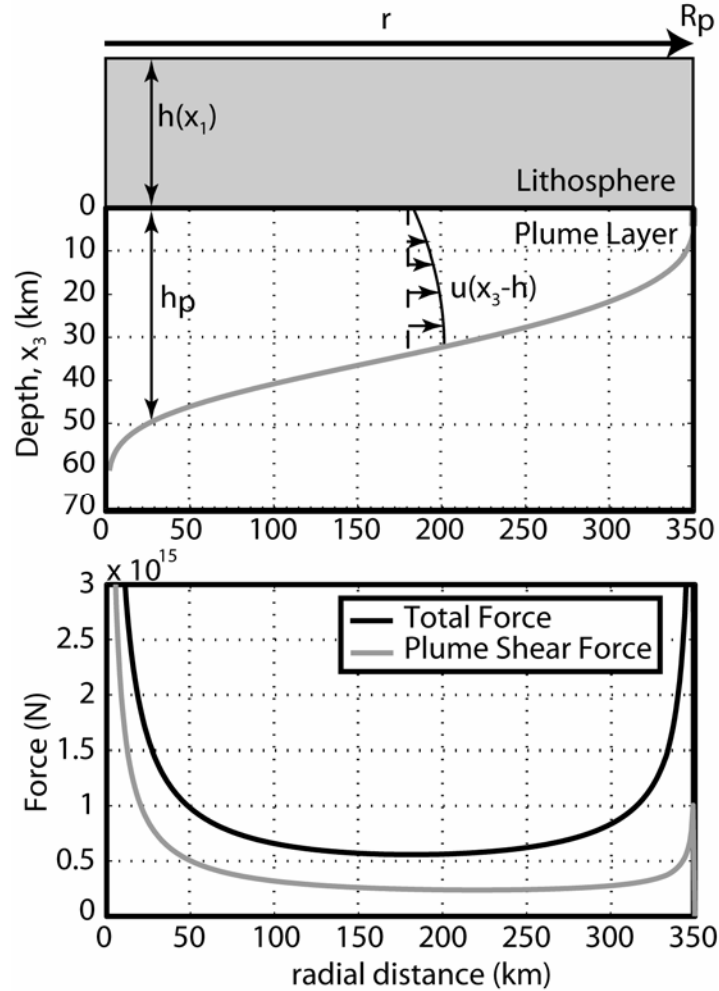


**Figure 3.** (top) Cross sectional view of the model plume flow beneath the lithosphere (here sketched with constant thickness). Velocity with depth in the plume is zero immediately beneath the lithosphere and increases to 10's of cm/yr at the base of the plume layer. (bottom) On average the plume shear force ( $q_s$ , gray; directed to the right) is approximately 40% of the total force ( $q$ , black; directed to the right) exerted on the lithosphere due to plume shear and uplift. Large forces at  $r = 0$  and  $r = R_p$  are consequences of theoretical singularities in the plume solution and are calculated at these locations using an approximate solution [Huppert, 1982].

To compute  $q_s$  I must determine the vertical velocity gradient of plume-flow beneath the lithosphere. Conservation of momentum for a thin layer of fluid yields the solution for radial flow,  $u$ , as a function of radial distance from the center of the flow,  $r$ , and depth below the lithosphere ( $x_3 - h$ ) [Huppert, 1982]

$$u(r, x_3) = -\frac{1}{2} \frac{\Delta\rho g}{\mu} \frac{\partial h_p}{\partial r} (x_3 - h) [2h_p - (x_3 - h)] \quad (10)$$

where  $g$  is the acceleration due to gravity,  $\Delta\rho$  is the density contrast between the plume and surrounding mantle,  $h_p$  is the thickness of the plume flow and  $\mu$  is dynamic viscosity (Figure 3). The shear along the base of the plate is found to be

$$q_s = \mu \left. \frac{\partial u}{\partial x_3} \right|_{(x_3-h)=0} = -\frac{1}{2} \Delta\rho g \frac{\partial h_p}{\partial r} 2h_p \quad (11)$$

and is proportional to  $(h_p^2)$  (Figure 3). *Huppert* [1982] shows that the equations describing conservation of mass and momentum in a thin layer of fluid can be formulated into a single, second order, ordinary differential equation describing the shape of the flow,  $h_p(r)$  (Eq. 2.25 of *Huppert* [1982]). I solve this equation for  $h_p(r)$  and  $\partial h_p / \partial r$  (in (10) and (11)) using a second-order Runge-Kutta method.

Anomalously buoyant plume material beneath the lithosphere will also produce topographic uplift, and a gravitational force component will parallel the plate slope. If the radius of the plume is large compared to the flexural wavelength, then the height of isostatic topography,  $h_t$ , depends on the product of the plume thickness,  $\Delta\rho$ , and the difference between the mantle density,  $\rho_m$ , and the ocean density,  $\rho_w$ ,

$$h_t = \frac{\Delta\rho}{(\rho_m - \rho_w)} h_p. \quad (12)$$

The plate-parallel gravitational body force due to plate uplift ( $q_g$ ) is proportional to  $h_t$  and the slope of the lithosphere,  $\partial h_t / \partial r$ ,

$$q_g = \frac{\partial h_t}{\partial r} (\rho_l - \rho_w) gh \quad (13)$$

where  $\rho_l$  is lithospheric density. The total plume force is  $q = q_s + q_g$  (Figure 3).

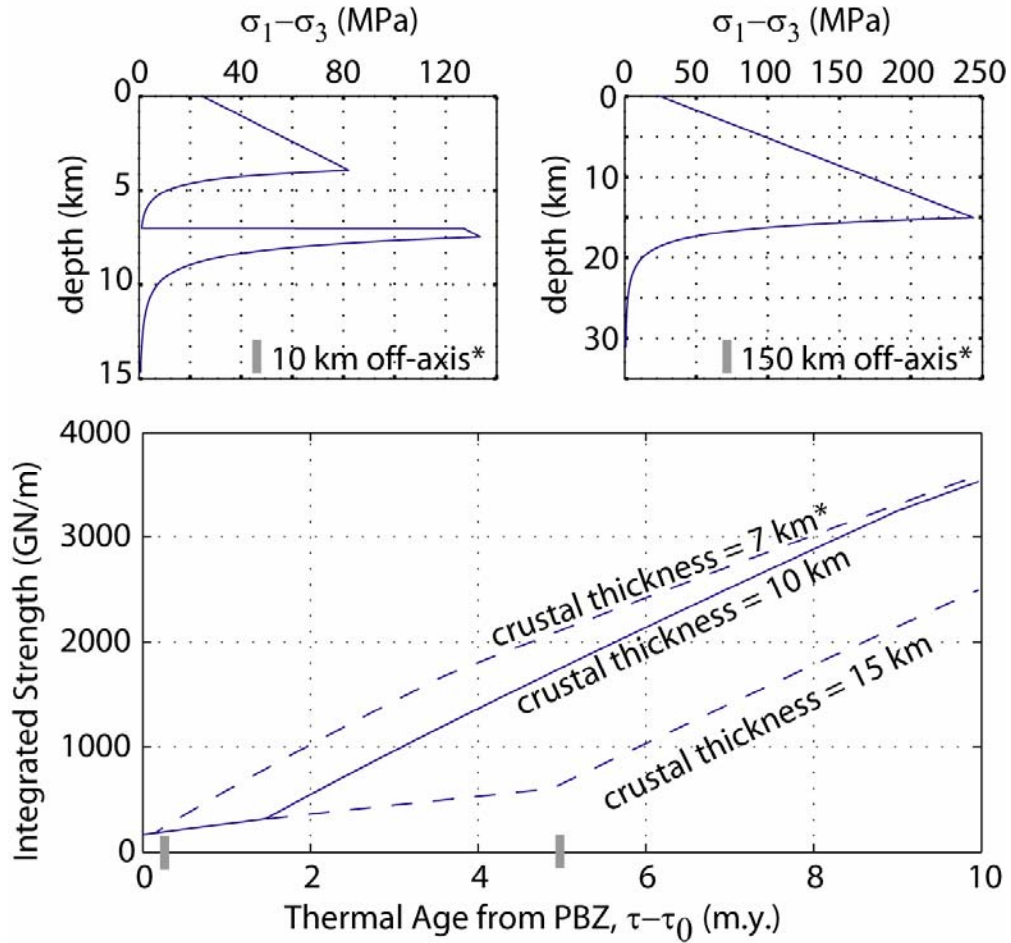


**Figure 4.** (Top) Lithospheric yield envelopes at 10 and 150 km from the ridge axis (grey bars) demonstrate the strength of the lithosphere with depth for a 7-km-thick crust. (bottom) The strength of the lithosphere, calculated by depth-integrating the yield stress envelopes, increases with thermal age  $\tau$  of the lithosphere outside of the PBZ. In young lithosphere, the ductile strength dominates the lower crust, while in older lithosphere, brittle strength is most important. Left side of diagram ( $\tau - \tau_0 = 0$ ) corresponds to the edge of the PBZ, assumed to have cooled as an infinite half space to a thermal age of  $\tau_0 = 0.5$  m.y.

In order to understand the response of the lithosphere to the imposed forces, I calculate depth integrated tensile yield strength (Figure 4). As commonly done, the lithosphere is assumed to behave in a brittle fashion at shallow depths and transition to ductile behavior with depth [Chen and Morgan, 1990; Shaw and Lin, 1996; Buck and

*Poliakov*, 1998]. I assume a two-layer lithosphere with a top layer of basaltic crust having a lower ductile strength than the underlying peridotite mantle [e.g. *Shaw and Lin*, 1996]. Thickening of the lithosphere is controlled by a half-space cooling model [e.g. *Parsons and Sclater*, 1977]. A cooling plate strengthens with age, but like *Small* [1995], I predict the integrated strength to increase gradually at young plate ages ( $< \sim 1.8$  m.y. for a crustal thickness of 10 km), when the crust is supplying most of the strength, and to increase more rapidly at greater plate ages when the mantle begins to supply strength (Figure 4). Another interesting prediction is that thicker crust will produce a weaker lithosphere which, in turn, may influence the maximum plume-ridge separation distance where lineament formation is possible. When including the transform fault in these models, the strength variations due to the age discontinuity across the transform and fracture zone are present for the entire length of the model.

The boundary conditions include imposed stress resultants in the far field and along the ridge axis. The imposed far field (resultant) stresses may be tensile or compressive and are assumed to be caused by all of the loads upon the plate, except by the local forces associated with plume-ridge interaction. The local ridge axis is subject to imposed normal tractions equal to the value of the far field stress perpendicular to the ridge. I assume that extension and accretion in the PBZ prevent any substantial shear tractions on its boundaries and therefore impose a zero shear traction condition at the ridge axis. For a segmented ridge offset by a transform fault, the normal and zero shear stress conditions are identical along both the ridge and transform segments. Although shear may be present along the transform at the Galapagos, it does not significantly affect the model solutions.

## 2.4 Numerical Implementation

Stress resultants are calculated throughout the 2D plate by solving Eq. (8) with the right hand side approximated by point loads. The well known problem of calculating stress in an infinite plate due to a directed point force is known as Kelvin's problem [Timoshenko and Goodier, 1934; Crouch and Starfield, 1987; Barber, 2002]. I use a plane stress solution of Kelvin's problem to calculate the effect of plume shear and uplift at any given point in the model space. By summing Kelvin solutions due to the appropriate forces at each location, I simulate the effect of the whole plume on the lithosphere.

The boundary conditions along the PBZ are implemented using a displacement discontinuity, boundary element model [Crouch and Starfield, 1987]. The boundary elements method is used for effective modeling of crack-like behavior of the ridge. I begin with an idealized case of a straight ridge axis and extend the ridge well beyond the region of interest (i.e. 10 times the plume radius in both directions) to minimize the influence of the ridge ends on the solutions.

With the Kelvin point forces (imposing the loads  $q$ ) and the ridge boundary condition applied, I solve equation (8) using an Airy stress function approach to yield a first approximation to  $N_{ij}$ 's and  $b_i$ 's with the "fictitious" body forces initially set to zero. Achieving the final solution requires several iterations over the whole domain to accurately solve for the "fictitious" body forces due to the varying plate thickness (Eq. 9 and Appendix B). With each successive iteration, the difference between the previous and new stress fields diminishes indicating convergence toward the solution. A solution

is assumed to be sufficiently accurate when the difference between successive iterations is less than 0.1% of the maximum stress in the plate.

### **3. Results**

#### *3.1 Straight Ridge*

To provide an intuitive understanding of the results I show a series of solutions with the different plate loads sequentially added to the models (Figure 5). For each model, I set a plume volume flux of  $90 \text{ m}^3/\text{s}$  [Ribe and Delattre, 1998], a seafloor spreading rate of  $30 \text{ km}/\text{myr}$ , a radius of axisymmetric plume flow of  $350 \text{ km}$ , and a plume density deficit appropriate for a temperature excess from local mantle of  $200 \text{ K}$ . Complete model parameters and variables are described in the list of symbols (page ix). First, I consider a plate with uniform thickness, no ridge axis, zero far field stress and subject only to the shear due to radial plume expansion. Stress resultants due to plume shear alone show a radial pattern of least tensile stress resultant trajectories with most tensile magnitudes being proportional to  $(h_p)^2$  and having a maximum at the plume center (Figure 5a). Trajectories of least tensile stress resultants may control the preferred paths of lateral magma propagation through the lithosphere (e.g., dikes will tend to open in the direction of maximum tension and propagate in the direction normal to that) while stress resultant magnitudes should reflect the ability of magma to penetrate the lithosphere. Plume shear induces  $\sim 40\%$  of the imposed stress due to plume-lithosphere interaction (Figure 3). Figure 5b shows the effects of plume shear combined with the effects of topographic uplift. Plate parallel gravitational body forces due to dynamic topography introduce the remaining  $\sim 60\%$  of the stress resultant

magnitude. The magnitude of plate parallel gravitational forces is proportional to lithospheric thickness and height of uplift (*Eq. 13*). The thinning of the lithosphere toward the ridge axis therefore produces a non-axisymmetric pattern of stress resultants with deviation from the radial pattern greatest where gradients in lithospheric thickness are largest.

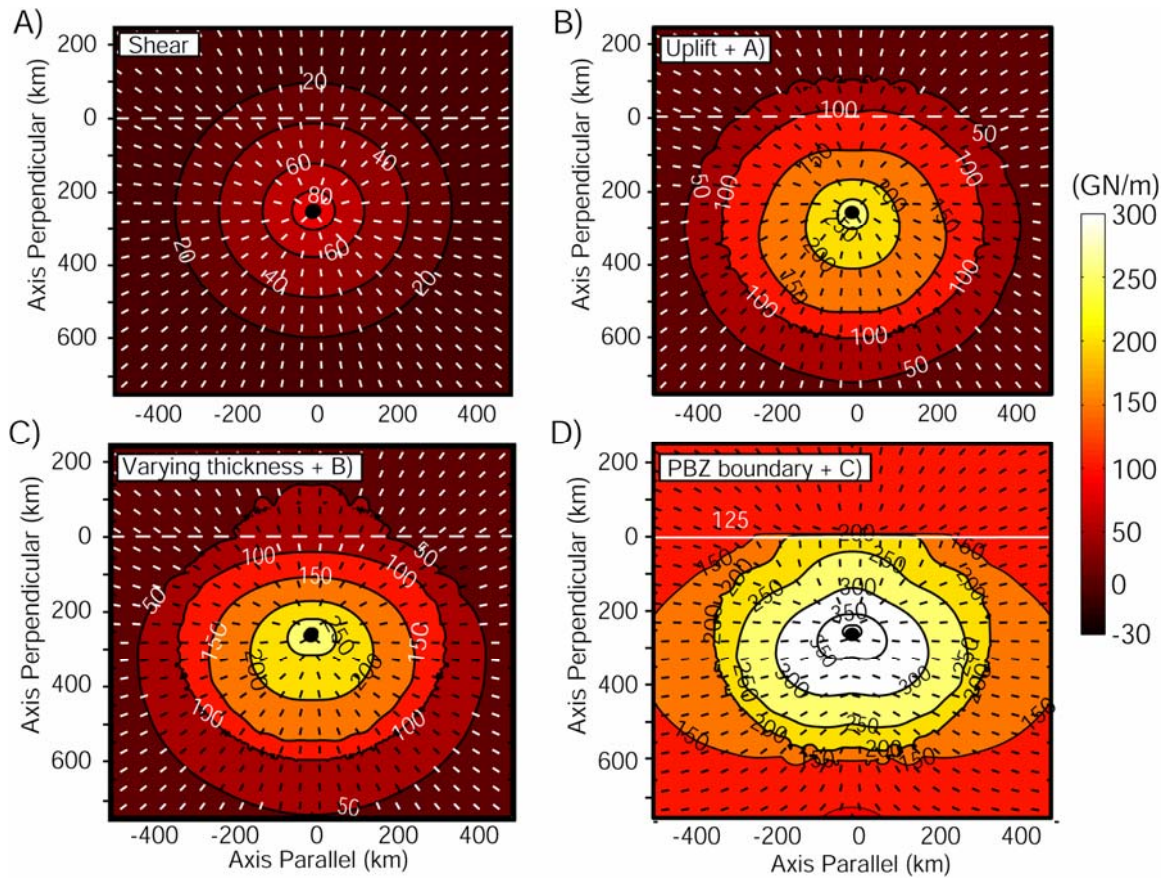


**Figure 5.** Calculated solutions of the most tensile stress resultant magnitude for different components of plume-ridge interaction. Contours are most tensile stress resultant (GN/m) and ticks are stress trajectories of the least tensile stress resultant. The plume center is denoted by a black dot. Dotted white lines denote the future location of the ridge while the solid white line in (D) denotes the implemented ridge boundary and boundary condition (white number). (A) The axisymmetric shear due to plume flow ( $q_s$ ), (B) plus the gravitational body forces due to dynamic topography ( $q_g$ ), (C) plus the effects of varying plate thickness (see equation 2.2.9), (D) plus the ridge boundary condition.

Adding the effects of variations in plate thickness causes the orientations of least tensile stress resultants to rotate toward the gradient in plate thickness (i.e. toward a ridge axis, *Fig. 5c*) and increases the magnitude of the most tensile stress by  $\sim 10\%$ . Finally, introduction of isotropic far field tension and a ridge boundary condition, equal to the far field condition, increases tension uniformly throughout the plate. The zero shear stress (resultant) condition on the ridge tends to orient least tensile trajectories perpendicular to the ridge closest to the hotspot. In the area between the plume and the ridge, the stress resultant trajectories form a fan shape with a center slightly ridgeward of the plume and curve to meet the ridge at nearly right angles (Figure 5d).

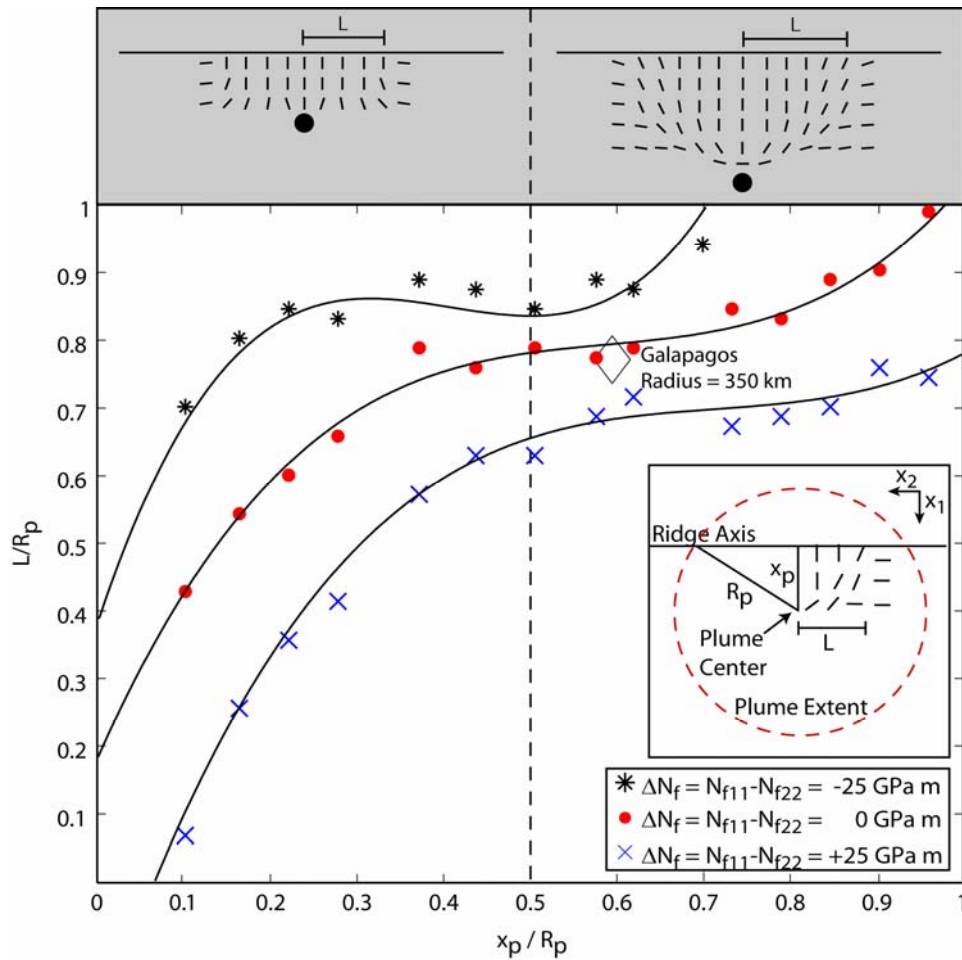


**Figure 6.** Model predictions of normalized lineament half-width,  $L/R_p$ , increase with normalized plume ridge separation,  $x_p/R_p$ , and differential far field stress resultant ( $\Delta N_f = N_{f11} - N_{f22}$ ). The predicted pattern of least tensile stress trajectories forms a fan shaped pattern for  $x_p/R_p$  greater than 0.5. For smaller plume-ridge separations, the trajectories maintain ridge perpendicular orientations between the ridge and plume center. Solid curves are best fit cubic functions which are shown to emphasize the general trends of the model predictions.

Ultimately, the trajectory pattern is produced by the combination of the above forces. When the differential stresses caused by the far field and ridge conditions are small, the trajectory pattern is dominated by the axisymmetric plume forces and displays a fan shape. Such conditions are maintained while the differential far field stress is small or zero, the plume-ridge separation  $x_p$  is relatively large ( $x_p/R_p > 0.5$ ), and when the normal stress on the ridge equals to the far field stress normal to the ridge (Figure 6). A uniform change in the isotropic far field stress with a matching uniform change in the normal traction on the ridge does not change the pattern of stress trajectories, but simply changes the stress resultant magnitude uniformly.

Variations in the pattern of least tensile stress trajectories with  $x_p$  and with the imposed differential far field stress resultants ( $\Delta N_f = N_{f11} - N_{f22}$ , see Figure 6) can be characterized by predictions of  $L$ , the half-width along the ridge axis that lineaments will intersect the ridge axis at an angle greater than  $45^\circ$  (Figure 6, inset). Values of  $L$  normalized by  $R_p$  increase with normalized separation ( $x_p/R_p$ ). At small separations ( $x_p/R_p < \sim 0.4$ ) the increase in width is rapid, at intermediate separations ( $\sim 0.4 < x_p/R_p < \sim 0.6$ ) the increase is more gradual, and for larger separations ( $x_p/R_p > \sim 0.6$ ) width increases again rapidly with separation. Increasing the relative far field tension perpendicular to the ridge ( $\Delta N_f$ ) roughly preserves the dependence on normalized

separation, but shifts the curve to smaller normalized widths (crosses, *Figure 6*). Decreasing  $\Delta N_f$  to negative values increases the normalized widths (asterisks, *Figure 6*).

The dependence of normalized width on the differential far-field stress resultant is better illustrated in *Figure 7*. Here I show  $L/R_p$  at  $x_p/R_p = 0.72$  and vary  $\Delta N_f$  normalized by the differential stress resultants due to plume induced forces in the absence of the ridge and far field conditions (taken 30 km south of the ridge axis),  $\Delta N_p$ . For increasing values of  $\Delta N_f/|\Delta N_p|$ ,  $L/R_p$  decreases until all least tensile trajectories are ridge parallel at  $\Delta N_f/|\Delta N_p| = 1.1$ . This decrease in  $L/R_p$  with differential far field stress is well modeled by a quadratic relationship over the majority of far field conditions. With negative values of  $\Delta N_f/|\Delta N_p|$ , all trajectories eventually become axis-perpendicular causing  $L$  to increase rapidly with decreasing  $\Delta N_f/|\Delta N_p|$  and deviate from the quadratic best-fit line (*Figure 7*, left most points).

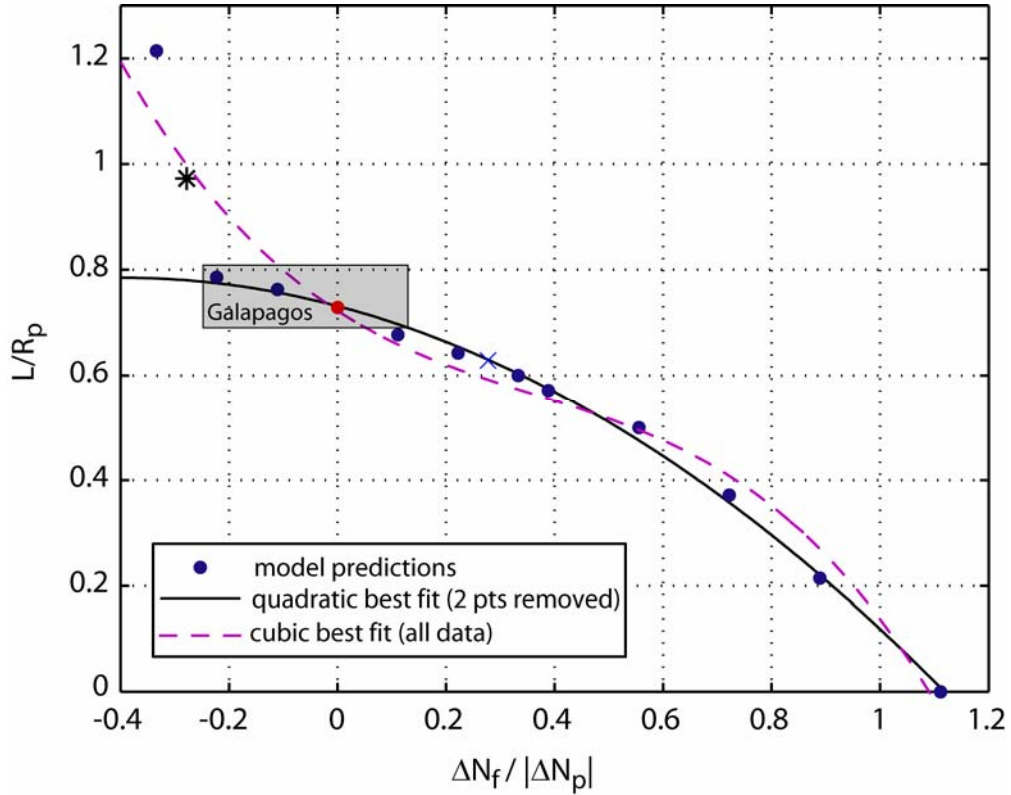


**Figure 7.** Model predictions of lineament half width (see Figure 6),  $L$ , versus the ratio of the differential remote stress resultant ( $\Delta N_f = N_{f11} - N_{f22}$ ) and the magnitude of the differential plume stress resultant,  $\Delta N_p$ , 30 km south of the ridge axis between the plume center and ridge in a calculation with  $N_{f11} = N_{f22} = 0$ . The width of the fan-shaped region diminishes as  $\Delta N_f / |\Delta N_p|$  increases. For a plume ridge separation distance,  $x_p / R_p$ , of 0.7 most of the model predictions are well approximated by a quadratic fit, but a cubic fit is necessary to fit the total range of predictions. Using measurements of the Galapagos lineaments, the stress regime near the GSC falls within the gray box (see text for details). The black star, red dot, and blue cross correspond to symbols in figure 6.

### 3.2 Segmented Ridge

Finally, I test the importance of a transform fault. Transform faults have significant effects upon the near-ridge lithospheric stress field [Pollard and Aydin, 1984; Behn et al., 2002] and the 91°W transform fault along the GSC is an example of large scale segmentation that may affect the lineament pattern. I model a transform fault 125 km in length located north of the plume center. The lengths of the two ridge segments are limited to ~400 km which is the approximate distance of the next set of

transform faults of the GSC to the east and west. Lithospheric thickness is discontinuous across the transform fault throughout the model domain (i.e. I assume the fracture zone extends across the whole model).

First I look at the solutions for a ridge with normal tension equal to the isotropic far field stress. Stress resultants due solely to the far field and ridge boundary conditions are isotropic without the plume forces (Figure 8a). With forces due to a plume of viscosity  $10^{18}$  Pa s, a focus zone of least tensile stress trajectories is seen south of the lower transform corner and rideward of the plume center, but is poorly defined (Figure 8c). Trajectory orientations deviate from the general fan-shaped pattern in the inside corner of the transform. With the larger plume viscosity of  $10^{19}$  Pa s, a focus is apparent near the plume center, while the inside corner region again displays trajectories that deviate from the fan-shaped pattern (Figure 8d).

Next I examine solutions where the normal tension along the ridge is greater than the far field stress. As in the previous case, I first examine the effect of the far field and ridge conditions alone. Trajectories radiate from a distinct focus zone just south of the lower ridge-transform intersection and curve back toward the ridge axis. Near the left (west) side of the transform, the strike of the stress resultant trajectories is nearly parallel to the transform fault and rotates clockwise with distance from the transform (Figure 8b). Stress resultant magnitudes are highly tensile close to the transform, but become compressive south of the transform tip. Inclusion of a plume produces stress resultant magnitudes that are more tensile throughout the plate, reduces the compressive stress south of the transform tip, and produces a general fan-shaped pattern of least tensile stress trajectories (Figure 8d,f). With a plume viscosity of  $10^{18}$

Pa s, the apparent trajectory focus zone remains identical to that without plume forces, but the stress trajectories to the left of the transform rotate counter-clockwise with increasing distance from the transform; in the opposite sense of the trajectories without the plume forces (Figure 8d). With a larger plume viscosity of  $10^{19}$  Pa s, the apparent focus shifts to a location close to the plume center with subtle changes in trajectory orientation near the transform (Figure 8f). Overall, the inclusion of the ridge offset maintains the general fan-shaped pattern of least tensile stress trajectories, but deviates from the solution due to a straight ridge near the transform fault where a focus zone is observed.

To assess where volcanic lineaments are most likely to form I divide the predicted stress resultants by the lithospheric yield strength. For both cases with and without a transform, the fraction of the lithospheric yield strength is largest between the model plume center and the ridge axis, where the plate is youngest. To the south of the model plume center the fraction is relatively low (Figure 9b,c). Model results therefore show that lineament formation is most likely to occur between the plume and ridge axis in a fan-shaped pattern.

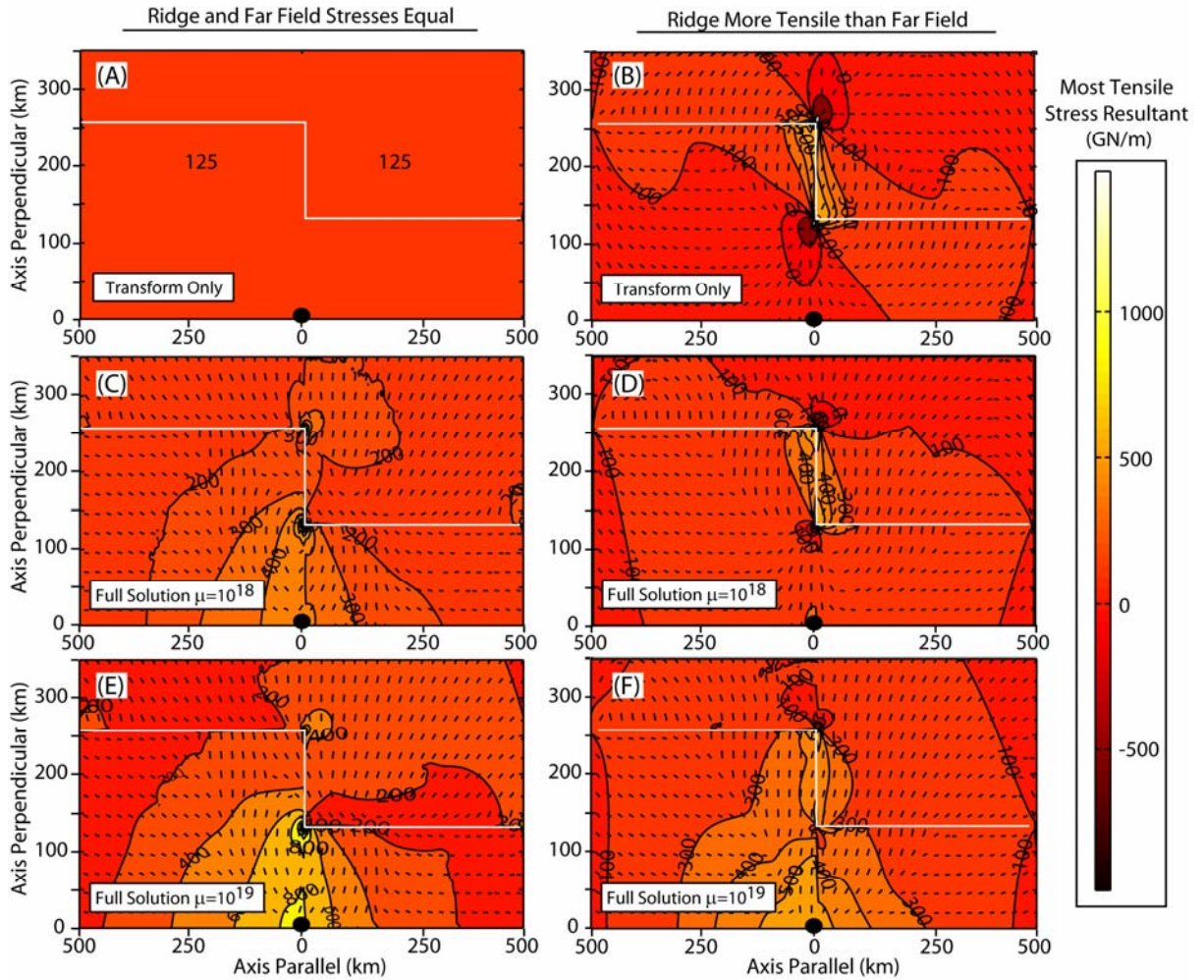


**Figure 8.** (A) Ridge-transform boundary stresses equal to the isotropic far field stresses produce an isotropic stress field. (B) Least tensile stress resultant trajectories and magnitudes of most tensile stress resultant due to a segmented ridge show many of the characteristics of the Galapagos lineaments when the ridge is more tensile by 100 GPa m than the far field, but do not explain the orientation of the Wolf-Darwin lineament. (C and D) Added effects of a plume with a viscosity of  $10^{18}$  show features consistent with the Galapagos lineaments when the ridge is more tensile than the far-field, but deviate near the inside transform corner when the ridge and far-field stresses are equal. (E and F) A plume with a viscosity of  $10^{19}$  is more consistent with other hot spots, such as Kerguelen. White lines denote the location of the ridge axis and black dots at the origin denote the model plume center.

## 4. Discussion

### 4.1 The Galapagos Lineament Pattern

It is well known that dikes and fractures tend to propagate along trajectories of least tensile stress [Ode, 1957; Muller and Pollard, 1977; Pollard and Aydin, 1988; Ernst and Buchan, 1997; Muller et al., 2001a; Glen and Ponce, 2002]. Islands along the lineaments to the west of the southward projection of the 91°W transform fault, display north-northwest trending fractures, whereas east-west trending fractures are found to the east [Geist et al., 1986; Cullen and McBirney, 1987; Harpp and Geist, 2002; Harpp et al., 2003]. Thus, the fractures roughly parallel the lineaments, consistent with the notion that volcanic lineaments will tend to form along trajectories of least principle tension in the whole lithosphere.

The ridge-transform-ridge configuration of the model shown in figure 8d and 9b is successful in reproducing the gross pattern of lineaments in the Galapagos region. This model successfully predicts lineaments to focus south of the southern transform-ridge intersection. Because predicted magnitudes of integrated stresses are appreciable fractions of the integrated lithospheric strength only on the youngest lithosphere, models also predict formation of lineaments between the presumed plume center (Fenandina Island) and the GSC. While both the straight and segmented ridge models produce the above general characteristics, the segmented ridge does slightly better because the transform fault causes the apparent focus zone to be north of the plume center more consistent with observations (Figure 8, 9b,c). Without the transform, or for large plume viscosities, the focus center is nearly at the plume center, similar to models that only include plume shear and uplift (Figure 5a,b). Models including the transform

offset thus provide a solution to the paradox of the lineament focus being offset from the presumed plume center.

The transform fault at 91°W was previously suggested to be the primary control on lineament patterns at the Galapagos [Harpp and Geist, 2002; Harpp et al., 2003]. These models support a significant contribution from the transform, but models also indicate that the plume effects are important. For example, the model with only the ridge-transform effects predicts least tensile stress trajectories that are nearly perpendicular to the Wolf-Darwin lineament and other lineaments far from the transform fault (Figure 8b). In addition, the transform effects cause relatively compressive deviatoric stress resultants south of the lower transform corner which should inhibit lineament formation. The added plume effects produce trajectories consistent with the Wolf-Darwin lineament and tensile stress resultant magnitudes near the southern transform tip. Overall, the lineament pattern is better modeled by the case of a ridge that is more tensile than the far field stress. The focus of trajectories is better delineated and trajectories close to the transform roughly resemble the lineament orientations. I conclude that the plume effects are critical to the fan-like pattern of Galapagos lineaments far from the transform, while the transform fault effects are important to lineament orientations close to the transform and to locating the focus of the fan ridgeward of the plume center.

Based upon gravity modeling, Feighner and Richards [1994] predict a discontinuity in the effective elastic thickness of the Nazca plate near the Galapagos archipelago, with lithosphere to the west and south of the Wolf-Darwin lineament more rigid than the lithosphere to the north and east. Lithospheric strength in these models

varies both north-south due to plate-cooling and east-west across the age discontinuity due to the transform fault. This closely approximates the proposed strength variations of *Feighner and Richards* [1994], only significantly differing between the transform and the WDL. Tests on the importance of this east-west discontinuity to the overall pattern of stress resultants in these models indicate little change in trajectory orientations or stress resultant magnitudes and suggest that inclusion of the more complex strength variations of *Feighner and Richards* [1994] will not significantly alter the solutions.

This said, it is important to note that where the stress resultant magnitudes are equal to or exceed the integrated lithospheric yield strength, the lithosphere will deform anelastically and its behavior is not represented by the elastic rheology. This applies especially to the inside corner regions of the transform fault model where stress concentrations due to the crack tips may exceed the yield strength of young lithosphere (Figure 9b). I therefore consider these purely elastic models as representing the minimal level of sophistication needed to address the posed problem.

Regarding the source of magma feeding the lineaments, geochemical analysis of lavas from the Wolf-Darwin lineament shows increasing plume chemical influence toward the ridge (e.g.  $^{87}\text{Sr}/^{86}\text{Sr}$  from 0.7026 – 0.7034) [*Harpp and Geist*, 2002]. These chemical variations could be caused by changes in melt composition along an asthenospheric plume channel oriented along the pseudofault near Wolf Island or by tapping of plume-contaminated mantle dispersed throughout the region and already processed by melting beneath the GSC [*Harpp and Geist*, 2002]. The models discussed here require a melt source beneath the lineaments and suggest that the lithospheric

stress field controls where and how this melt erupts, but do not require asthenospheric channels to form the lineaments.

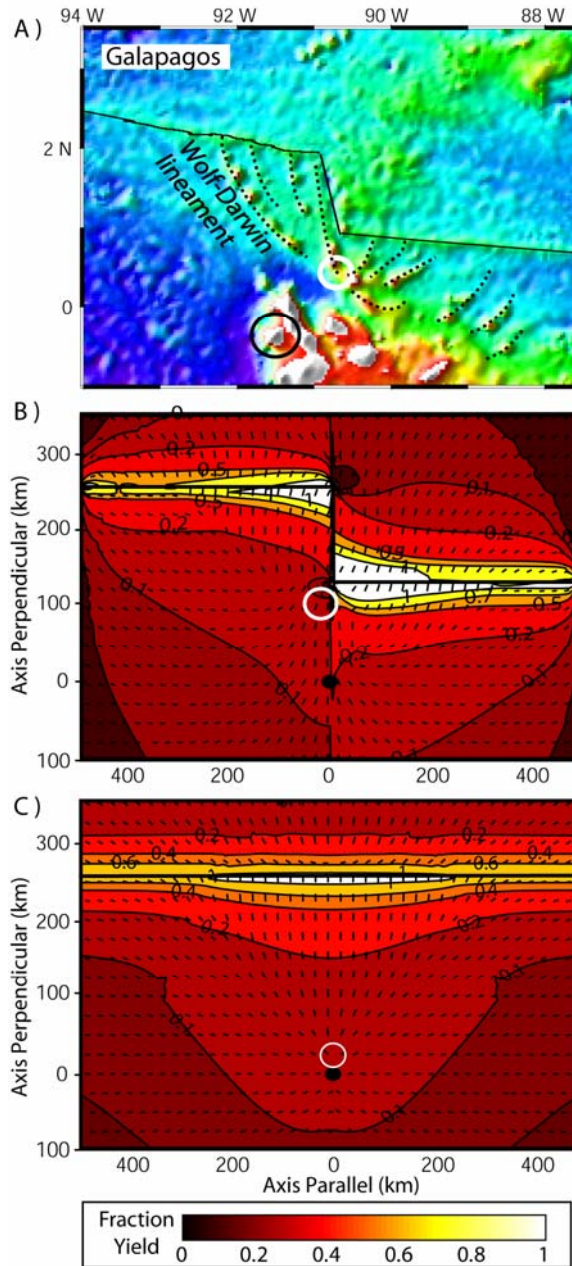


**Figure 9.** (A) Map of the Galapagos Spreading Center (denoted by sub-horizontal black lines), the Galapagos archipelago (black circle enclosing Fernandina Is., location of most recent volcanism), and the volcanic lineaments (black dashed lines) which appear to fan out from a focus at the white circle. Contours of fraction of lithospheric yield strength (most tensile stress resultant divided by yield strength) for (B) a model with two ridge segments separated by a transform fault and (C) a model with a single, straight ridge axis. Ridges are more tensile than the imposed isotropic far field stress by 100 GPa m. Ticks mark trajectories of least tension. Magma penetration via dikes will tend to align with these trajectories. Models predict trajectories to fan northward away from an apparent center within the white circles. Black dots show the center of the model mantle plume.

I propose a model where the lineaments form in regions of high integrated tension that will promote magma to crack its way through the lithosphere and erupt to initiate a volcanic lineament. The process of diking and volcano loading decreases the integrated tension in the underlying lithosphere and leads to tensile stress concentrations near the ends of the lineament. This will promote new volcanism and lengthening of the lineament in a manner much like a giant crack in the lithosphere. Volcanism initiates where magma supply is high and tension is a large fraction of the lithospheric yield strength near the ridge axis. Volcanism subsequently propagates away from the ridge axis roughly according to the pre-existing lithospheric stress field. Indeed, along Wolf-Darwin, ages are seen to decrease away from the ridge [Sinton *et al.*, 1996] suggesting that volcanism initiated near the ridge axis and propagated southeast. Volcanic initiation near the ridge axis supports the assertion that regions of high lithospheric yield fraction will be most penetrable by magma. Age dating of the other Galapagos lineaments will provide a further test of this hypothesis.

#### *4.2 Islands of the Galapagos Archipelago*

Islands of the Galapagos Archipelago also show aligned fractures [Darwin, 1860] and the volcanoes themselves are aligned along rectilinear “Darwinian trends” most readily exhibited by the “J” shaped Isabela island [McBirney and Williams, 1969]. The stresses I have modeled could have influenced the formation of these islands. A similar pattern is displayed by least tensile stress trajectories near the plume center in the straight ridge models and slightly rideward of the plume center in models of a segmented ridge with a large viscosity plume (Figure 8e,f, 9c). However, the main

islands are larger than the volcanic lineaments and will introduce much larger bending stresses which may have been more important in controlling where adjacent volcanoes form [tenBrink, 1991; Hieronymus and Bercovici, 2001]. Future studies that incorporate bending into models of plume-lithosphere interaction are needed to better explore the formation of the main Galapagos islands.

#### 4.3 Constraints on the Tectonic Stress Field

The differential stress ( $\Delta N = N_{11} - N_{22}$ ) induced by the combination of plume forces, and the far field and ridge boundary conditions controls the orientations of the least-tensile stress trajectories and thus the width of the observed fan-shape pattern. One quantity that characterizes the shape of the fanning lineaments is the half-width,  $L$ , along the ridge axis. These models show that plume-ridge separation,  $x_p$  and the differential stress in the far field strongly influence the value of  $L$  and may indicate one reason why patterns of lineaments differ between hot spot localities such as Kerguelen, Tristan de Cuhna and the Galapagos.

With knowledge of  $L$ ,  $R_p$ , and  $x_p$  from the Galapagos I can use the predictions of figure 7 to place first-order constraints upon the far field stress field in the near-GSC lithosphere. Taking measured values for  $x_p = 260$  km [Ribe, 1996],  $L = 255$  km, and a  $R_p = 350$  km based upon the location of a distinct decrease in chemical plume influence, crustal thickness and plume-driven melt supply seen at approximately  $93^\circ\text{W}$  [Detrick et al., 2002; Cushman et al., 2004], I predict the ratio of differential far field stress to differential plume stress ( $\Delta N_f / |\Delta N_p|$ ) to fall between -0.2 and 0.1 (Figure 7, gray box). These models predict a nearly isotropic far field stress in the near-GSC lithosphere.

This estimate provides an independent prediction of the stress field around the Galapagos and provides an additional constraint on lithospheric stress field models.

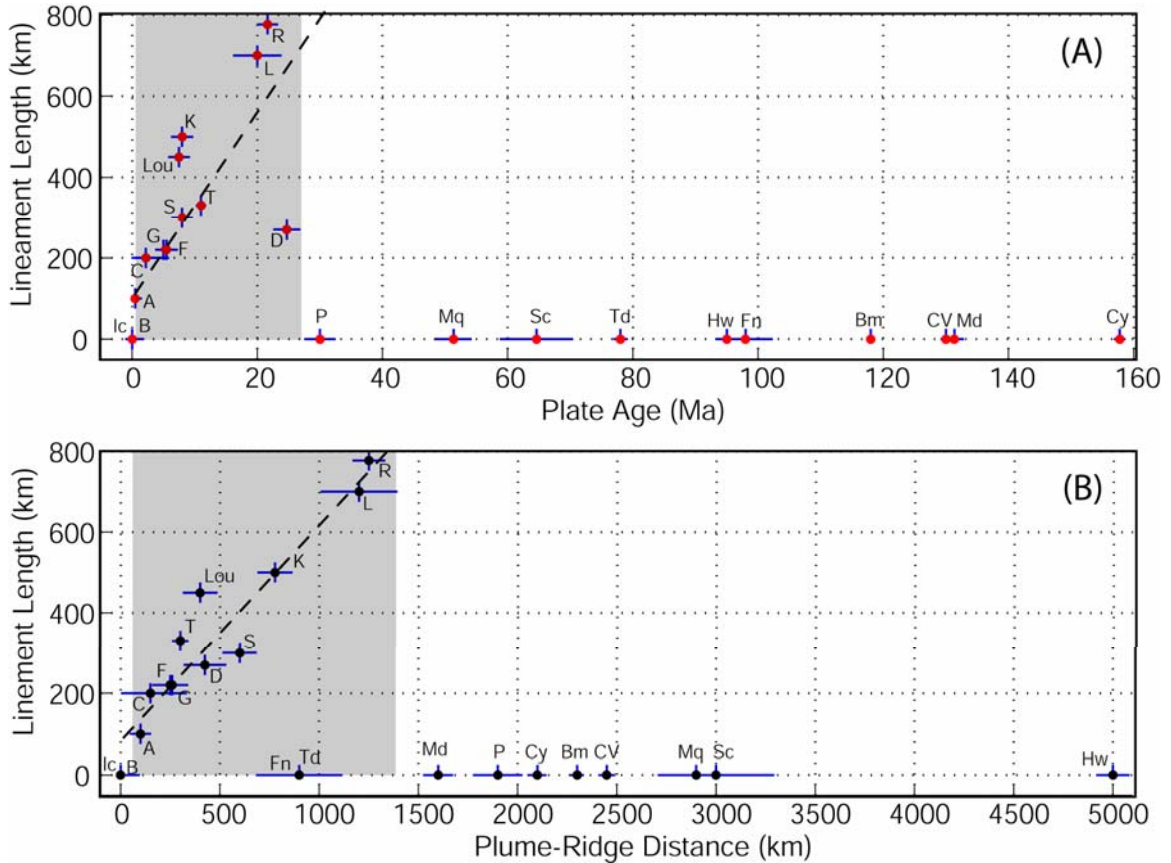


**Figure 10.** Observations of 23 oceanic hotspots show distinct patterns in lineament formation. (A) This plot of plate age at the time of lineament emplacement versus lineament length demonstrates a region of lineament formation between plate ages of 0.2 to 25Ma (hot spots without lineaments are associated with a lineament length of zero). (B) Comparison of plume-ridge separation and lineament length also shows a restricted region of formation between 100 and 1250 km. Both trends show an approximately linear (black dotted best fit line) increase in lineament length in the region of formation (gray boxes). Plate ages and errors in plate age from [Muller *et al.*, 1997]. Where error bars are not visible, the symbol is larger than the error. Hot spots are labeled as; A, Amsterdam; B, Bowie; Bm, Bermuda; C, Cobb; CV, Cape Verde; Cy, Canary; D, Discovery; F, Foundation; Fn, Fernando; G, Galapagos; Hw, Hawaii, I, Iceland; K, Kerguelen; L, Line Islands; Lou, Louisville; Md, Madeira; Mq, Marquesas; P, Pitcairn; R, Reunion; S, Sala y Gomez; Sc, Society; T, Tristan; Td, Trinidade. Lineament ages and hot spot tracks are compiled from the literature [Duncan, 1984; Bonneville *et al.*, 1988; Desonie and Duncan, 1990; O'Connor and Duncan, 1990; Sonne, 1990; O'Connor and Roex, 1992; O'Connor *et al.*, 1995; Small, 1995; Geli *et al.*,

1998; *Vlastelic et al.*, 1998; *Douglass et al.*, 1999; *Hekinian et al.*, 1999; *Geldmacher and Hoernle*, 2000; *Davis et al.*, 2002; *Weis et al.*, 2002]

#### *4.4 Global Lineament Formation*

Although the majority of this study focuses on the Galapagos lineaments, volcanic lineaments appear to be common manifestations of hot spot-ridge interaction. I have identified at least 12 separate hot spots currently or previously located near to mid-ocean ridges, showing volcanic lineaments similar to those at the Galapagos. They include Azores, Cobb, Discovery, Foundation, Kerguelen, Line Islands, Louisville, Musicians, Reunion, Sala y Gomez, St. Paul (Amsterdam), and Tristan de Cuhna hot spots. All of the above hot spot-ridge systems share the common characteristic of having a ridge axis near the inferred location of the hot spot based on available dates of volcanism and seafloor magnetic lineations.

This model predicts plumes to introduce integrated lithospheric stresses of appreciable fractions of lithospheric yield strength only in young lithosphere. To evaluate the off-axis extent of lineament formation I estimate the age of the plate on which the lineaments were emplaced, lineament lengths, and the relative location of the hot spot at the time of lineament emplacement. Ages of volcanism along the hot spot track and lineaments are compiled from the literature (see Figure 10 for references) and crustal ages are determined from seafloor isochrons [*Muller et al.*, 1997]. I measure the maximum length of lineaments at each hot spot by creating regional bathymetry maps and digitally measuring the distance along each lineament.

Figure 10 shows the relationships between maximum lineament length, plate age and plume-ridge separation for 23 oceanic hot spots with error bars in plume-ridge separation and plate age from the error contours of *Muller et al.* [1997] and errors in lineament length measurements estimated at  $\pm 20$  km. Hot spots that do not show evidence for lineaments are given a lineament length of zero. Lineaments, on average, reach lengths of about 75% of the plume-ridge separation distance at the time of emplacement. Approximately linear relationships between lineament length and plate age, and lineament length and plume-ridge separation are seen until a critical distance or seafloor age is reached (Figure 10). Lineaments are not seen beyond 1250 km or in lithosphere older than  $\sim 25$  Ma. This cutoff is likely due to the presence of thick, strong lithosphere resisting plume stresses, the lack of interaction between the ridge and plume at separation  $> 1250$  km, or both. *Schilling* [1991] notes a cutoff in geochemical tracers and bathymetric highs with plume-ridge separations of  $\sim 1600$  km, slightly greater than the maximum distance found in this collection of hot spots with lineaments. In addition, lineaments do not appear to form near ridge-centered plumes. For example, at Iceland volcanic lineaments are primarily focused along 3 major rift axes, but are not present off-axis. This localization of volcanism may be a consequence of efficient suction of magma to these rift zones, or, alternatively, the rift zones themselves may be an expression of a plume-induced stress field similar to that which causes off-axis lineament formation. Not only does *Fig. 10* demonstrate that lineaments form preferentially within certain plate ages and separation distances, it demonstrates the commonality of lineament formation at near ridge hot spots.

## 5. Conclusions

In this study I use a 2-D model of plume-ridge interaction to examine factors contributing to the formation of lineaments seen at the Galapagos and other oceanic hot spots. I present a new method of simulating patterns of stress caused by the local factors of plume shear, gravitational body forces due to uplifted topography, ridge boundary conditions, and variations in plate thickness.

Least tensile stress resultant trajectories due to a plume interacting with a linear ridge axis form a fan-like pattern between the plume and ridge. The trajectories tend to curve to meet the ridge axis at approximately right angles if the shear stress on the ridge is zero. While the general fan-shaped pattern is preserved beyond plume-ridge separations over  $\sim 0.5$  times the radius of the dominantly axisymmetric plume flow (Figure 6, where  $x_p > L$ ), the pattern deviates to the east and west for smaller plume-ridge separations, but maintains a ridge-perpendicular orientation between the ridge and plume center. The addition of a transform fault creates a more complex pattern with least tensile stress trajectories again curving to meet the ridge at right angles, but with the focal point of the fan pattern further ridge-ward than the corresponding linear ridge model (Figure 9).

Increasing the far field tension perpendicular to the ridge relative to that parallel to the ridge causes the width of the fan at the ridge axis to decrease in an approximately quadratic function of  $\Delta N_f$ . Examination of this relationship in context of Galapagos lineaments suggests that the differential far field stress is nearly isotropic in the region of the GSC.

The model stress resultant trajectories closely resemble the pattern of lineaments seen near the Galapagos when the ridge is segmented and more tensile than the far field stress. Results reconcile the difference in plume center location from that of lineament focus and explain the decreasing trend and curvature of lineaments as the transform is approached. I propose that the Galapagos lineaments form near the ridge axis where tension is a large fraction of the lithospheric strength and then propagate southward roughly following the predicted stress trajectories. Volcanism is probably fed by a widespread melt supply from the underlying asthenosphere.

Measurements of 23 separate oceanic hotspots show a nearly linear increase in volcanic lineament length with increasing age of the plate at the hot spot and increasing plume-ridge separation distance. This linear relationship holds until plate ages of ~25Ma and plume-ridge separation distances in excess of ~1250 km where lineament formation is no longer observed. I conclude that beyond 25 Ma, plate thicknesses are too large for plume stresses to enhance the ability of magma to penetrate the plate. Also, plume-ridge distances greater than 1250 km probably prevent significant asthenospheric interaction of the plume and ridge.

## Chapter 3:

### **Mid-ocean ridge jumps associated with hotspot magmatism**

#### **1. Introduction**

The evolution and geometry of mid-ocean ridges influences the thickness [Parsons and Sclater, 1977], shape and movement [Nicholson *et al.*, 1994; Bohannon and Parsons, 1995; Hey, 1998] of the tectonic plates. Repeated changes in the location of ridge axes, such as those caused by hotspot influenced asymmetric spreading [Muller *et al.*, 1998], ridge segment propagations [Sempéré *et al.*, 1995] or discrete ridge jumps, can significantly alter the global pattern of plate tectonics through time.

Many places along the mid-ocean ridge network have experienced ridge jump behavior including localities near Ascension, Conrad Rise, Discovery, Galápagos, Iceland, Ninety-East Ridge, Louisville, Shatsky Rise, Shona and Tristan de Cunha [Hey, 1977; Mammerickx and Sandwell, 1986; Brozena and White, 1990; Muller *et al.*, 1993; Krishna *et al.*, 1995; Small, 1995; Hardarson *et al.*, 1997; Nakanishi *et al.*, 1999; Krishna and Rao, 2000; Briaies and Rabinowicz, 2002]. Although the above jumps all cause a discrete change in the location of the ridge, the distance over which a jump occurs and the type of ridge boundary varies. Shatsky Rise, which is associated with large outputs of magma, is the location of a series of triple junction jumps that repeatedly displaced the triple junction by up to 800 km [Nakanishi *et al.*, 1999]. In contrast, relocations of ridge axes over much smaller distances (10-100km) occurred near Ascension, Galápagos and Iceland (Figure 1). Intermediate between the very large jumps at Shatsky Rise and the smaller jumps at Ascension, Galápagos and Iceland, were

a series of at least 4 ridge jumps near the Ninety-East Ridge, transferring portions of the Antarctic plate to the Indian plate. At each of the above locations, hotspot-ridge interaction is likely to be the dominant cause of ridge jump initiation.

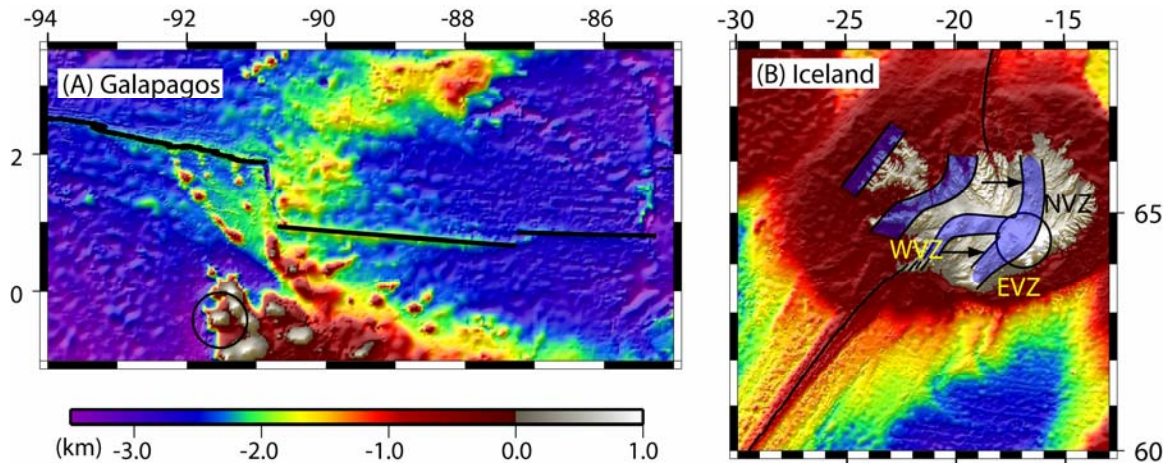


**Figure 1.** Satellite derived bathymetry [Smith and Sandwell, 1994] and digital elevation of the (A) Galápagos and (B) Iceland hotspots and the nearby ridges (black lines). Former ridge jumps kept the axis of the Galápagos Spreading Center close to the hotspot, but ridge jumps ceased approximately 5 Ma. At Iceland the Northern Volcanic Zone (NVZ) formed after completion of a ridge jump at  $\sim 3$  Ma [Hardarson *et al.*, 1997] and the Eastern Volcanic Zone (EVZ) has since propagated to the southwest. The Western Volcanic Zone (WVZ) appears to be dying due to the propagation of the EVZ [LaFemina *et al.*, 2005]. The arrows indicate the direction of the most recent ridge jump towards the current location of the hotspot (black circle). The bands marking the previous ridge axes locations encompass previous estimates [Hardarson *et al.*, 1997; Garcia *et al.*, 2003].

Assuming hotspots overlie sources of anomalously hot asthenosphere, there are several mechanisms that can promote ridge jumps including lithospheric tension induced by buoyant and convecting asthenosphere [Mittelstaedt and Ito, 2005], mechanical and thermal thinning of the lithosphere due to hot flowing asthenosphere [Jurine *et al.*, 2005], and penetration of magma through the plate [Kendall *et al.*, 2005]. This study focuses on the last process by quantifying the effects of lithospheric heating caused by hotspot magmatism. I examine how seafloor age at the hotspot, spreading

rate, magmatic heating rate (magma flux) and ridge migration influence the timescale and viability of ridge-jumps. Results indicate that magmatic heating, alone, can cause ridge jumps for geologically reasonable magma fluxes only in young, slow-moving lithosphere. Further, I show that magmatic heating can also promote jumps in back-arc spreading systems such as the Marianas as well as propagation of ridge segments at slow-spreading ridges such as the Mid-Atlantic Ridge.

## **2. Conceptual and Mathematical Model**

### *2.1 Conceptual Model*

Figure 2 illustrates a conceptual model for a ridge jump induced by magmatic heating from an off-axis hotspot. Magma is produced by the hotspot beneath the plate and then penetrates the lithospheric thermal boundary layer to create hotspot volcanoes. During volcanism, some of the heat carried by the magma is transferred to the lithosphere, weakening it over time. Heating of the lithosphere is controlled by the balance between the heat flux from the magma, advection due to plate spreading and surface heat flow. If the magmatic heating rate is sufficient, the lithosphere will thin until new rifting begins over the hotspot. The weaker, new rift then becomes an established ridge axis and spreading at the former axis ceases.

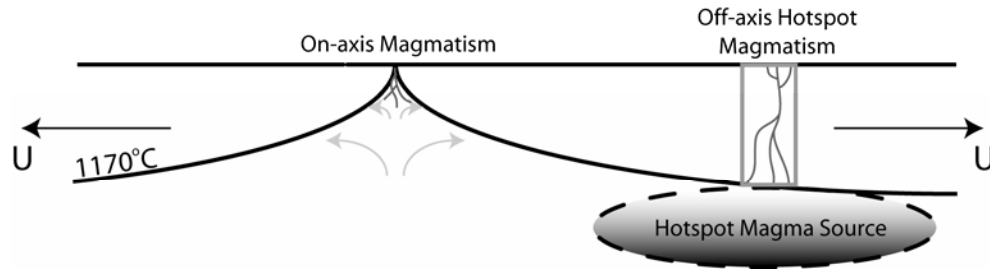


**Figure 2.** Conceptual model of magmatic heating of the lithosphere. A source of melt beneath the hotspot (dashed circle) provides magma which passes through the lithosphere in a magma transport zone (grey box) and proceeds to thermally weaken the lithosphere. The rate of heating is influenced by magma flux, spreading rate ( $U$ , black arrows) and surface heat flow. Magmatism also heats and thermally weakens the ridge axis.

## 2.2 Mathematical and Numerical Model

Using the FLAC (Fast Lagrangian Analysis of Continua) method [Cundall, 1982; Poliakov *et al.*, 1993], I solve the equations describing conservation of mass and momentum for a visco-elastic-plastic continuum in 2-D Cartesian geometry [Lavier and Buck, 2002]. The model domain is 150 km laterally by 50 km vertically and is made up of a grid of 300 by 100 Lagrangian (i.e. the grid deforms with the model) quadrilaterals each composed of two pairs of triangular elements. Since deformation of the grid degrades numerical accuracy, model quantities are linearly interpolated to a new grid when the minimum angle of any triangle is less than a given value ( $10^\circ$ ). The ductile asthenosphere is approximated as a visco-elastic material with a non-Newtonian, temperature-dependent viscosity, and the strong, brittle portion of the lithosphere is treated as an elastic-perfectly-plastic material subject to a Mohr-Coulomb failure criteria. Faulting in the model develops through localization of strain by a reduction in cohesion from 44 MPa to 4 MPa over a plastic strain of 0.25 (i.e. over  $\sim 500$ m of fault offset). Rheologically, the model consists of a 6-km-thick crust of dry diabase

[Mackwell *et al.*, 1998] and a dunite mantle [Goetze and Evans, 1979]. The mechanical boundary conditions include a horizontal, uniform velocity equal to the half spreading rate,  $U$ , on the two vertical sides of the box, a stress free top surface, and zero shear and hydrostatic pressure on the base.

Temperature,  $T$ , is calculated using the following advection-diffusion equation,

$$\frac{\partial T}{\partial t} = \kappa \nabla^2 T - \bar{\mathbf{u}} \cdot \nabla T + \frac{(source)}{\rho c_p}, \quad (1)$$

where  $\kappa$  is the thermal diffusivity ( $3 \times 10^{-6} \text{ m}^2 \text{ s}^{-1}$ ),  $t$  is time,  $\bar{\mathbf{u}}$  is the velocity vector,  $\rho$  is the density ( $2900 \text{ kg m}^{-3}$  for the crust and  $3300 \text{ kg m}^{-3}$  for the mantle) and  $c_p$  is the specific heat ( $1000 \text{ J C}^{-1} \text{ kg}^{-1}$ ) [Turcotte and Schubert, 2002]. See Table 1 for definitions of all variables. The thermal boundary conditions consist of an isothermal top, set to  $0^\circ\text{C}$ , and a bottom boundary equal to the temperature of a half-space cooling model at 50 km depth with thermally reflecting side boundaries. The initial temperature field is described by an analytical solution for half-space cooling [e.g. Parsons and Sclater, 1977] with an asthenospheric temperature of  $1300^\circ\text{C}$  (appropriate for shallow upper mantle that has had latent heat of melting removed from it [e.g. Asimow *et al.*, 2004]). Numerically, heat advects with the grid and thermal diffusion is calculated using explicit finite differences.

Magmatic heating is incorporated at the ridge as well as at the off-axis hotspot.

This is done in the “source” term of Eq. (1), which is defined as  $q_{ridge}$  in a specified zone at the ridge axis and  $q_{hotspot}$  within an off-axis hotspot zone, both of fixed width,  $w$ .

Outside of the ridge axis and hotspot zones,  $q_{ridge}$  and  $q_{hotspot}$  are equal to 0. Within the hotspot zone,  $q_{hotspot}$  is defined by,

$$q_{hotspot} = \rho c_p \beta F(x) (T_{asth} - T(x, z, t)), \quad (2)$$

where  $T_{asth}$  is the temperature of both the asthenosphere and the penetrating magma (1300°C),  $\beta$  is the magnitude of the hotspot heating rate and  $x$  and  $z$  are the horizontal and vertical coordinates. The constant,  $\beta$ , controls the magnitude of  $q_{hotspot}$  and is set manually. The function  $F(x)$  is a Gaussian function that describes the dependence of  $q_{hotspot}$  on horizontal position,  $x$ ,

$$F(x) = \exp\left(\frac{-\Delta x^2}{2\sigma^2}\right) \cdot H[w - \Delta x], \quad (3)$$

where  $\sigma$  is the standard deviation of the Gaussian distribution ( $\sigma = w \cdot (2\sqrt{2\ln(2)})^{-1}$ ),  $\Delta x$  is the difference between  $x$  and the center of the hotspot and  $H$  is the Heaviside function which is equal to 0 outside of the hotspot heating zone and 1 within this zone. For most cases, I assume a reference width of the hotspot heating zone of  $w = 2$  km, which is similar to the width of the region of long period earthquakes (often associated with magma movement) between 12-24 km depth beneath Kilauea [Wolfe *et al.*, 2004]. I discuss the effects of varying  $w$  in Section 3.3.

I also consider magmatic heating due to the accretion of magma to form the oceanic crust. The accretion zone,  $w$ , is set to be 2 km wide and 6 km in height with  $q_{ridge}$  defined by,

$$q_{ridge} = \rho c_p \cdot F(x) \frac{(T_{asth} - T(x, z, t)) \cdot R(t)}{w}. \quad (4)$$

where  $R(t)$  is the ridge divergence rate ( $R = 2U$  at  $t = 0$ ) and  $F(x)$  is defined by Equation (3) except that here  $\Delta x$  is the difference between  $x$  and the location of the ridge axis. Below, I examine model solutions both with and without  $q_{ridge}$ .

Because little is known about the mechanisms of magma transport through the lithosphere, the above equations for magmatic heating are designed to be as general as

possible and to not require defining a specific transport mechanism. Eq (2), for example, is the solution for heating of material between two vertical channels of magma of constant temperature. The form of the equation should be reasonable for a wide range of channel geometries and spacing, with the requirement that magma temperature remains close to its starting value ( $T_{asth}$ ), a condition that would hold so long as liquid magma survives to the surface without completely freezing. For reference, the above conditions, as well as the range of heat fluxes simulated by these models, would be met with a scenario involving vertical magma channels having flow rates described by Poiseuille flow, widths starting at 0.2-1.25 m but decreasing due to partial freezing, each lasting for 0.25-1.5 days, and re-forming in the hotspot magma zone every 40-150 years.

The geologic implications for the dependence on the temperature contrast between the magma and host rock are that the majority of heat transfer occurs in the cool thermal boundary layer, regardless of its thickness. At both normal and hotspot affected mid-ocean ridges, most of the magmatic heat transfer occurs near to or within the crust [Kelemen *et al.*, 1997; MacLennan *et al.*, 2001]. Away from the ridge axis, the model predicts a thicker thermal boundary layer and thus a larger depth range of magmatic heating. Currently, the depth range of off-axis crystallization and the related thermal structure are poorly known.

Finally, while hydrothermal circulation is thought to be important at shallow depths [Chen and Morgan, 1990], I do not explicitly include this effect. The scaling laws that I establish (Section 3.3), however, depend on the difference in the integrated heating rates between the off- and on-axis heating zones. Thus the overall results are

robust to the extent that hydrothermal circulation is not extremely different between the ridge and hotspot. If hydrothermal cooling contributes a larger fraction of the heat budget of the thin thermal boundary layer at mid-ocean ridges, the predictions made here will tend to under-estimate the importance of off-axis magmatic heating in promoting ridge jumps.

### 2.3 Geologic parameters

I consider three types of simulations. Type 1 involves magmatic heating at an off-axis hotspot located a fixed distance from the ridge, but does not include ridge-axis heating ( $q_{ridge} = 0$ ). Type 2 includes magmatic heating at a fixed hotspot and at the ridge axis. For Type 1 and 2 cases, the hotspot magma penetration zone is located beneath seafloor of ages 1 or 2 Myr, with half spreading rates of  $U = 10, 20, \text{ or } 30$  km/Myr and a variety of input heating rates,  $q_{hotspot}$  ( $\beta$  ranges between  $8.5 \times 10^{-14} \text{ s}^{-1}$  and  $1.25 \times 10^{-12} \text{ s}^{-1}$ ). This range of parameters is not meant to span the geologic range, but rather to yield an appreciable range of the fundamental parameters that control the system.

Finally Type 3 cases have a hotspot magma zone that migrates relative to the ridge axis (or the ridge migrates relative to a “fixed” hotspot) without ridge axis heating. These cases have a spreading rate of 20 km/Myr with three heating rates ( $\beta = 8.5 \times 10^{-14} \text{ s}^{-1}, 2.1 \times 10^{-13} \text{ s}^{-1}, 4.2 \times 10^{-13} \text{ s}^{-1}$ ) and ridge-hotspot migration rates of  $U_{mig} = 10\text{-}30$  km/Myr.

Models are run until the temperature has reached steady state without a ridge jump (for Types 1, 2), a ridge jump occurs (for Types 1, 2) or the magma penetration

zone migrates across the model domain (for Type 3). Ridge jumps are defined as complete when the divergence rate at the off-axis intrusion zone is equal to 80% of the full spreading rate of the original ridge axis (Figure 3c). In the following section I first quantify the hotspot magmatic heating fluxes needed to generate ridge jumps and then apply the results to hotspot-ridge environments where magma fluxes have been estimated as well as to the Mariana back-arc and non-hotspot influenced areas of the Mid-Atlantic Ridge.

### **3. Results**

#### *3.1 Time Evolution: Fixed Hotspot Magma Penetration Zone (Type 1 and 2)*

For Types 1 and 2, the ridge system is first allowed to equilibrate to steady state without a hotspot ( $q_{hotspot} = 0$ ). Then, at time  $t = 0$  a hotspot is initiated and  $q_{hotspot}$  is imposed as in Eq. 2. Immediately after  $t = 0$ , spreading is fully accommodated at the ridge axis and hotspot magmatism begins to thin and warm the off-axis lithosphere (Figure 3, 4). Continued hotspot heating leads to weakening of the off-axis lithosphere, which initiates rifting and perturbs the mantle flow pattern, such that small amounts of upwelling begin to occur near the hotspot zone. As the off-axis lithosphere continues to weaken, larger divergence rates develop and induce asthenospheric upwelling (Figure 4). In models that generate a ridge jump, after a period of magmatism (0.05–3.0 Myr) a relatively short period (~0.2–0.8 Myr) of coeval rifting occurs during the shift of spreading from the old axis to the new rift. During this period, the divergence rates at the two rifts change rapidly, but the lithosphere between them experiences small lateral velocity gradients, acting as a “microplate”. Throughout this “microplate” stage, the

divergence rate decreases sharply at the original spreading axis. This causes cooling and strengthening of the lithosphere at the original axis and faster spreading at the new rift. Finally, as the divergence at the original ridge axis ceases, the off-axis location establishes stable seafloor spreading.

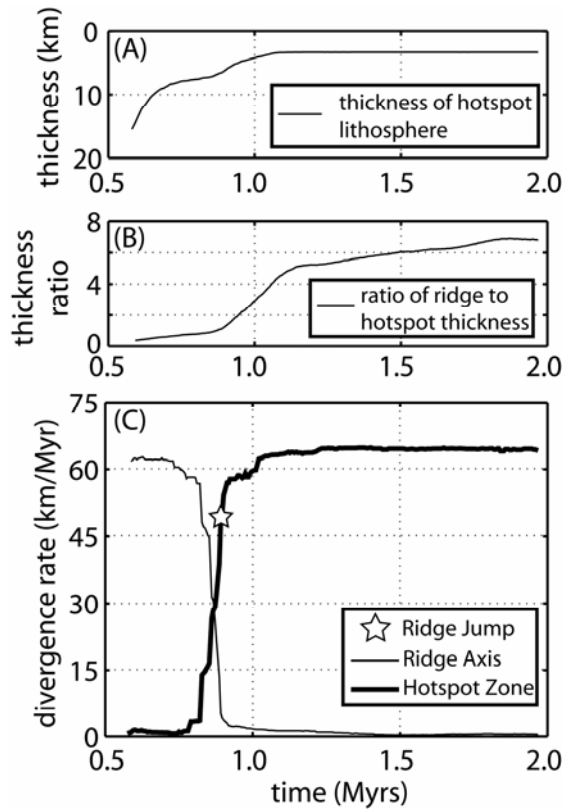
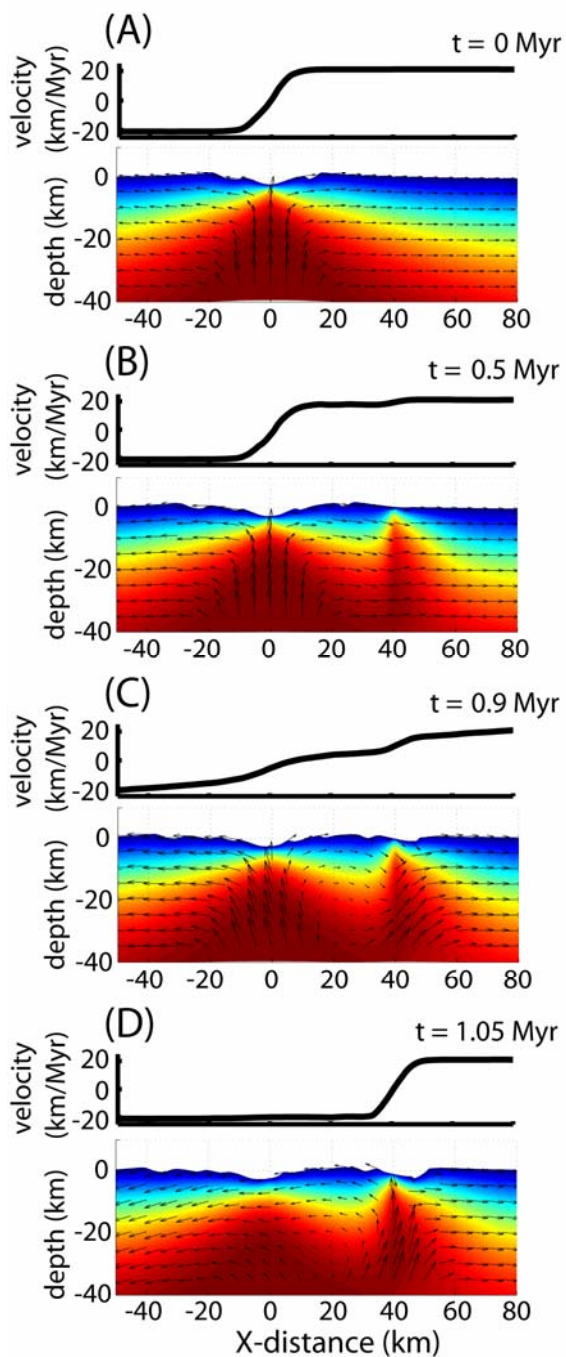


**Figure 3.** (A) Beneath the hotspot, the thickness of the lithospheric thermal boundary layer, defined by the  $1170^{\circ}\text{C}$  isotherm, changes dramatically during the formation of a new ridge axis. (B) The ratio of ridge axis thickness to off-axis lithosphere thickness passes 1 near the time of jump initiation. (C) A ridge jump (star) is defined as complete when the divergence rate off-axis (thick line) is equal to 80% of the original full spreading rate. The case shown here is for a half spreading rate of 30 km/Myr and a  $Q_{\text{hotspot}}-Q_{\text{ridge}}$  of  $161 \text{ kJ m}^{-1} \text{ s}^{-1}$  (see section 3.2 for a description of  $Q_{\text{hotspot}}$  and  $Q_{\text{ridge}}$ ).

### Fixed Hotspot



### Migrating Hotspot

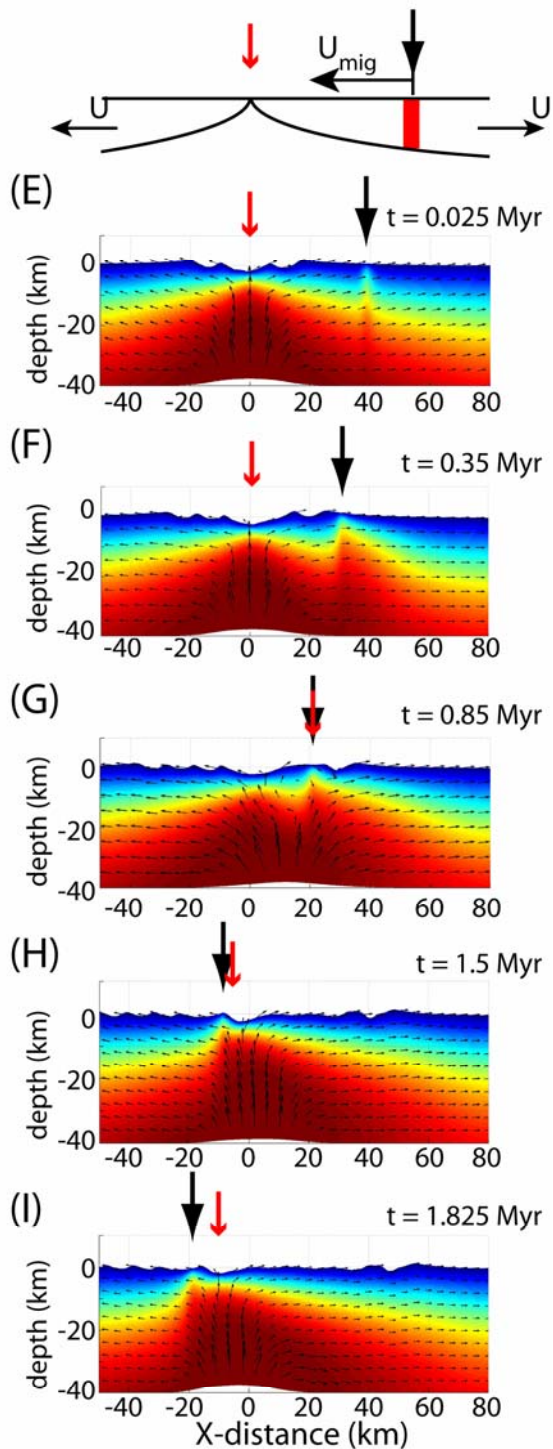


**Figure 4.** Thermal evolution of a ridge jump for a typical case of Type 1 (Type 2 is very similar) involving a hotspot that is fixed with respect to the ridge (left column,  $Q_{hotspot}-Q_{ridge} = 83 \text{ kJ m}^{-1} \text{ s}^{-1}$ ) and Type 3 with a hotspot migrating relative to the ridge at a rate of  $U_{mig} = 30 \text{ km/Myr}$  (right column,  $Q_{ratio}$  varies with time as in figure 8). The half spreading rate is  $U = 20 \text{ km/Myr}$  for both cases. Colors panels show cross-sections of temperature and mantle flow (arrows); profiles above, show depth-averaged velocities within the upper 20 km of the model. (A) An initial square-root-of-age thermal profile is allowed to evolve to steady state and heat is subsequently added at an off-axis location. (B) Heating thins the lithosphere in and around the magma intrusion zone. (C) Beneath the hotspot, mantle upwelling is enhanced as seafloor rifting begins while spreading continues at the ridge axis. (D) Divergence shifts to the location of the hotspot and a new ridge axis is established. In the evolution of Type 3 cases, migration of the hotspot (large black arrow) relative to the ridge leads to ridge jumps and ridge-hotspot migration indicated by changes in the location of maximum divergence (small red arrow). (E) Initially the hotspot is located 40km from the ridge and migrates toward the ridge axis. (F) Hotspot heating thins a broad area of lithosphere. (G) Lithospheric thinning leads to upwelling of hot mantle. (H) After a ridge jump, the hotspot and ridge migrate together. (I) The hotspot moves away from the ridge.

### 3.2 Controlling Parameters

To understand the mechanisms that control the initiation of ridge jumps, I introduce scaling relations involving three basic parameters: the rate of magmatic heating at the hotspot, the rate of magmatic heating at the ridge axis, and the heating rate required to thin the lithosphere. The total magmatic heating rate at the hotspot at the onset of hotspot magmatism ( $t=0$ ) is,

$$Q_{hotspot} = \int_0^{\infty} \int_{-w/2}^{w/2} (q_{hotspot})_{t=0} dx dz . \quad (5)$$

The total heating rate at the ridge axis, also at  $t=0$ , is,

$$Q_{ridge} = \int_0^{z_{crust}} \int_{-w/2}^{w/2} (q_{ridge})_{t=0} dx dz , \quad (6)$$

where  $z_{crust}$  is the depth of the crust (6 km). I re-emphasize that because the actual heating rates (Eqs. 3, 4) are time-dependent, the above parameters are defined based on the temperature structure at  $t = 0$ .

The third heating parameter,  $Q_{thin}$ , is a measure of the heating rate required to thermally dissolve the off-axis lithosphere so that it is as weak as the ridge-axis lithosphere. I define  $D$  to be the lateral distance over which the lithosphere is thinned by the hotspot (Figure 5). To quantify the required heating rate, I examine the balance of heat advected into and out of this zone. The heat being advected into the hotspot magma zone (Figure 5) is measured by the influx of the unperturbed thermal boundary layer ( $T(z)$  at the hotspot center when  $t=0$ )

$$Q_{in} = \rho c_p U \int_0^{z_{max}} T(z)_{t=0} dz, \quad (7)$$

where  $z_{max}$  is the maximum thickness of the lithospheric thermal boundary layer as defined arbitrarily by the 1170°C isotherm at the center of the hotspot. The outgoing heat flux (again at the hotspot center) transported by the “dissolved” lithosphere will be,

$$Q_{out} \sim \rho c_p U \int_0^{z_{max}} T_{asth} dz. \quad (8)$$

Should a ridge jump occur, the net heat advected out of the box of width  $D$  is thus

$$Q_{thin} = Q_{out} - Q_{in} = \rho c_p U \left[ \int_0^{z_{max}} (T_{asth} - T(z))_{t=0} dz \right]. \quad (9)$$

In the absence of conduction out of the seafloor and asthenospheric flow into the base of the box,  $Q_{thin}$  would therefore be the total heating rate in the box required to dissolve the lithosphere in the time it crosses the heating zone. Note that  $Q_{thin}$  incorporates information about both the spreading rate and the age of the seafloor at the hotspot (through the thickness,  $z_{max}$ , in the integration limits).

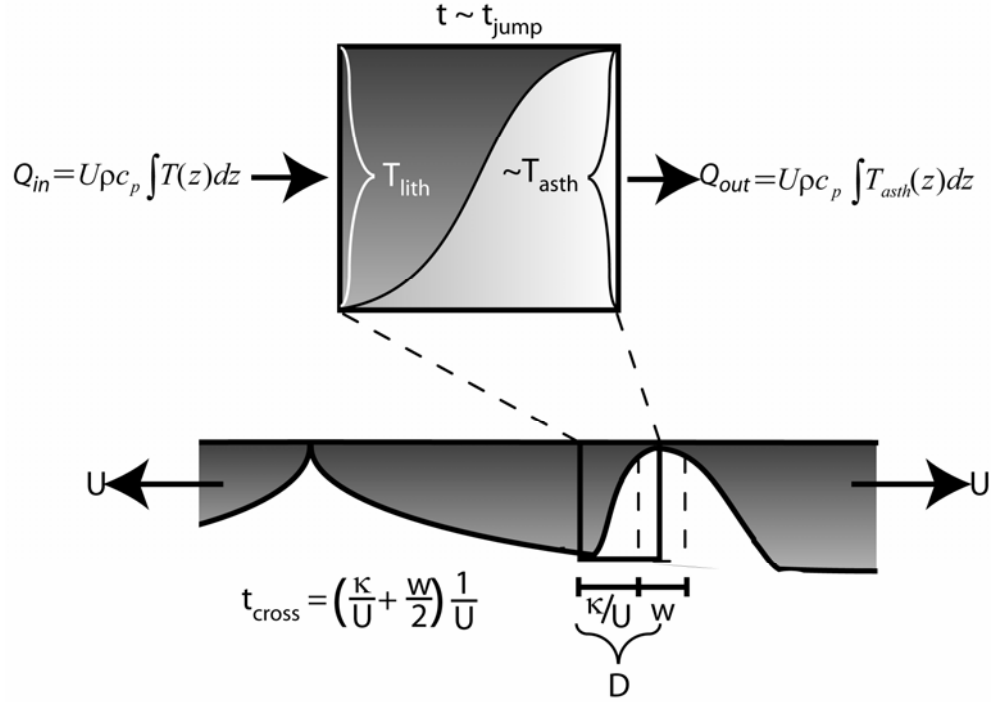


**Figure 5.** Cartoon of the thermal structure immediately prior to a ridge jump. The net advective heat flux passing out of the box,  $Q_{\text{thin}} = Q_{\text{out}} - Q_{\text{in}}$ , is proportional to the depth integrated temperature multiplied by the spreading rate ( $U$ ). The width ( $w$ ) of the zone of magma penetration (dashed box) where heat is added is only a portion of the area over which heating of the lithosphere occurs ( $D$ ). The size of the zone outside of the magma penetration zone,  $(D-w)/2$ , and the time needed to cross the total zone,  $t_{\text{cross}}$ , are described in section 3.2.

The time scale for ridge jump initiation is related to the total width  $D$  that the lithospheric thickness is perturbed. Magmatic heating at the hotspot occurs in a zone of fixed width ( $w$ ), but heat diffusion causes lithospheric thinning over the larger distance,  $D$  (Figure 5). The approximate balance between advection of relatively cool (i.e., normal) lithospheric material toward the hotspot due to spreading ( $Q_{\text{in}}$ ) and diffusion of excess heat away from the hotspot determines the ridge-ward boundary of  $D$ . Equating the timescale needed to advect heat a distance  $D-w/2$  and the characteristic diffusion timescale,  $(D-w/2)^2/\kappa$ , the total width of lithospheric thinning is approximately  $D \sim w/2 + \kappa/U$ . Results will show that an appropriate time scale for the process of magmatic

heating and eventual ridge jump is the time it takes a piece of lithosphere to cross the zone of lithospheric thinning,

$$t_{cross} = D/U \equiv (w/2 + \kappa/U)/U. \quad (10)$$

### 3.3 Scaling: Fixed Hotspot Magma Penetration Zone (Type 1 and 2)

Ridge jumps in Type 1 (no ridge heating) cases are promoted by greater magmatic heating (measured by  $Q_{hotspot}$ ) and are inhibited by thicker (older) or faster moving lithosphere (measured by  $Q_{thin}$ ). Indeed, I find that, for a given value of  $Q_{thin}$ , there is a minimum value of  $Q_{hotspot}$  required to initiate a ridge jump and that this minimum value increases with  $Q_{thin}$  (Figure 6A). Similar behavior is seen with cases of Type 2, but the on-axis heating requires that the minimum value of  $Q_{hotspot}$  for a ridge jump be greater. Examining Type 1 and 2 cases together (Figure 6A), I find that the key parameter determining ridge jump formation is how much  $Q_{hotspot}$  exceeds the on-axis magmatic heating rate (i.e.,  $Q_{hotspot} - Q_{ridge}$ ). Specifically, a ridge jump will occur for sufficient values of  $Q_{hotspot} - Q_{ridge}$  to weaken the plate such that the lithosphere off-axis becomes as weak as or weaker than the lithosphere at the original ridge-axis. Model results indicate that this occurs approximately when (Figure 6A)

$$(Q_{hotspot} - Q_{ridge}) \geq M Q_{thin}^a, \quad (11a)$$

or when the ratio,

$$Q_{ratio} = (Q_{hotspot} - Q_{ridge}) / M Q_{thin}^a \geq 1, \quad (11b)$$

where  $M (=3.4 \times 10^{-3})$  and  $a (=2.68)$  are empirically fit constants.

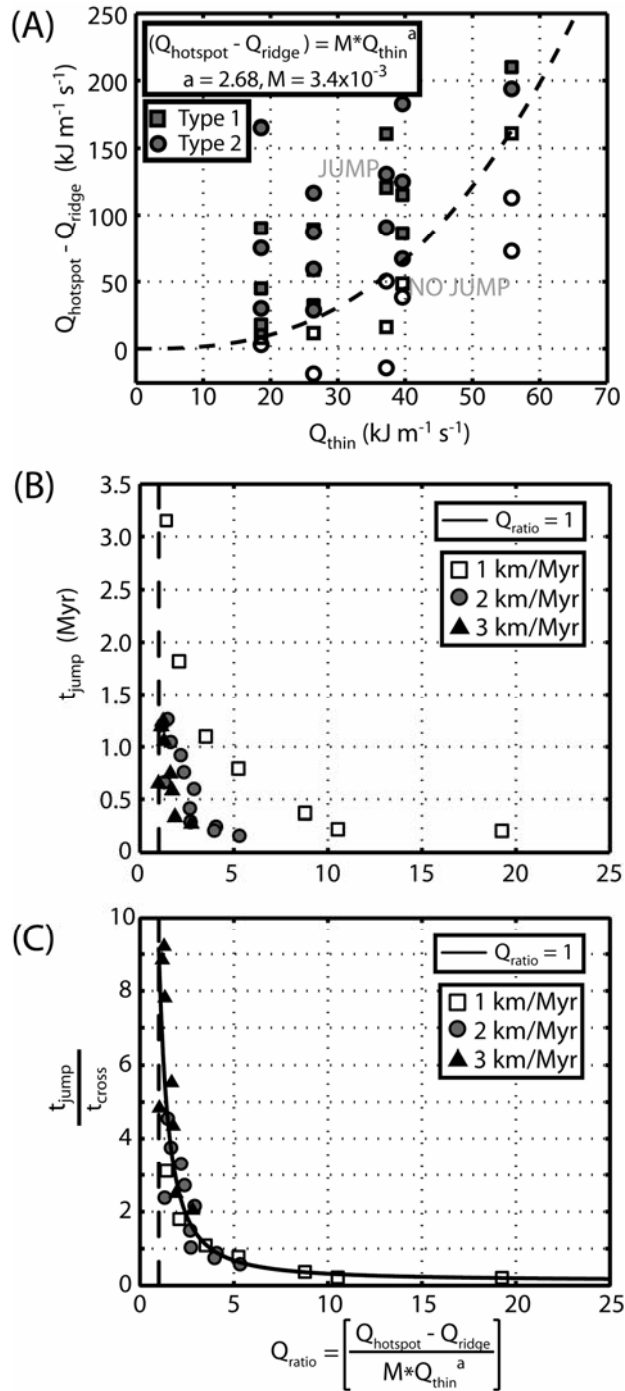


**Figure 6.** (A) Ridge jumps (solid symbols) occur when the value of the integrated heating rate at the hotspot ( $Q_{hotspot}$ ) minus the heat input at the ridge axis ( $Q_{ridge}$ ) is greater than  $MQ_{thin}^a$  where  $a = 2.68$  and  $M = 3.4 \times 10^{-3}$  (dashed line). Values of  $Q_{hotspot} - Q_{ridge}$  below this line do not result in ridge jumps (empty symbols). Results include cases where  $Q_{ridge} = 0$  (Type 1, squares) and cases with heating at the ridge axis (Type 2, circles). (B) The time to achieve a ridge jump ( $t_{jump}$ ) shows an asymptotic

dependence upon  $Q_{ratio}$ . Different symbols mark ridge jump times for different  $Q_{ratios}$  and spreading

The time from the initiation of the hotspot to the formation of a ridge jump ( $t_{jump}$ ) is shown in Figure 6B. For values of  $Q_{ratio}$  near 1, the value of  $t_{jump}$  is large; as  $Q_{ratio}$  increases,  $t_{jump}$  decreases asymptotically toward zero. These results illustrate a wide range of different, sometimes competing, effects. For example, for a given excess heating rate,  $Q_{hotspot}-Q_{ridge}$ ,  $t_{jump}$  increases with increasing spreading rate (and  $Q_{thin}$ ) until the heating rate is insufficient to weaken the lithosphere faster than the material can be advected through the magma penetration zone. Alternatively, for a given spreading rate (and  $Q_{thin}$ ), increases in  $Q_{hotspot}-Q_{ridge}$  will decrease the time required to achieve a ridge jump as material within the hotspot heating zone is heated more rapidly. Scaling  $t_{jump}$  by the time required to cross the zone of lithospheric thinning,  $t_{cross}$ , allows the relationship to be described by a single, empirical scaling law (Figure 6c),

$$\frac{t_{jump}}{t_{cross}} = 7.82 \cdot Q_{ratio}^{-2} + 1.25 \cdot Q_{ratio}^{-1} + 0.117. \quad (12)$$

Lastly, the width  $w$  of the off-axis heating zone also affects the time and the minimum integrated heating rate,  $Q_{hotspot}$ , required to initiate a ridge jump (Figure 7). For a fixed  $Q_{hotspot} = 151 \text{ kJ m}^{-1} \text{ s}^{-1}$ , a half spreading rate of 20 km/Myr, and a plate age of 2 Myr I varied  $w$  between 1 and 40 km. Models predict that as  $w$  increases from 1 km to 12 km,  $t_{jump}$  decreases from 0.575 Myr to 0.325 Myr. For  $w$  increasing from ~15 km to 40 km, the trend reverses such that  $t_{jump}$  increases to 0.75 Myr. This non-monotonic relationship is complex and is likely caused by the interaction of several factors. For example, on one hand, a wider heating zone implies a large value of  $t_{cross}$ , which according to (12) would tend to increase  $t_{jump}$ . But on the other hand, a wider

heating zone results in a smaller average value of  $Q_{thin}$  which is a consequence of higher average initial temperatures across the heating zone due to the more rapid shoaling of isotherms on the ridgeward side of the heating zone compared to the opposite side. The lower average  $Q_{thin}$  causes a larger average  $Q_{ratio}$ , and by (12), tends to increase  $t_{jump}$ . Thus, in the above test cases, increasing  $w$  up to widths comparable to those of the neovolcanic zone on Iceland results in values of  $t_{jump}$  within about 25% of that obtained by the reference width of 2 km.

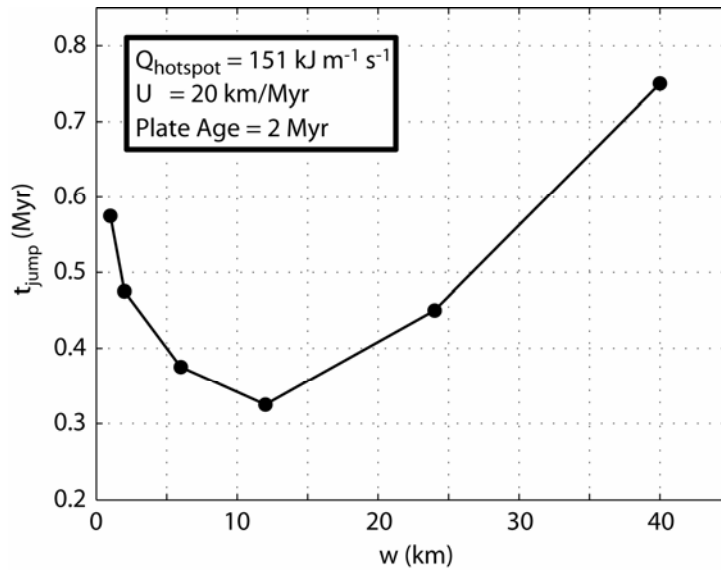


**Figure 7.** Models are run with a fixed  $Q_{hotspot}$ , spreading rate (20 km/Myr) and lithospheric age (2 Myr) at the center of the heating zone for off-axis heating zone widths,  $w$ , from 1 to 40 km.

### 3.4 Time Evolution: Migrating Magma Intrusion Zone (Type 3)

For Type 3 cases I initiate a hotspot at a distance 40 km to the right of the ridge axis at  $t=0$ . The hotspot migrates to the left (or the ridge migrates to the right in the hotspot reference frame) at a specified rate,  $U_{mig}$ . As the hotspot migrates toward the ridge axis, the lithosphere thins asymmetrically over a broad area (Figure 4).

Eventually, if the hotspot heating rate is sufficient, rifting begins at the hotspot. Similar

to Type 1 and 2 cases, incipient rifting causes hot mantle to rise and further weaken the new rift which is followed by further rifting, and soon thereafter a ridge jump. The new ridge axis then migrates along with the hotspot. For cases in which the hotspot migration rate,  $U_{mig}$ , equals or exceeds  $U$ , models predict the hotspot and ridge to eventually separate. The hotspot then proceeds to move away from the ridge axis. For cases in which the hotspot heating rate is too small, the ridge never jumps and the hotspot migrates across the model with little effect on the lithosphere.

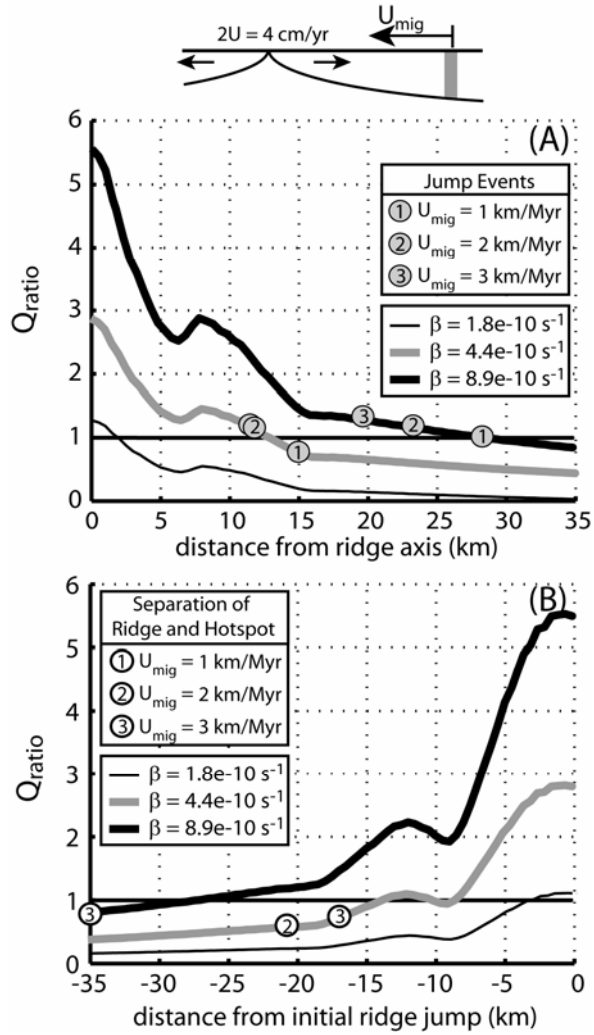
### 3.5 Scaling: Migrating Magma Intrusion Zone (Type 3)

Figure 8a displays  $Q_{ratio}$ , calculated from Eqs. 5-7 and the initial temperature structure at time  $t = 0$  as a function of the distance from the ridge. In this plot,  $Q_{ratio}$  is computed based on the  $Q_{thin}$  and  $Q_{hotspot}$  values that are present at  $t=0$  just before the initiation of magmatic heating, not the time-dependent temperatures throughout the simulation. Different curves are for different values of  $\beta$  (heating rate magnitude, Eq. 2), but for the same spreading rate (20 km/Myr). For each value of  $\beta$ , I explore three different hotspot migration rates (relative to the ridge axis),  $U_{mig} = 10, 20$  and  $30$  km/Myr.

When the hotspot migrates toward the ridge, the axis jumps to the hotspot at a location (grey circles Figure 8a) that depends upon  $Q_{ratio}$  and the migration rate of the hotspot. Faster migration rates initiate ridge jumps closer to the ridge axis than do slower migration rates (i.e. a faster migration rate moves the hotspot closer to the ridge in the time required to sufficiently thin the lithosphere). Like the non-migrating cases (Type 1, 2), jumps only occur when the  $Q_{ratio}$  is near to or greater than 1. The lowest

value of  $\beta$  only achieves a  $Q_{ratio} \geq 1$  very close to the ridge axis and therefore a ridge jump does not occur before the hotspot migrates to the original ridge location in the numerical simulations.

After a ridge jump has occurred, the ridge and hotspot are predicted to migrate together for a distance that also depends on  $Q_{ratio}$  and  $U_{mig}$  (Figure 8b). Here  $Q_{ratio}$  is the same function of  $Q_{hotspot}$  and  $Q_{thin}$  based on the  $t=0$  temperature profiles, but is plotted as a function of distance from the new ridge axis right after it jumped. The location of separation occurs closer to the ridge axis with increasing  $U_{mig}$ . For cases in which the  $Q_{ratio}$  remains  $> 1$  or  $U_{mig} < U$ , the ridge remains captured and continues to migrate with the hotspot over the distance spanned by the numerical box.



**Figure 8.** Predicted values of the  $Q_{ratio}$  (solid curves) versus distance from the ridge axis at three different values of  $\beta$  (Eq. 2). (A) When the hotspot migrates toward the ridge, a ridge jump is predicted to occur when  $Q_{ratio} \geq \sim 1$ . Ridge jumps (grey circles) occur closer to the ridge axis for larger migration rates,  $U_{mig}$ . (B) After a ridge jump, the ridge and hotspot migrate together until  $Q_{ratio}$  (see text) falls below 1. When  $U_{mig} < U$  they migrate together, but when  $U_{mig} \geq U$  they separate at the shown locations (white circles). The local peak in the  $Q_{ratio}$  at distances of 5-10 km from the ridge axis is associated with changes in the temperature profile due to faulting.

#### **4. Discussion: Importance of hotspot magmatic heating to natural systems**

##### *4.1 To Jump or Not to Jump: Iceland versus the Galápagos*

There are many near-ridge hotspots around the globe, but only some display recent ridge jumps. I focus on two example systems for which the tectonic evolution is well understood and for which hotspot magma fluxes can be estimated: Iceland-MAR where ridge jumps have recently occurred and Galápagos where ridge relocations have recently ceased.

The Galápagos spreading center (GSC) has moved north relative to the hotspot for tens of Myr [Hey, 1977; Wilson and Hey, 1995]. Between ~5-10 Ma, the GSC and Galápagos were located very close to each other and the ridge experienced several distinct jumps. Between ~2.5-5 Ma, the GSC was “captured” by the hotspot and remained close to it, but did not display discrete jump activity at the resolution of the available geophysical data. Since ~2.5 Ma, the GSC has remained separate from the Galápagos hotspot and has not appeared to have jumped. At the present day, the segments west and east of the 90.5°W transform fault are 260 and 200 km north of the hotspot, respectively.

Iceland was the site of at least four major jumps of the Mid-Atlantic Ridge (MAR) in the last ~16 million years ([Jóhannesson, 1980], Figure 1). Migration of most of the MAR to the northwest at approximately 5-17 km/Myr [Torsvik *et al.*, 2001; Jones, 2003] with respect to the hotspot was punctuated by jumps of individual ridge segments on Iceland toward the hotspot. Recent dating of dikes along a 350 km transect across northern Iceland indicates that the most recent jump (initiated at ~7.8 Ma)

occurred into ~1 Myr-old lithosphere from the Skagafjordur rift to the Northern Volcanic Zone (NVZ) [Garcia *et al.*, 2003]. Geological estimates, however, place the former ridge axis tens of kilometers to the west on the Skagi peninsula suggesting a jump into 4 Myr old seafloor [Hardarson *et al.*, 1997]. I thus bracket the seafloor age to which jumps occur between 1-4 Myrs. After initiation of the ridge jump, coeval rifting of the NVZ and the former ridge axis ensued for approximately 3.5 Myr with the old rift dying at ~3 Ma [Hardarson *et al.*, 1997].

Using the relationship between  $Q_{hotspot}$ - $Q_{ridge}$  and  $Q_{thin}$  (Figure 6A), I can now assess whether thermal weakening alone is likely to have initiated the ridge jumps at the Iceland and Galápagos hotspots.  $Q_{thin}$  can be estimated for a given location based upon the age of the overlying lithosphere and a basic square-root-of-age cooling profile. To calculate  $Q_{hotspot}$ , the heat transferred to the lithosphere is assumed to be equal to the magma flux times the latent heat of fusion of the magma for latent heat values between 400 and 600 kJ/kg. This assumption will tend to maximize the effects of magmatic heating at both the ridge and hotspot, so the effect of this assumption on  $Q_{hotspot}$ - $Q_{ridge}$  is not clear at this point. The magma flux used is based upon crustal thicknesses derived from geophysical data.  $Q_{ridge}$  is calculated in a similar manner as  $Q_{hotspot}$ , but with a magma flux based on the spreading rate of the given ridge and a crustal output at that ridge.

For Iceland,  $Q_{thin}$  is calculated for 1-4 Myr old lithosphere (Eq. 7).  $Q_{ridge}$ , is calculated assuming a 20-km-thick crust (crustal thickness estimate for western Iceland [Allen *et al.*, 2002]) multiplied by a spreading rate of 20 km/Myr.  $Q_{hotspot}$  is estimated based on 10-25km of additional crust (45km directly above the hotspot or 30km in the

NVZ minus 20km in western Iceland) assumed to be associated with the hotspot and a full spreading rate of 20 km/Myr.

For the Galápagos,  $Q_{ridge}$  is estimated from the maximum crustal thickness of 9km at the ridge axis just north of the hotspot [Canales *et al.*, 1997] and a full spreading rate of 60 km/Myr. I estimate  $Q_{hotspot}$  based on the average magmatic flux estimated for the islands of  $1.3 \times 10^5 \text{ km}^3/\text{Myr}$  (per km parallel to the ridge) [Ito *et al.*, 1997].  $Q_{thin}$  is calculated based on 8 to 8.5 Myr-old lithosphere at the current presumed location of the hotspot (Fernandina Island).

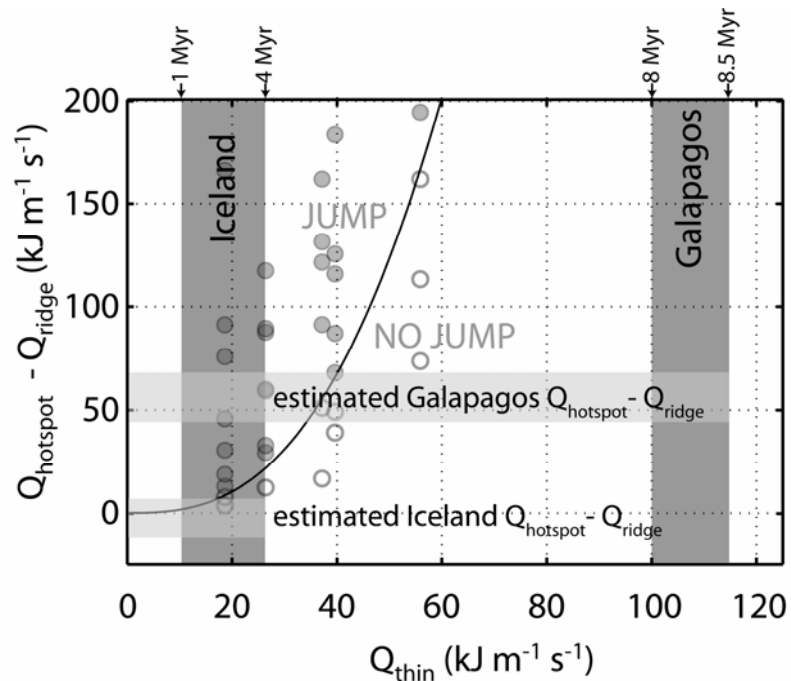


**Figure 9.** Estimates of  $Q_{hotspot}-Q_{ridge}$  (light grey bars) and  $Q_{thin}$  (dark grey bars) for the Galápagos and Iceland hotspots compared to the theoretical limit of  $Q_{ratio}$  (black curve, also Figure 6) suggest that the magma flux at Iceland could be sufficient to produce a ridge jump to 1.5 Myr. old seafloor at the slow spreading MAR (20 km/Myr full rate). Estimates were made on 1-4 Myr and 8-8.5 Myr old lithosphere for Iceland and the Galápagos respectively (top arrows). The estimated magma flux at the Galápagos, although larger, is clearly insufficient to initiate a ridge jump near the faster spreading Galápagos Spreading Center (60 km/Myr full rate) and to the older seafloor at the current location of the hotspot. See section 4.1 of the text for more details on estimates of  $Q_{hotspot}$ ,  $Q_{ridge}$  and  $Q_{thin}$ . The circular symbols show all model results in Figure 6.

Figure 9 shows the estimated values of  $Q_{hotspot}-Q_{ridge}$  for Iceland and the Galápagos versus the estimates of  $Q_{thin}$  at these hotspots. Figure 10 illustrates the model estimates of the required excess heat and magma fluxes for the appropriate spreading rates and seafloor ages. Comparisons to the model results suggest that lithospheric heating due to magma penetration alone is insufficient to cause the Galápagos Spreading Center to jump to the current hotspot location. Taking the estimated  $Q_{hotspot}-Q_{ridge}$  for the Galápagos and assuming constant spreading rate through time, the maximum age of lithosphere for which the Galápagos can initiate a ridge jump is  $\sim 1$  Ma. These results are consistent with the lack of a Galápagos ridge jump over the past few million years as the ridge migrated away from the hotspot [Wilson and Hey, 1995].

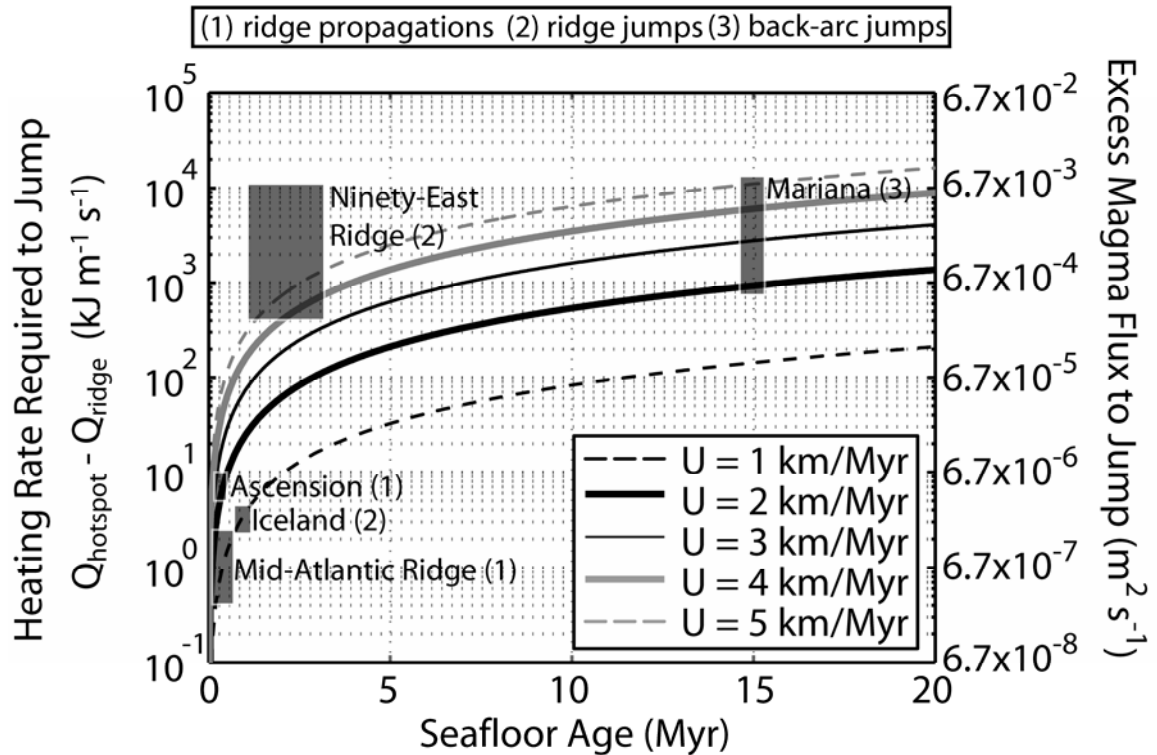


**Figure 10.** Curves show predictions of Eq. (11) for the excess magma fluxes and excess heating rates required to produce ridge jumps for an example range of spreading rates (1-50 km/Myr). Boxes show the required fluxes that are predicted for four settings

based on estimates of spreading rates and seafloor age to which ridge relocations have been documented [Brozena and White, 1990; Cormier and Macdonald, 1994; Krishna et al., 1995; Sempéré et al., 1995; Searle et al., 1998; Garcia et al., 2003; Sdrolias et al., 2004]. These example settings include ridge relocations in the form of (1) ridge propagations, (2) ridge jumps and (3) back-arc ridge jumps.

Estimates for Iceland, however, show a different picture. In this case, for jumps to seafloor up to 1.5 Myr old, the upper range of magma flux of the Iceland hotspot (in excess of the hotspot-influenced ridge axis) exceeds that predicted by the scaling law to cause a ridge jump. While the study of dike ages suggests that the Icelandic ridge jumps occurred to crust as young as 1 Myr old, the relation of the dated dikes to the former ridge axis is unclear due to a lack of trace-element data. It is thus likely that the ridge jumped to older crust. A jump to crust of 4 Myr, based on the geologic evidence [Hardarson et al., 1997], would likely require other mechanisms in addition to magmatic heating to initiate rifting. Although seafloor age is a significant factor, the most important difference between the Galápagos and Iceland localities is the spreading rate. Despite the lower igneous magma flux associated with the Icelandic hotspot, the slow moving lithosphere allows greater time to heat a given piece of lithosphere (Figure 10). This is the main reason that magmatic heating is predicted to be more important at Iceland than at Galápagos.

Another model prediction to compare with observations is the duration of coeval rifting while the ridge jump is in progress. Models predict a duration of coeval rifting of 0.2-0.8 Myr that is an order of magnitude shorter than the ~3.5 Myr duration estimated during the last ridge jump on Iceland [Hardarson et al., 1997]. This discrepancy further suggests either that magmatic heating changed in time differently

than simulated in the models, or that different processes are also important to the evolution of Icelandic ridge jumps.

#### *4.2 Hotspot-Ridge Migration*

Results from Type 3 (migrating hotspot) cases show that during the time in which the ridge is “captured” by the hotspot, the hotspot and ridge-axis migrate together, but do not exhibit discrete jumps. After the separation of the ridge and hotspot, no further ridge jump behavior occurs due to the low value of the  $Q_{ratio}$ . On Earth there is evidence for ridge “capture” via steady ridge migration as well as discrete ridge jumps. The large distances involved in jumps at the Ninety-East Ridge and Shatsky Rise evident in magnetic anomalies [*Krishna et al.*, 1995; *Nakanishi et al.*, 1999; *Krishna and Rao*, 2000], as well as the age dating of dikes on Iceland [*Garcia et al.*, 2003] suggest that ridge jumps at these locations are discrete events. Alternatively, after the last jump of the Galápagos Spreading Center (~5 Ma), asymmetric spreading kept the ridge close to the hotspot for ~2.5 Myr probably without discrete jumps [*Wilson and Hey*, 1995].

The failure of the models to predict discrete jumps as the ridge moves away from the hotspot center, suggests that processes other than those considered here are at work. For example, upwelling, warm mantle plumes thermally and mechanically thin the lithosphere and can influence melt migration through changes to the slope of the lithosphere [*Sparks and Parmentier*, 1991; *Kincaid et al.*, 1996; *Hall and Kincaid*, 2003; *Hall and Kincaid*, 2004]. The amount of lithospheric thinning depends on the ratio of the thinning rate to the hotspot migration rate [*Jurine et al.*, 2005]. In the case

of a migrating, ridge-centered plume, the thin lithosphere at the ridge axis could focus melt to the ridge [*Sparks and Parmentier, 1991*] while the plume moves off-axis. This could keep melt focused to the ridge axis until the plume migrates a sufficient distance such that plume-generated magma cannot make it back to the ridge. This behavior would result in a gap in hotspot volcanism after a ridge jump, which could be tested with further field observations. A similar change in the pattern of volcanism due to the slope of the lithosphere is proposed by *Sleep [2002]* for plumes approaching ridges. Another process that may influence the formation of repeated ridge jumps is variations in magma flux. Iceland, for example, may experience pulses of magmatism indicated by anomalous V-shaped ridges along the Mid-Atlantic Ridge [*Vogt, 1971; Ito, 2001; Jones et al., 2002*]. Variations in magma flux could change  $Q_{ratio}$  below and above the critical value to cause discrete jumps. Also, fracturing of the lithosphere due to propagating dikes will mechanically weaken the plate and could affect the initiation of ridge jumps.

#### *4.3 Relocation of the Mariana Back-arc Spreading Center*

Although I have focused on jumps of mid-ocean ridges to the location of nearby hotspots, the Mariana back-arc also experienced a jump in the location of seafloor spreading. Subduction of the Pacific plate beneath the Philippine Sea plate initiated at ~50 Ma with arc volcanoes first forming at ~40 Ma [*Hussong and Uyeda, 1981; Taylor, 1992; Cosca et al., 1998*]. After ~10 Myr of volcanism, an initial rift of the volcanic arc and formation of seafloor spreading occurred at ~30Ma [*Hussong and Uyeda, 1981*]. A reorganization of plate spreading in SE Asia approximately 15Ma [*Sibuet et al., 2002*],

caused the cessation of seafloor spreading [Briais *et al.*, 1993]. Continued volcanism at the arc, which remained near the subduction front, led to the creation of a rheological weak zone [Steckler and tenBrink, 1986] and initiation of a new seafloor spreading center at ~7Ma [Sdrolias *et al.*, 2004].

A ridge jump due to magmatic heating of near-ridge lithosphere associated with arc volcanism is consistent with the conditions of the model. The cessation of spreading at ~15Ma, suggests that  $Q_{ridge}$  decreased to 0, promoting the initiation of a new spreading ridge at the arc due to the corresponding increase in  $Q_{hotspot}-Q_{ridge}$  (i.e.  $Q_{ratio}$ ). The increased value of  $Q_{hotspot}-Q_{ridge}$ , compounded by the cooling of the old ridge, may have decreased the necessary magma flux at the back arc required to relocate rifting (Figure 10). Thus, a smaller back-arc magma flux than required during active seafloor spreading may initiate a new rift due to magmatism. In fact, magmatic heating may have promoted the initial arc rifting itself. There is evidence that relocation of back-arc spreading may also be associated with arc magmatism at other subduction zones, such as in the Mediterranean [Faccenna *et al.*, 2001].

#### 4.4 Ridge Propagation on the Mid-Atlantic Ridge

In the past 10 Myr, small-scale relocations of the Mid-Atlantic Ridge (MAR) have occurred through propagation of axis segments [Pariso *et al.*, 1995; Sempéré *et al.*, 1995; Searle *et al.*, 1998]. Many of the relocations are not considered to be affected by hotspot volcanism, but Sempéré *et al.* [1995] find that, between 29°N and 31°30'N, the segments with the largest propagation rates are associated with the largest volume of crust (~9 km of crust at the segment center versus ~7 km for the weaker segments).

Ridge propagation has been widely understood in terms of fracture mechanics. The above correlation is consistent with the notion that thicker crust at segment centers elevates the pressure in the axial lithosphere and thus enhances the “driving pressure” (difference between pressure on a crack surface and in the far-field pressure) for ridge propagation [Phipps Morgan and Parmentier, 1985]. I propose that enhanced magmatism could further increase the driving pressure of propagating ridge segments by reducing the tensile strength of the axial lithosphere.

Assuming that magmatic weakening of the plate is important to propagation of the above segments, I can use the scaling relationships predicted by the model to estimate the excess magma flux required to promote rift propagation of one segment over another segment (Figure 10). To initiate rifting  $Q_{ratio}$  must be greater than 1 and thus the required excess heating rate ( $Q_{hotspot} - Q_{ridge}$ ) is equal to  $MQ_{thin}^a$ . I convert this excess heat estimate to a predicted excess magma flux using a latent heat of 500 kJ/kg (see section 4.1). The model results predict that to initiate propagation the segment must have an excess magma flux between  $\sim 4 \times 10^{-7}$  and  $\sim 1 \times 10^{-6} \text{ m}^2 \text{ s}^{-1}$  ( $Q_{hotspot} - Q_{ridge} = 0.8 - 4 \text{ kJ m}^{-1} \text{ s}^{-1}$ ) for age offsets between 0.4 and 1 Myr. (Figure 10). For a half-spreading rate of 12 km/Myr, the above excess flux corresponds to an excess crustal thickness of 1000-2500 m at the propagating ridge relative to the dying segment. This range is consistent with the variations in crustal thickness estimated for the most rapidly propagating segments of the MAR between 29°N and 31°30'N [Pariso et al., 1995; Sempéré et al., 1995]. The obvious shortcoming of this study is the 2D geometry; 3D models are clearly necessary to more completely test the effects of magmatism on ridge propagation.

## 5. Conclusions

I have used 2D thermo-mechanical models to explore one of several possible factors that can promote jumps of mid-ocean ridge segments: heating of the lithosphere due to hotspot magmatism. I have quantified the effects of plate age, spreading rate, ridge migration rate, and the excess magmatic heating rate. Three fundamental parameters effectively describe the behavior of the model: 1)  $Q_{hotspot}$ , the initial integrated heating rate within the specified width of the heating zone; 2)  $Q_{ridge}$ , the initial integrated heating rate at the ridge axis; and 3)  $Q_{thin}$ , the instantaneous heating rate required to initiate a ridge jump. The key time scale is  $t_{cross}$ , which is the time needed to advect a piece of the lithosphere moving at the spreading rate through the zone of lithospheric thinning.

To initiate a ridge jump the function  $Q_{ratio} = (Q_{hotspot} - Q_{ridge}) / M Q_{thin}^a$  with  $a = 2.68$  and  $M = 3.4 \times 10^{-3}$  must exceed 1. For cases in which  $Q_{ratio} > 1$ , the time required to initiate a ridge jump is on the order of 0.25-4 Myr. When scaled by  $t_{cross}$ , the dimensionless time to a jump ( $t_{jump}/t_{cross}$ ) decreases nonlinearly with increasing  $Q_{ratio}$ . Increasing the excess hotspot heating rate ( $Q_{hotspot} - Q_{ridge}$ ) increases  $Q_{ratio}$  and decreases the time to a jump; increasing the spreading rate decreases  $Q_{ratio}$  and thus increases the time to a jump. Additionally, the time required to initiate a ridge jump increases (or decreases) for a hotspot located on older (or younger) seafloor.

Hotspot migration toward a ridge axis is also found to produce ridge jumps for values of  $Q_{ratio} \geq 1$ . Once  $Q_{ratio}$  exceeds 1, the age of lithosphere to which a jump occurs depends on the hotspot migration rate relative to the ridge, with faster migration

rates jumping to younger seafloor. After a ridge jump, the ridge and hotspot are predicted to migrate together until the  $Q_{ratio}$  (as defined relative to the initial jump location) falls below 1. At this point, the ridge and hotspot separate and no further ridge jumps are predicted. The location where the hotspot separates from the ridge axis also depends on the migration velocity, with faster migration rates separating earlier. I conclude that for ridges migrating away from a hotspot, steady hotspot magmatic heating alone will “capture” the ridge axis, but is unlikely to initiate repeated discrete ridge jumps. Other processes not considered here may be important to forming repeated discrete ridge jumps.

Application of the model results to Iceland reveals that magmatic heating alone is capable of producing ridge jumps of the slow-spreading Mid-Atlantic Ridge in lithosphere younger than  $\sim 1.5$  Ma for high-end magma flux estimates. In contrast, hotspots on older seafloor, or at faster spreading rates, including those with larger magma fluxes—like the Galápagos—are unlikely to initiate a ridge jump. This prediction is consistent with the lack of observed ridge jumps at the Galápagos over the last  $\sim 5$  Myr. Model results also provide a plausible mechanism for ridge jump formation in non-hotspot affected regions such as back-arc settings like the Marianas and ridge propagations along the Mid-Atlantic Ridge.

## Chapter 4:

### **Repeated ridge jumps associated with plume-ridge interaction, melt transport and ridge migration**

#### **1. Introduction**

Mantle plume-ridge interaction significantly alters the crustal thickness [Canales *et al.*, 2002], segmentation pattern [Jones, 2003], depth [Canales *et al.*, 1997], axial morphology [Canales *et al.*, 1997; Sinton *et al.*, 2003; Christie *et al.*, 2005], and location of mid-ocean ridges [Sæmundsson, 1974; Jóhannesson, 1980; Wilson and Hey, 1995; Hardarson *et al.*, 1997; Muller *et al.*, 2001b]. Changes in ridge location are often caused by a plume “capturing” a nearby ridge-axis through asymmetric spreading [Muller *et al.*, 1998; Muller *et al.*, 2008], increased ridge propagation [Hey, 1977; Wilson and Hey, 1995], and discrete shifts of the ridge axis [e.g. Hardarson *et al.*, 1997], which I call ridge jumps. Numerous observations of ridge-jumps associated with plume-ridge interaction [e.g. Hey, 1977; Jóhannesson, 1980; Mammerrickx and Sandwell, 1986; Brozena and White, 1990; Muller *et al.*, 1993; Krishna *et al.*, 1995; Small, 1995; Hardarson *et al.*, 1997; Nakanishi *et al.*, 1999; Krishna and Rao, 2000; Briaies and Rabinowicz, 2002] suggest that by transferring sections of lithosphere from one plate to another they play a significant role in the long-term evolution of the tectonic plates.

Ridge jumps are observed to occur over distances from  $\sim 10^1$  km at Iceland [Hardarson *et al.*, 1997; Garcia *et al.*, 2003] to  $\leq 800$  km at Shatsky Rise and often occur repeatedly along a single section of ridge axis as the ridge migrates away from a

nearby hotspot. For example, Iceland has experienced at least four ridge jumps in the last 16 Myr [Jóhannesson, 1980] as the Mid-Atlantic Ridge has migrated at 5-17 km/Myr to the NNW relative to the hotspot [Torsvik *et al.*, 2001; Jones, 2003]. Repeated ridge jumps are also observed at the Galápagos [Hey, 1977], the Ninety-East Ridge [Krishna *et al.*, 1995; Krishna and Rao, 2000], and possibly the Louisville hotspot [Small, 1995].

Two of the principal factors necessary to initiate a ridge jump are weakening of off-axis lithosphere and a stress field which promotes rifting in the same location. One mechanism proposed to weaken the lithosphere is the thermal and physical removal of material from the bottom of the plate by a laterally spreading mantle plume (i.e. plate “rejuvenation”) [e.g. Ribe and Christensen, 1994; Li *et al.*, 2004]. Evidence of plate thinning caused by an upwelling mantle plume has been suggested from seismic studies of the Hawaiian hotspot where an observed seismic discontinuity could reveal a thinning of the lithosphere by as much as ~50% [Li *et al.*, 2004]. Another proposed weakening mechanism is heating of the lithosphere as magma passes through it [Mittelstaedt *et al.*, 2008]. In fact, magmatic weakening, including heating, is suggested to be important to the initiation of rifting in the Gulf of Aden [Kendall *et al.*, 2005], during the initial breakup of the North Atlantic [Nielsen *et al.*, 2002], to the creation of continental micro-plates [Muller *et al.*, 2001b] and to play a key role in determining the location of hotspot islands [Hieronymus and Bercovici, 2001]. In addition to these weakening mechanisms, non-lithostatic stresses are felt at the ridge boundary due to far-field tectonic stresses, shear tractions on the base of the lithosphere induced by a laterally spreading plume, and plate-parallel gravitational stresses due to buoyant uplift

of the lithosphere. The combination of the above mechanisms is suggested to induce fracturing of the lithosphere, enhance off-axis magmatism [*Mittelstaedt and Ito, 2005*], and may contribute to the initiation of ridge jumps.

In previous work [*Mittelstaedt et al., 2008*], colleagues and I examined the contribution of magmatic heating to the initiation of ridge jumps by imposing a magmatic heating zone of fixed width and a prescribed heating rate proportional to the temperature contrast between magma and the lithosphere. This work was important in revealing the physical effects of magmatic heating under a variety of spreading rates (10-30 km/Myr), hotspot-ridge separation distances (20-60 km), and ridge migration rates (10-30 km/Myr). The results suggest that magmatic heating alone can cause ridge jumps, but only on young, slow-moving lithosphere. One shortcoming of these models was the inability to predict repeated ridge jumps as the ridge migrates away from the plume. The absence of repeated ridge jumps in those models may be due to the neglect of several processes that are likely to be important to rift initiation including the thermo-mechanical effects of a hot, upwelling plume on the lithosphere and changes in magmatic heating caused by varying magma flux through the lithosphere in response to changes in melt generation and transport from below.

This study builds upon our previous work by including the contribution of a plume-like upwelling and a new method for magmatic heating that is governed by mantle melting and melt transport. I quantify the effects of these processes on the initiation of ridge jumps in stationary and migrating systems, for different plume-ridge separation distances, spreading rates, plume temperatures and buoyancy fluxes, and different heating rates of the lithosphere by magma. Results suggest that the addition of

a warm upwelling plume inhibits ridge jumps by heating the ridge axis lithosphere, and promotes ridge jumps through changes to the lithospheric stress field and increasing the off-axis melt supply. I find that the heating rate required to initiate a ridge jump is a non-linear function of the plate spreading rate and the age of the lithosphere. The new models are the first to successfully predict repeated ridge jumps but only over a restricted range of spreading rate, ridge migration rate and magmatic heating rate. Additionally, magmatic heating of the lithosphere predicted by our models provides another possible mechanism for thinning of the lithosphere above intra-plate plumes, such as Hawaii.

## **2. Conceptual and Mathematical Model**

### *2.1 Conceptual Model*

Figure 1 illustrates a conceptual model for a ridge jump caused by plume-ridge interaction. A relatively hot off-axis mantle plume rises, melts, and spreads laterally as it encounters the lithosphere. The buoyant melt percolates vertically through the mantle until it reaches the top of the melting region (i.e. the solidus) where it accumulates within a high-porosity layer just below the cooler, low permeability lithosphere. Melt flows along the solidus toward a local depth minima (e.g. the ridge axis) where it accumulates and builds pressure. When the melt pressure is high enough beneath the brittle lithosphere, fractures open and allow magma to travel to the seafloor. As the magma passes through the plate, it conducts heat to the lithosphere reducing its strength. Additional weakening occurs as the spreading plume thermally and

mechanically erodes the underside of the plate. If the combined plume and magmatic weakening are sufficient, stresses associated with plate motion and the spreading plume initiate rifting off-axis. Eventually, a new ridge axis is formed and spreading on the former axis ceases.

## 2.2 Mathematical and Numerical Model of Viscous Mantle Flow

I use the finite-element code CITCOM [Moresi and Solomatov, 1995; Zhong *et al.*, 2000] to solve the 2-D equations of conservation of energy, momentum, and mass in a visco-plastic mantle. The model domain measures 1200 km laterally and 400 km vertically and is made up of a grid of 512 by 128 elements. The height and width of each element range between 1.5km and 3.2km with the highest resolutions in the upper 50km and in the region of plume-ridge interaction. The sides of the model are normal traction free at all depths >80 km with a horizontal velocity imposed at shallower depths to drive plate spreading (Figure 2). The horizontal upper surface is shear traction free and has a zero vertical velocity while the bottom boundary is traction free. The side boundaries have an imposed zero horizontal temperature gradient and the top and bottom are set to 0°C and 1300°C temperatures respectively. Thermally, the initial temperature condition is that of a plate cooling model in which the lithosphere is thinnest at the ridge and increases to a maximum thickness of 125 km [e.g. Parsons and Sclater, 1977]. To initiate a plume-like upwelling, a hot patch with a Gaussian temperature distribution is imposed along the bottom of the model. Although varied in some cases, the maximum plume temperature is set to  $\Delta T_p = 300^\circ\text{C}$  and the width of

the Gaussian  $\Delta x_p = 40$  km which results in a plume buoyancy flux of  $\sim 2000$  kg/s similar to estimates for many hotspots [Sleep, 1990]. See the list of symbols on page (xi) for all model parameters.

Viscous deformation in the model depends on an Arrhenius function of viscosity with temperature

$$\eta = \left[ N_0 \exp\left(\frac{E}{RT}\right) \right] \quad (1)$$

where  $N_0$  is set based upon a reference viscosity  $\eta_0$  of  $2.2 \times 10^{19}$  Pa s defined at a temperature  $T$  equal to the basal temperature ( $1300^\circ\text{C}$ ). The activation energy  $E = 180$  kJ mol<sup>-1</sup> is less than experimental values ( $E = 520$  kJ mol<sup>-1</sup>, dunite [Goetze and Evans, 1979]) to simulate the effects of a stress-dependent rheology [i.e. Christensen, 1984]. In this model, I do not consider the effects of retained melt fraction [Hirth and Kohlstedt, 1995b; Hirth and Kohlstedt, 1995a] or water content [Hirth and Kohlstedt, 1996] on the viscosity of the mantle. Retained melt is predicted to decrease the mantle viscosity whereas removal of water in the initial 1% or 2% of melting may cause a sharp increase in viscosity, but the balance between these effects is not well known. The current assumptions are designed to be simple, but to still address the first-order behavior of ridge jump initiation.

To approximate faulting behavior, I simulate Coulomb-Navier plasticity through an additional viscosity law that depends upon the strain history as well as the stress. Plastic yielding occurs when the difference between the maximum  $\sigma_1$  and minimum  $\sigma_3$  principal stresses is greater than the yield stress,

$$(\sigma_1 - \sigma_3) > \sigma_{ys} \quad (2)$$

where the yield stress is defined by

$$\sigma_{ys} = (2\sigma_{coh}(\varepsilon_p) \pm \gamma(\sigma_1 + \sigma_3)) \left( \frac{1}{\sqrt{\mu^2 + 1}} \right), \quad (3)$$

where  $\gamma$  is the coefficient of static friction, and  $\sigma_{coh}$  is the cohesion, which is a function of  $\varepsilon_p$ , the accumulated plastic strain. The criteria in equation (2) is implemented numerically by adjusting the viscosity of elements where  $(\sigma_1 - \sigma_3) > \sigma_{ys}$  to

$$\eta = \eta_0 \frac{\sigma_{ys}}{\eta_{old}(\dot{\varepsilon}_1 - \dot{\varepsilon}_3)}, \quad (4)$$

where  $\eta_{old}$  is the viscosity from the previous time step and  $\dot{\varepsilon}_1$  and  $\dot{\varepsilon}_3$  are the maximum and minimum principal strain rates, respectively. This method is similar to that used by *Chen and Morgan* [1990], with the important difference that the cohesion  $\sigma_{coh}$  weakens with plastic strain  $\varepsilon_p$ , a feature that leads to more localized deformation at plate boundaries. The weakening law I have adopted is

$$\sigma_{coh} = \sigma_{coh}^{old} \left( 1 - \frac{\varepsilon_p}{\varepsilon_{crit}} \right), \quad (5)$$

where  $\varepsilon_{crit}$  is a parameter that controls the rate of strain weakening [*Poliakov and Buck*, 1998]. As  $\varepsilon_p$  is a material property, I track its advection using passive tracer particles [*Bianco et al.*, 2006; *Bianco et al.*, 2007]. This method forms regions of plate rifting across ~10-20 elements with faster spreading rates leading to more focused deformation. Thus, the model resolution of ~1.5 km in the region of plume-ridge interaction allows for spreading to be accommodated over widths of 15-30 km for spreading rates between 10-30 km/Myr.

### 2.3 Mantle Melting

I use a simple description of decompression melting of a dry, peridotite mantle to calculate productivity  $dF/dP$  where  $F$  is the melt fraction and  $P$  is pressure. The melting region is described by the peridotite solidus  $T_{solidus}$  of *Katz et al.* [2003] (their Figure 1). For pressures  $P$  and temperatures  $T$  which surpass  $T_{solidus}$ , a constant  $dT/dF$  and a constant change in entropy  $\Delta S$  associated with converting a solid to a liquid are used to calculate  $dF/dP$  [e.g. *Katz et al.*, 2003; *Asimow et al.*, 2004; *Ito and Mahoney*, 2005]

$$-\frac{dF}{dP} = \frac{\left(\frac{\partial T}{\partial P}\right)_F - \frac{\alpha T}{\rho c_p}}{\left(\frac{\partial T}{\partial F}\right)_P + \frac{T\Delta S}{c_p}}, \quad (6)$$

where  $\alpha$  is the coefficient of thermal expansivity,  $c_p$  is the heat capacity at constant pressure, and  $\rho$  is the mantle density. The value of  $dT/dF$  and  $\Delta S$  are chosen (list of symbols, page xi) so that the model predicts a normal ridge crustal thickness of 6-7 km in the absence of a mantle plume. I limit  $F$  to  $\sim 0.2$  to simulate the strong reduction in  $dF/dP$  when cpx is completely melted [*Asimow et al.*, 1997; *Katz et al.*, 2003; *Asimow et al.*, 2004; *Ito and Mahoney*, 2005]. This parameterization of mantle melting is very simple; the only variations of  $F$  with depth are associated with the slope of the solidus. However, more realism is not necessary because what is most essential to this study is modeling self-consistent changes in total melt flux reaching the solidus at the base of the lithosphere in response to changes in the temperature and flow field of the mantle.

## 2.4 Melt Transport and Penetration of the Lithosphere

The melt transport equations used here are based on those introduced by *McKenzie* [1984] to describe the conservation of mass and momentum of a two-phase system (see Appendix C). In the melting zone and along the solidus I assume that the shear and effective bulk viscosities of the matrix are too low for pressure gradients associated with solid shear or compaction to influence melt flow. As a result of these assumptions, pressure gradients associated with melt buoyancy cause melt to rise vertically in the melting zone and to flow laterally along the solidus.

At the top of the melting region (i.e. the solidus), where  $T \leq T_{solidus}$ , freezing melt makes a boundary that is impermeable to flow. It is the transport of melt accumulating just below this boundary that is essential to the model results. Here, lateral melt flow is controlled by the porosity (volume fraction of melt) in the layer below the boundary  $\phi$  while melt flux across the boundary (through the lithosphere) is controlled by the characteristic porosity of the lithosphere  $\Phi$ . The time-dependent melt transport along and across the solidus is described by (Appendix C)

$$\frac{\partial \rho_m \phi}{\partial t} + \rho_m \left( \frac{\partial u}{\partial x'} + \frac{\partial w}{\partial z'} \right) = 0 \quad (7)$$

$$u = \frac{-k_0 \phi^n}{\mu_m} (\rho_s - \rho_m) g \left[ \sin(\theta) + \Delta z \frac{\partial \phi}{\partial x'} \right] \quad (8)$$

$$w_{mantle} = - \int_{z_{max}}^{z_{solidus}} \left( \frac{dF}{dP} \right) \rho_s g u_z^s dz \quad (9)$$

$$w_{lith} = \frac{-k_0 \Phi^n}{\mu_m} (\rho_s - \rho_m) g \cos(\theta) \quad (10)$$

where  $u$  is the Darcy melt flux (Darcy flow rate times porosity) parallel to the solidus,  $w$  is the melt flux perpendicular to the solidus,  $u_z^s$  is the vertical velocity of the matrix,  $\rho$  is the density (subscripts refer to the melt  $m$ , and the solid  $s$ ),  $n$  is the exponent relating porosity to permeability ( $n = 2$ , corresponding to a solid with interconnected circular tubes [Turcotte and Schubert, 2002]) and other variables can be found in Table C1 (Appendix C). Primes denote the solidus parallel  $x'$  and perpendicular  $z'$  coordinates of the reference frame of the above equations (Figure 2). Equation (7) describes conservation of mass while equation (8) describes Darcy flow (conservation of momentum) of the melt in the direction parallel to the solidus  $x'$ . Since melt transport is 1D along the solidus, equation (9) and (10) define the melt supply from below  $w_{mantle}$  separately from the melt flux penetrating the lithosphere  $w_{lith}$ . I also approximate the gradient in melt flux in the direction perpendicular to the solidus  $z'$  as  $(w_{lith} - w_{mantle})/\delta$ , where  $\delta$  is constant (1 km). Vertical melt flow in the mantle melting zone,  $w_{mantle}$  is equal to the depth-integrated melting rate in the mantle (Equation (9)). These equations can be combined into a single dimensionless equation by using the following scaling factors (where, here, primes denote non-dimensional values and the primes denoting the solidus parallel and solidus perpendicular directions, which in detail deviate from the absolute coordinates, are dropped),

$$\begin{aligned} \phi &= \phi_0 \phi' & x &= \delta x' & t &= \tau t' & k &= k_0 \phi'^n & \tau &= \delta^2 / \kappa_0 \\ w_{mantle} &= w_{m0} w'_{mantle} & w_{m0} &= \frac{\delta \phi_0}{\tau} & u &= u_0 \phi'^{n-1} & u_0 &= \frac{\Delta \rho g}{\mu_m} k_0 n \phi_0^{n-1} \end{aligned}$$

$$\kappa_0 = \Delta z \frac{\Delta \rho g}{\mu_m} k_0 \phi_0^n \quad w_{lith} = w_{l0} w'_{lith} \quad w_{l0} = \frac{\Delta \rho g}{\mu_m} k_0 \left( \frac{\Phi_{\max}}{2} \right)^n.$$

See Appendix C or page ix for the definition of all parameters. After substituting the above factors and dropping primes, one obtains the following dimensionless equation for the porosity along the top of the melting zone,

$$\frac{\partial \phi}{\partial t} - Pe \left[ \phi^{n-1} \sin(\theta) \frac{\partial \phi}{\partial x} - \frac{\phi^n}{n} \cos(\theta) \frac{\partial \theta}{\partial x} \right] - \frac{\partial}{\partial x} \left[ \phi^n \frac{\partial \phi}{\partial x} \right] = w_{mantle} - \frac{w_{l0}}{w_{m0}} w_{lith}. \quad (11)$$

Equation (11) describes the time-dependent transport of average porosity along the solidus, just beneath the lithosphere. The porosity is controlled by two independent variables, the Peclét number  $Pe$ , and the ratio of the lithospheric melt flux scale and the scale factor of melt supply from the mantle  $w_{l0}/w_{m0}$ .

The other essential aspect of the magma transport model is to simulate when and where magma actually penetrates the lithosphere (i.e. where and when  $w_{lith} > 0$ ). The following is meant to approximate a temporal and spatial average of magma flux through the lithosphere that could include porous flow, interconnected melt channels, and diking. Based on equation (10), the vertical flux scale  $w_{l0}$  is sensitive to the effective lithospheric porosity  $\Phi$ . Following a similar methodology to *Hieronymus and Bercovici* [2001], I assume that a small change in  $\Phi$  is attributed to small changes in the excess pressure of the magma just below the plate  $\sigma_p$  and lithospheric damage (generally to include chemical, thermal, and physical damage) caused by magma passing through the plate (see Appendix C)

$$\Phi = \frac{\Phi_{\max}}{2} \left( 1 + \tanh \left( \frac{\sigma_p - \sigma_c + B_0 H_r}{2C_0 / \Phi_{\max}} \right) \right) \quad (12)$$

where  $\sigma_c$  is the inherent (constant) strength of the lithosphere represented by the cohesion and  $H_r$  is the “reduced” integrated melt flux, a measure of the accumulated magmatic damage (described below). The other variables are defined in Appendix C.

Combining equations (10) and (12) and using the scaling factors in Appendix C, the non-dimensional vertical melt flux is

$$w_{lith} = \cos(\theta) \left[ 1 + \tanh\left(\frac{\phi \cos(\theta) - \phi_{coh} + L_0 H}{D}\right) \right]^n. \quad (13)$$

This equation describes the vertical melt flux across the solidus as a balance between the dimensionless porosity along the solidus  $\phi$  (a measure of the melt pressure), the dimensionless porosity required to overcome the strength of the lithosphere  $\phi_{coh}$ , the scale factor  $D$ , and the sensitivity to magmatic damage  $L_0$  where  $L_0 H$  which is a measure of lithospheric damage associated with magma. The total damage is not permitted to exceed the strength of the lithosphere (i.e.  $L_0 H \leq \phi_{coh}$ ). In practice, this limit is rarely reached for the chosen value of  $L_0$ .

The effect of lithospheric erosion (damage) is assumed to be due to recent volcanism that causes increases in lithospheric porosity through thermal, chemical, or physical mechanisms and is assumed to be proportional to a fraction of the total time-integrated melt flux through a given piece of lithosphere. This “reduced” time-integrated melt flux  $H_r$  is calculated using the following dimensional advection equation

$$H_r = H_r^{old} + dt \left( w_{lith} w_{l0} - \frac{\partial(u_{rate} H_r^{old})}{\partial x} - healing\ rate \right) \quad (14)$$

where  $u_{rate}$  is the velocity of the overlying plate. To define a healing rate (reduction of damage), I assume that a continuously active magma conduit has a width  $w$  that is

proportional to the time-integrated melt flux. If  $w$  describes the length scale for thermal diffusion in the magma conduit

$$\frac{\partial T}{\partial t} = \kappa \frac{\partial^2 T}{\partial x^2} \propto \frac{\Delta T}{w^2},$$

( $\kappa$  is the thermal diffusivity) and if the healing rate is proportional to  $dT/dt$ , I can assume a healing rate proportional to the square of the “reduced”, time-integrated magma flux

$$healing\ rate = \frac{S}{(H_r + H_0)^2} \quad (15)$$

where  $S$  is a parameter controlling the healing rate and  $S/H_0^2$  defines the maximum healing rate in undamaged lithosphere. The form of the healing rate is valid for a system where no damage occurs below a minimum magma flux and where the healing rate decreases with increasing damage.

Although similar to the methodology of previous authors [*Spiegelman and McKenzie, 1987; Sparks and Parmentier, 1991; Sparks and Parmentier, 1994; Magde and Sparks, 1997*], the model used here is slightly more complex in that it accounts for mass and momentum conservation along the solidus as well as off-axis melt flux through the lithosphere. The melt flux across the solidus predicted by the above system of equations represents the magma penetrating and heating the lithosphere and is used to calculate the heating rate in the models (see section 2.5).

In summary, the following procedure is used to calculate melt migration at each time-step. First the location and slope of the solidus are determined. Next, the melt supply from below  $w_{mantle}$  is calculated by depth integrating the melting rate. The value of  $w_{lith}$  at each point along the solidus is found using Equation (13) with the damage

values from the previous time-step. Equation (11) is then solved for the transport of melt along the solidus. Finally, the damage variable  $H_r$  is updated using Equation (14).

### 2.5 Magmatic Heating

In a similar formulation to *Mittelstaedt et al.* [2008], the heating rate at each point in the lithosphere is defined as,

$$q = \rho c_p \beta w_{lith} w_{l0} (T_{asth} - T(x, z, t)), \quad (16)$$

where  $T_{asth}$  is the temperature of both the non-plume asthenosphere and the penetrating magma (1300°C),  $\beta$  is a constant scale factor controlling the heating rate, and  $w_{lith}$  is the magma flux through the lithosphere. The above equation for magmatic heating is designed to be as general as possible and to not require a specific melt transport mechanism in the lithosphere. For a discussion of the style of melt transport and the geologic implications represented by equation (16), see *Mittelstaedt et al.* [2008].

I examine two types of cases in this manuscript. First, cases of Type 1 have constant values of both  $\beta$  and  $w_{lith}$  ( $\beta w_{lith}$  values range from 9e-14 to 10e-13) multiplied by a Gaussian distribution (half-width = 6 km). Cases of Type 2 use the time-varying value of  $w_{lith}$  calculated by the melt transport equations in section 2.4 and the value of  $\beta$  is constant ( $\beta$  is varied between 9e-6 and 10e-5). For both types, I examine half spreading rates of 10, 20, and 30 km/Myr, plate ages of between 3 and 15 Myr, and, for a few cases, the variation in plume temperature and buoyancy flux. Additionally, I consider some cases of Type 2 where the plume and ridge migrate relative to each other.

### 3. Results

#### 3.1 Controlling Parameters of Melt Transport

Three of the main parameters controlling the transport of melt and the localization of melt flux through the lithosphere are  $Pe$ ,  $L_0$ , and  $S$  (Figure 3). I use three simple examples to illustrate the effect of these parameters. First, I examine the effect of  $Pe$  on the steady-state porosity beneath a “ridge-axis”-like solidus that slopes down from a peak located at  $x' = 30$  (Figure 3A). The melt supply from below is distributed in a Gaussian manner centered at  $x' = 30$ ,  $L_0$  is 0 (melt escapes from the ridge center, but no damage is accumulated), and the porosity is set to 0 on the left and right sides of the domain. The flow of melt along the solidus is largely controlled by the size of  $Pe$ . Smaller values of  $Pe$  will tend to reduce porosity variations along the solidus whereas larger values of  $Pe$  will lead to higher porosities (melt accumulation) at local peaks in solidus height (Figure 3A).

The second case discussed here (Figure 3B) demonstrates the effect of the healing rate scale  $S$  on the focusing of magma flux through the lithosphere. Roughly similar to a hotspot beneath sloping off-axis lithosphere, the melt supply from below is distributed in a Gaussian manner centered at  $x' = 50$ , the solidus slopes down to the right at a constant angle ( $10^\circ$ ) (Figure 3B). Accumulated lithospheric damage  $H_r$  is advected to the right at a constant velocity (10 km/Myr) with the plate, porosity is set to 0 on the right edge (cases shown at dimensional time  $t = 1$  Myr) and melt allowed to flow out of the left edge. The healing rate scale  $S$  sets both the maximum ( $S/H_0^2$ ) and minimum value of the healing rate (Equation 15) over a given range of accumulated magmatic damage. Larger values of  $S$  lead to more focused zones of initial damage

accumulation and lower values of the maximum magma flux through the lithosphere (Figure 3B).

Finally, the third case discussed here demonstrates how the sensitivity to damage  $L_0$  affects the width and location of magma flux through the lithosphere. Resembling the models of plume-ridge interaction discussed later, the solidus depth increases with the square of the distance from a “ridge axis” which is centered at  $x' = 30$ ; the melt flux from below is equal to the sum of two Gaussians with peaks at  $x' = 30$  and at  $x' = 60$  (the “ridge” and “plume” melt supplies), and porosity is 0 on the left and right hand edges (Figure 3C). Once damage begins to accumulate, larger values of  $L_0$  lead to greater magma fluxes for the same value of  $\phi$ . The greater magma flux causes more damage to accumulate and reduces the healing rate, which together cause a positive feedback that focuses the magma flux to narrow peaks (Figure 3C). This focusing is important because it restricts regions of magma flux through the lithosphere to geologically reasonable distances (e.g. compared to the width of a hotspot volcano) and is essential for the initiation of ridge jumps. The chosen values of the various parameters lead to eruptive zones at the hotspot and ridge over distances of  $\sim 10$ - $20$  km for most cases, and are kept the same for all model cases below. Further discussion of the parameters which control melt transport and focusing of magma flux through the lithosphere is given in Appendix C. Parameter values are listed in Table 1.

### *3.2 Time evolution: Fixed plume-ridge separation distance (Type 2)*

In this section, I examine the time evolution of a ridge jump for a case of Type 2 with no plume-ridge migration (Figure 4A-D). Although Type 1 and Type 2 show

similar behavior, I focus here on the more realistic case to reveal the importance of melt transport. Melt transport and lithospheric heating are initiated after the plume impacts the lithosphere and begins to spread across the box at time  $t = 0$ . Melting occurs in the mantle both beneath the ridge axis and within the plume stem, and melt begins to accumulate along the solidus. Initially, the magma flux at the ridge axis is fed from a combination of plume and ridge melting (equivalent of  $\sim 30\text{-}40$  km of crust) and focused to a region  $\sim 15$  km wide; but off-axis, above the plume, a small magma flux passes through the undamaged lithosphere over a broad region ( $\sim 150$  km) (top box, Figure X). After several hundred thousand years, the diffuse off-axis magma flux starts to focus to a smaller region ( $\sim 90$  km) in response to damage accumulation and flattening of the solidus caused by erosion of the lithosphere by the plume and magmatic heating. The continued erosion of the lithosphere and accumulation of damage eventually focus the magma flux to a width comparable to that of the ridge axis. Because the melt erupting off-axis is tapping melt produced by the plume that previously would have traveled to the ridge axis, the magma flux and magmatic heating rate at the ridge-axis are greatly reduced. The focused off-axis magma flux results in large magmatic heating rates which weaken the lithosphere until rifting is initiated. As rifting begins, warm mantle material rises into the proto-rift which further weakens the lithosphere and promotes faster rifting. During this transfer of spreading from the old to the new ridge-axis ( $\Delta t = 0.15\text{-}2.9$  Myr), the lithosphere between the rifts acts as a micro-plate with very little, to no visible velocity gradients across its surface. Finally, all spreading is accommodated at the new ridge axis and the old ridge is abandoned ( $t = 1.5\text{-}9.0$  Myr).

### 3.3 Scaling: Ridge Jumps with Imposed Magma Flux Through the Lithosphere (Type 1)

I first examine scaling relationships for cases of Type 1 (upwelling plume with imposed lithospheric heating off-axis) to reveal the important effects of lithospheric heating and to relate these results to previous work of myself and colleagues (imposed lithospheric heating without a plume) [Mittelstaedt *et al.*, 2008]. As in our previous work, we use two parameters to evaluate the minimum heating rate required to initiate a ridge jump for cases of Type 1. First, the total integrated off-axis heating rate above that at the ridge-axis at time  $t = 0$ ,

$$(Q_{hotspot} - Q_{ridge}) = \int_0^{\infty} \int_{-w/2}^{w/2} ((q)_{t=0} - Q_{ridge}) dx dz \quad (17)$$

where  $w$  is the width of the heating zone (12 km),  $q$  is the heating rate from equation (16), and  $Q_{ridge}$  is the total integrated ridge-axis heating rate. Mittelstaedt *et al.* [2008] found that the important variable to initiating ridge jumps is the total integrated heating rate ( $Q_{hotspot}$ ) above that at the ridge axis ( $Q_{ridge}$ ), thus we set  $Q_{ridge}$  to 0 here for simplicity.  $Q_{hotspot}$  represents the maximum heating rate of the model, when the temperature contrast between the magma and the lithosphere is greatest. The second parameter is a measure of the heating rate required to thermally remove the lithosphere,

$$Q_{thin} = \rho c_p u_{plate} \left[ \int_0^{z_{lith}} (T_{asth} - T(z)) dz \right]_{t=0} \quad (18)$$

where  $z_{lith}$  is the initial thickness of the lithosphere.  $Q_{thin}$  incorporates the effect of spreading rate and plate age on the magnitude of the heating rate required to achieve a ridge jump.

Similar to our prior results [Mittelstaedt *et al.*, 2008], for a given value of  $Q_{thin}$  there is a minimum value of  $Q_{hotspot}$  necessary to initiate a ridge jump (Figure 5) and this

value increases non-linearly with increasing  $Q_{thin}$  approximately according to the following least squares fit

$$Q_{hotspot} = a(Q_{thin})^b + c \quad (19)$$

where  $a = 2088.00 \text{ J}^{-(b-1)} \text{ m}^{(b-1)} \text{ s}^{(b-1)}$ ,  $b = 0.47$ , and  $c = -1.95\text{e}5 \text{ J m}^{-1} \text{ s}^{-1}$ . For an increase in the spreading rate or the lithospheric age (larger  $Q_{thin}$ ), a greater heating rate ( $Q_{hotspot}$ ) is required to initiate a ridge jump.

Although the minimum values of  $Q_{hotspot}$  required to jump in the current model are larger than those found by *Mittelstaedt et al* [2008] for small values of  $Q_{thin}$ , the two models overlap at the largest  $Q_{thin}$  values examined in that manuscript (Figure 5). This consistency is encouraging given that this work and the previous work differ in terms of the numerical method, the rheology simulated, and the inclusion of a hot, upwelling plume.

The time between when magmatic heating begins at time  $t = 0$  and when the ridge jumps  $t_{jump}$  (defined as the time when 80% of the full spreading rate is accommodated at the new ridge axis) increases with increasing spreading rate (advection of lithospheric material through the heating zone) and lithospheric thickness, but decreases with increasing rates of magmatic heating. Results indicate that these behavior are captured approximately by a power-law relationship

$$\frac{t_{jump}}{t_{age}} = j \left( \frac{u_{rate}}{(\beta w_{lith} w_{l0})_{fixed} \sqrt{t_{age}}} \right)^m + l \quad (20)$$

where  $j = 6.37 \text{ m}^{-m} \text{ s}^{m/2}$ ,  $m = 0.29$ , and  $l = 0.277$  (Figure 5). This approximate relationship reveals many of the processes important to magmatic heating. For example, larger values of  $\beta w_{lith}$  will more rapidly thin the lithosphere and thus decrease

the time to a jump. In contrast, for a given spreading rate and  $\beta w_{lith}$ , an older plate with thicker lithosphere requires longer to heat and thus a larger  $t_{jump}$ . The approximate fit of Equation (20) also shows that at a given  $t_{age}$ ,  $t_{jump}$  increases with spreading rate. This increase is consistent with *Mittelstaedt et al.* [2008] who, simulating heating without a plume, also found  $t_{jump}$  for a given  $t_{age}$  to increase with spreading rate, suggesting that the inclusion of a hot, upwelling plume does not significantly alter the processes that control ridge jump initiation in these models.

### 3.4 Scaling: Fixed plume-ridge separation distance and computed magma flux (Type 2)

In cases of Type 1 (section 3.3), the width of the imposed heating zone is used to calculate the value of  $Q_{hotspot}$ . Measured at time  $t = 0$ , when the temperature contrast between magma and the lithosphere is greatest,  $Q_{hotspot}$  represents the maximum heating rate of the system. Analogously, for cases of Type 2, the maximum magma flux through the off-axis lithosphere  $w_{lith}^{max}$  multiplied by the heating rate scale factor  $\beta$  is a measure of the maximum heating rate of the lithosphere. Similar to cases of Type 1, I find that for a given value of  $Q_{thin}$  there is a minimum value of  $\beta w_{lith}^{max}$  to initiate a ridge jump and this value increases non-linearly with  $Q_{thin}$  (Figure 6A). This indicates that the maximum heating rate necessary to initiate a ridge jump increases with spreading rate and plate age. The model results predict that ridge jumps will occur for a given value of  $Q_{thin}$  when the heating parameter  $\beta w_{lith}^{max} w_{l0}$  meets the following condition

$$\beta w_{lith}^{max} w_{l0} \geq a(Q_{thin} - d)^b + c \quad (21)$$

where least squares regression yields  $a = 2.96e-14 \text{ J}^b \text{ m}^b \text{ s}^{(b-1)}$ ,  $b = 0.2$ ,  $c = -8e-14 \text{ s}^{-1}$ , and  $d = 2.9e4 \text{ J m}^{-1} \text{ s}^{-1}$ . Although this relationship is a good approximation to the

boundary between cases that jump and those that do not, it is difficult to relate to observations as the definition of  $Q_{thin}$  does not have a straightforward relationship with commonly observed values such as seafloor age. A nearly equivalent value to  $Q_{thin}$  is the spreading rate multiplied by the time-integrated surface heat loss of a mantle half-space

$$Q_{cool} = \int_0^{t_{age}} \frac{u_{rate} \rho c_p (T_{asth}) \sqrt{\kappa \pi}}{\sqrt{t}} dt = \frac{2u_{rate} \rho c_p \Delta T}{\sqrt{\pi}} \sqrt{\kappa t_{age}} \quad (22)$$

where the seafloor temperature is assumed to be 0°C. For young plate ages, this value is identical to  $Q_{thin}$ , but at larger plate ages there is a greater discrepancy between the plate-cooling initial condition (used to calculate  $Q_{thin}$ ) and a cooling mantle half-space. Despite this discrepancy, the scaling relationship in equation (21), with  $Q_{cool}$  substituted for  $Q_{thin}$ ,

$$\beta w_{lith}^{max} w_{l0} \geq a(Q_{cool} - d)^b + c \quad (23)$$

( $a = 2.96e-14 \text{ J}^{-b} \text{ m}^b \text{ s}^{(b-1)}$ ,  $b = 0.2$ ,  $c = -8e-14 \text{ s}^{-1}$ , and  $d = 2.9e4 \text{ J m}^{-1} \text{ s}^{-1}$ ) displays a good fit to the results and predicts similar minimum values of  $\beta w_{lith}^{max} w_{l0}$  to initiate a ridge jump as equation (21) (Figure 6B). Equation (23) is used in section (4.1) to relate the model predictions to observations of ridge jumps.

Results from cases of Type 2 show that the value of  $t_{jump}$  scaled by  $t_{age}$  where rifting first occurs (a slightly different definition of  $t_{age}$  than for Type 1), is a function of the maximum heating rate, the thickness of the lithosphere ( $\sim \sqrt{t_{age}}$ ), and the slope of the lithosphere (Figure 6C)

$$\frac{\beta w_{lith}^{max} w_{l0} \sqrt{t_{age}}}{\partial z_{lith} / \partial x} = \frac{\beta w_{lith}^{max} w_{l0} \Delta x}{(f/2)(\kappa)^{1/2}} \quad (24)$$

where  $f$  is the scale factor controlling the estimate of the thickness of the lithosphere (taken to be 1 for simplicity),  $\Delta x$  is the off-axis distance corresponding to  $t_{age}$ , and  $z_{lith} = f \sqrt{\kappa t_{age}} \approx \sqrt{\kappa \Delta x / u_{plate}}$  is the thickness of a cooling mantle half-space. The relationship between equation (24) and the scaled value of  $t_{jump}$  is found by a least squares fit to be approximately

$$\frac{t_{jump}}{t_{age}} = j \left( \frac{\beta w_{lith}^{max} w_{l0} \Delta x}{(\kappa)^{1/2}} \right)^{-m} + l \quad (25)$$

where  $j = 8.42e-5 \text{ s}^{-m/2}$ ,  $m = 1.17$ , and  $l = 0.291$ . This relationship reveals the importance of several, sometimes competing, processes. For example, the scaled time to a jump will decrease for a larger value of  $\beta w_{lith}^{max}$  because the lithosphere will be heated more rapidly. Alternatively, a smaller value of  $\Delta x$  predicts a larger value of  $t_{jump}/t_{age}$  because more melt is transported to the ridge and not through the off-axis lithosphere.

To isolate the effect of spreading rate on  $t_{jump}$ , equation (25) is re-written using  $\Delta x = t_{age} u_{rate}$

$$\frac{t_{jump}}{t_{age}} = j \left( \frac{\beta w_{lith}^{max} w_{l0} t_{age} u_{rate}}{(\kappa)^{1/2}} \right)^{-m} + l \quad (26)$$

Holding  $t_{age}$  fixed, equation (26) reveals that an increase in spreading rate causes a decrease in  $t_{jump}$ . As spreading rate increases, the slope of the lithosphere decreases causing the ridge-ward flow of melt to decrease, and thus the magma flux through the lithosphere to increase (decreasing  $t_{jump}$ ).

The different scaling relationships found for cases of Type 1, Type 2, and the previous work of *Mittelstaedt et al.* [2008], reveal both similarities and differences

between the parameters that control ridge jump initiation in each case. For example, all of the above types of cases predict a decrease in the time to jump for a larger value of the heating rate because the lithosphere thins more rapidly. In cases of Type 2,  $t_{jump}$  displays an inverse relationship to spreading rate, whereas  $t_{jump}$  in cases of Type 1 and the results of *Mittelstaedt et al.* [2008] is proportional to spreading rate. This difference highlights the effect of melt transport on cases of Type 2. At a given lithospheric age, the slope of the lithosphere (at a given age) decreases and, for cases of Type 2, less melt is transported upslope to the ridge axis. This decrease in ridge-ward melt flow results in a decreased magma flux at the ridge and an increased off-axis magma flux, decreasing the time to jump. In contrast, in cases of Type 1 and in *Mittelstaedt et al.* [2008], the heating rate at the ridge axis and off-axis are fixed, therefore, increasing spreading rates cause a decrease in the time to jump because material passes more rapidly through the heating zone (causing weakening to occur over a broader region) and the weaker ridge axis requires greater off-axis lithospheric thinning to initiate rifting. These results suggest that melt transport is an important mechanism for the initiation of ridge jumps.

### 3.5 Migrating Ridge Jumps (Type 2)

Figure 4E-H displays the time evolution for a case of Type 2 ( $u_{plate} = 10$  km/Myr,  $\beta = 3.0e-5$ ) where I simulate relative motion between the plume and ridge by moving the location of the imposed plume temperature anomaly relative to the model boundaries at a constant rate (here, 10 km/Myr). To allow longer the plume to migrate longer, the model domain for these cases is 2000 km wide with a uniform element width of  $\sim 2$  km (1024 elements). Other model conditions are unchanged. The plume is

initially positioned beneath the ridge axis and is allowed to rise through the mantle until it reaches the lithosphere and begins to spread laterally. Time  $t = 0$  is defined when melt transport, magmatic heating, and plume migration are activated.

Initially, all of the melt produced travels to the ridge-axis and there is no magmatic heating off-axis. After the plume migrates a distance of  $\sim 50$  km ( $t = 5$  Myr), an off-axis region of magma flux develops at a distance of  $\sim 30$ - $50$  km from the ridge heating zone. As the plume continues to migrate, the off-axis magma flux focuses to a small region, magmatic heating weakens the lithosphere, and rifting pulls up warm mantle, which further weakens the lithosphere until a new ridge axis is formed. The time between  $t=0$  and the ridge jump takes significantly longer to complete ( $\sim 27$  Myr) than for non-migrating cases with the same values of the other parameters.

In some cases, the models successfully predict repeated ridge jumps. As in the case shown in Figure 4, after the initial ridge jump is complete, the majority of melt from the plume travels toward the ridge axis due to the steep slope between the old lithosphere currently above the plume and the new ridge axis. The magma flux is offset just plume-ward of the center of divergence of the new ridge (where the solidus begins to flatten). This offset tends to make the ridge migrate with the plume, but at a slightly slower rate than the migration of the plume itself. The plume essentially “captures” the ridge for a short time. After the plume moves sufficiently far from the ridge, off-axis magma flux occurs over a much broader area than prior to the first jump into the initially undamaged lithosphere, but heating thins the lithosphere causing the solidus to bend upward and directing more melt to the new off-axis location (Figure XG). The process continues until the ridge jumps a second time ( $t = 50$  Myr) (Figure XH).

The pattern of ridge jumps in Figure 7 depends on the spreading rate  $u_{rate}$ , the plume migration velocity  $u_{mig}$ , and the value of  $\beta$ . Cases (a) and (b) do not thin the lithosphere off-axis sufficiently to initiate ridge jumps and the plume and ridge separate at the migration velocity. In case (c) the same spreading rate and value of  $\beta$  are used as in case (a), but a smaller value of  $u_{mig}$  (20 km/Myr instead of 30 km/Myr), equal to the half-spreading rate, leads to a set of “dueling” rifts where each rift accommodates a fraction of the total spreading rate that varies through time. The reduction of  $u_{mig}$  towards  $u_{rate}$  increases the time available to heat the off-axis lithosphere allowing rifting to initiate off-axis. In case (d),  $u_{mig}$  is equal to  $u_{rate}$ , as in case (c), but their smaller magnitudes and different value of  $\beta$  result in repeat ridge jumps instead of dueling ridges. In case (e)  $u_{mig}$  is increase so that it is 5 km/Myr larger than  $u_{rate}$ . This case predicts a single jump followed by the plume “capturing” the ridge axis. The increase in migration velocity relative to case (d) decreases the time to heat lithosphere off-axis, but the slow overall rate allows a sufficient time to heat and weaken the ridge axis, causing it to move with the plume. The above results suggest that off-axis rifting, and thus a repeat ridge jump, requires a sufficient value of  $\beta$  to thin the lithosphere and is promoted by a small difference between  $u_{rate}$  and  $u_{mig}$ , which maximizes the time available to heat a given piece of lithosphere.

### *3.6 Variations in Plume Temperature and Buoyancy Flux*

Figure 8 displays the effect of separately varying the plume excess temperature  $\Delta T_p$  and the width of the plume (buoyancy flux  $B$  is shown for ease of comparison to other work) on the value of  $t_{jump}$  for both a case of Type 1 and one of Type 2. The Type

1 case has a half-spreading rate of 10 km/Myr with a plume-ridge separation distance of 100 km,  $\beta w_{lith} = 1.5e-13 \text{ s}^{-1}$ , and a zone of heating of width 12 km. The Type 2 case has a half-spreading rate of 20 km/Myr, a plume-ridge separation distance of 200 km (giving ridge jumps  $\sim 150$  km from the ridge),  $\beta = 6.5e-5 \text{ m}^{-1}$ ,  $\beta w_{lith}^{max} = 2e-13 \text{ s}^{-1}$ , and a width of off-axis magmatic heating that varies in time from 15 km to 100 km.

Changes in  $\Delta T_p$  and  $B$  in cases of Type 1 do not change the magmatic heating rate of the lithosphere and thus isolate the thermal and mechanical effects of an upwelling plume. The value of  $t_{jump}$  increases with increasing  $\Delta T_p$  (Figure XA), but decreases with increasing  $B$  (Figure XC). Although as  $\Delta T_p$  is increased the value of  $B$  is also increased, the principle control on  $t_{jump}$  when  $\Delta T_p$  is increased is the weakening of the ridge-axis caused by the warmer underlying mantle. When  $B$  is increased without changes in  $\Delta T_p$  (larger volume flux), the decrease in  $t_{jump}$  is promoted by changes to the lithospheric stress field associated with shear between the spreading plume material and the overlying plate.

For cases of Type 2, changes to  $\Delta T_p$  and  $B$  cause changes not only in mantle temperature and the stress field, but they also change the magmatic heating rate due to changes in the melt supply delivered by the plume. Unlike the cases of Type 1, increases in  $\Delta T_p$  and  $B$  for Type 2 both lead to decreases in  $t_{jump}$  (Figure XB and XD). For a small increase in  $\Delta T_p$  ( $50^\circ\text{C}$ ), there is a large decrease in  $t_{jump}$  ( $\sim 3\text{Myr}$ ) due to a larger magma flux through the lithosphere associated with greater plume melting. In fact, for the case shown in Figure 8, values of  $\Delta T_p \leq 250^\circ\text{C}$  do not result in a ridge jump. Decreases in  $t_{jump}$  associated with larger values of  $B$  are similar to those of Type

1 over the same range of  $B$ , but also have the added contribution of a higher melt flux from the plume.

## 4. Discussion

### 4.1 Mid-Ocean Ridge Jumps: Predicted Trends and Observations

Mid-ocean ridge jumps associated with plume-ridge interaction are observed near current and former locations of many hotspots including Iceland [Jóhannesson, 1980; Hardarson *et al.*, 1997], the Galapagos [Wilson and Hey, 1995], Ascension [Brozena and White, 1990], Shona [Small, 1995], Shatsky Rise [Nakanishi *et al.*, 1999], Louisville [Small, 1995; Geli *et al.*, 1998], and along the Ninety East Ridge [Krishna *et al.*, 1995; Krishna and Rao, 2000; Desa *et al.*, 2006]. In the following discussion, I relate the model predictions to three characteristics of the jumps at the above locations including half-spreading rate, seafloor age where jumps occurred, and the length of time from the initiation of volcanism to the completion of a ridge jump ( $\sim t_{jump}$ ). Values for half-spreading rate  $u_{rate}$  and seafloor age  $t_{age}$  are available or are estimated from published magnetic isochron data for all of the above locations (except Kolbeinsey, see below). Iceland is the only location for which  $t_{jump}$  is well constrained by age dating of lavas (see Figure 9 for references). I first discuss the initiation of ridge jumps relative to seafloor age and spreading rate (Figure 6A and 6B) and then discuss the relationship between time to jump and spreading rate (Equation 26).

Figure 9 shows the relationship between observed values of  $u_{rate}$  at the time of a ridge jump and  $t_{age}$  for 14 ridge jumps associated with plume-ridge interaction. Also

shown are a set of theoretical curves based on the model results (Equation 23) of the maximum  $t_{age}$  and  $u_{rate}$  to initiate a ridge jump (jumps are predicted to occur below the curves) at a given value of  $\beta w_{lith}^{max}$ . Values of spreading rate and plate age are from the references in Figure 9 or are estimated using published magnetic anomalies with error bars based on anomaly width. Error bars for published values are plotted when given. For the special case of the jump from the extinct Aegir Ridge into continental lithosphere to form the Kolbeinsey ridge (Kol, Figure 9), the value of  $t_{age}$  is taken as the equivalent age of oceanic lithosphere with the same elastic thickness [Burov and Diament, 1995] estimated to be equal to the depth of the lithosphere-asthenosphere boundary for Greenland just prior to rifting [Mjelde *et al.*, 2008]. The theoretical curves predict ridge jumps to be restricted to younger plate ages (for a given value of  $\beta w_{lith}^{max}$ ) for a larger value of spreading rate. For a given spreading rate, the theoretical minimum value of  $\beta w_{lith}^{max}$  to initiate a ridge jump is smaller for younger plate ages. These predictions suggest that jumps are more likely to occur to younger seafloor and that jumps to older seafloor may require large magma fluxes or very slow spreading rates. Indeed, although most of the data fall below the theoretical curves and likely represent a range of values of  $\beta w_{lith}$ , observations at the above locations show a general decrease in the observed  $t_{age}$  for larger spreading rates. The favorability of jumps in young seafloor is also reflected by 11 of the 14 jumps occurring in seafloor  $\leq 3$  Myr old. Of jumps that occur to older seafloor ( $\geq 4$ Ma), the most recent jump at Iceland (Ice, Figure 9) and the jump from the extinct Aegir ridge to the currently spreading Kolbeinsey ridge (Kol, Figure 9) both occurred in slowly moving lithosphere (half spreading rates  $\leq 10$  km/Myr). The remaining large jump along the Ninety East ridge into  $\sim 8$  Myr old

seafloor [*Krishna and Rao, 2000*] does not appear to follow the predicted trends seen here and may require an unusually large magmatic heating rate compared to other cases. Although the majority of the above observations generally agree with the trends predicted by the results, data are only available for a limited number of ridge jumps associated with plume-ridge interaction.

For a given  $t_{age}$ , model results predict the time between initiation of off-axis magmatism and the completion of a ridge jump to decrease with increasing spreading rate (Equation 26). Of the locations listed at the beginning of this section, only Iceland is the time to complete a ridge jump constrained by age dating of rift zone lavas ( $\sim 8$  Myr, [*Hardarson et al., 1997*]). However, magnetic anomaly data from the Galapagos require  $\sim 3$ -4 jumps of the Galapagos Spreading Center between  $\sim 5$ -10 Ma [*Wilson and Hey, 1995*] suggesting a maximum time to jump of  $\sim 1.6$ -2.5 Myr (assuming completion of the first jump at 10 Ma and the last at 5 Ma). This estimate of a shorter time to jump at the Galapagos and the faster half-spreading rate of the GSC ( $\sim 30$  km/Myr) compared to the Mid-Atlantic Ridge (MAR) at Iceland (10 km/Myr) are consistent with these model predictions.

#### *4.2 Repeated Ridge Jumps*

At many locations including Iceland [*Jóhannesson, 1980; Hardarson et al., 1997*], Shatsky Rise [*Nakanishi et al., 1999*], and along the Ninety East Ridge [*Krishna et al., 1995; Krishna and Rao, 2000; Desa et al., 2006*], ridge jumps often occur repeatedly as the ridge-axis migrates away from the (presumably) fixed hotspot. Alternatively, the hotspot might capture the ridge axis, such as at the Galapagos

between ~5 Ma and ~2.5 Ma where, after a series of jumps between ~5-10 Ma and a steadily increasing spreading rate, the ridge moved with the hotspot without discrete ridge jumps [Hey, 1977; Wilson and Hey, 1995]. Finally, the hotspot and ridge can separate without a jump as has occurred at the Galapagos since ~2.5 Ma [Wilson and Hey, 1995]. The mechanism which controls the timescale and distance over which repeat ridge jumps occur is not well understood.

*Mittelstaedt et al.* [2008] examined the effect of a magmatic heating zone of fixed width moving steadily across the lithosphere. As the heating zone approached a ridge-axis, for a sufficient value of  $Q_{hotspots}$ , the ridge jumped toward the heating zone and was subsequently “captured” and migrated steadily with the heating zone for a time as it continued to move across the model. The heating zone and new ridge-axis separated once the lithosphere entering the heating zone was too thick to thermally dissolve in the time it crossed the width of the heating zone. No repeat ridge jumps were observed.

What is new in the current models is the ability to successfully predict repeated ridge jumps. The dynamic evolution of magma flux through the lithosphere (and thus magmatic heating) is the primary process that leads to repeated jumps. After an initial ridge jump, a discrete shift (instead of a smooth progression) of magma flux from the recently jumped axis to a new off-axis location results in a region of magmatic weakening separate from the ridge and eventually a new ridge jump. The ability and length of time required for magma flux to shift to a new off-axis location is controlled primarily by melt transport along the slope of the solidus above the plume melting zone. Just after a jump, this slope is steep due to the age contrast between the new ridge axis

and the old lithosphere currently above the plume. Melt is transported rapidly up this slope, preventing the formation of a new off-axis heating zone. Repeat jumps in the model require flattening of this slope by plume induced thinning which is maximized when the migration rate is similar to the half-spreading rate.

Using geologic observations, the results from models with a migrating plume are compared to Iceland and the Galapagos. The models predict a jump recurrence time for a case similar to Iceland of ~25 Myr, significantly longer than the observed value of ~7-8 Myr [Jóhannesson, 1980; Hardarson *et al.*, 1997]. One possible cause for the discrepancy between Iceland and the models is the 2D geometry used here. A ridge axis may be less likely to migrate with the hotspot, delaying jumps, if the zone of magmatic heating is located across only a portion of the ridge axis, instead of along the entire ridge as implied by the 2D models used here. For a fixed heating rate parameter  $\beta$ , the models predict the plume and ridge to be more likely to separate without jumps as the relative velocity between the plume and the overlying plate increases. This trend is consistent with the steadily increasing spreading rate at the Galapagos since ~10 Ma and the current migration of the ridge without jumps (since ~2.5 Ma) [Wilson and Hey, 1995].

#### *4.3 Intra-Plate Hotspots: The Contribution of Magmatic Heating to Plate Thinning*

Magmatic heating in the model predicts appreciable amounts of lithospheric thinning above a plume, ranging from maximal thinning to cause a ridge jump, to broad regions of more subdued heating. The magnitude of the predicted thinning depends upon the heating rate  $\beta$ , the magma flux  $w_{lith}$ , and the time a given portion of the

lithosphere experiences heating. Such thinning is likely to contribute, at least locally, to elevating the hotspot swell and perhaps even to increasing the local heat flow. These predictions are consistent with observations at Hawaii where a recent investigation using receiver functions determined that the lithosphere beneath the Hawaiian volcano chain thins locally (across ~300 km) from ~100-110 km (normal 90 Myr old plate thicknesses) to ~50-60 km beneath Oahu and Kauai (~500 km down stream, ~86 km/Myr plate velocity) [Li *et al.*, 2004]. Previously suggested mechanisms for plume-induced thinning of the Hawaiian lithosphere include small scale convection and thermal “rejuvenation” [Detrick and Crough, 1978; Ribe and Christensen, 1994; Moore *et al.*, 1998; Li *et al.*, 2004]. Magmatic heating provides another, independent mechanism for lithospheric thinning above the Hawaiian plume and other intra-plate hotspots.

#### *4.4 Ridge jumps and the Location of Ridges Relative to Hotspots*

A recent study noted that hotspots not associated with the Pacific and African super-plumes are commonly clustered within ~1000 km of slow-spreading, but not fast-spreading ridges [Jellinek *et al.*, 2003]. The authors suggest that the large ratio of plate velocity to vertical plume velocity for fast-spreading ridges inhibits the formation of hotspots because plume material is pulled into the rapid ridge upwelling before a hotspot can form. The velocity ratio near slow spreading ridges, however, is smaller allowing hotspots to form more easily. Another possible reason for hotspots to be located near slow-spreading ridges, suggested by the above models, is the capture of a ridge by a mantle plume through ridge jumps and asymmetric spreading. The model

results suggest that jumps at slow spreading ridges might occur more readily because the minimum heating rate required to jump decreases with decreasing spreading rate (Equation 21). In addition, as a ridge and plume separate, under certain model conditions, the ridge is predicted to remain near the plume for long periods of time. Repeated ridge jumps over time result in asymmetric accretion as observed near many hotspots [*Muller et al.*, 1998; *Muller et al.*, 2001b] and might explain the distribution of hotspots and ridges today.

## 5. Conclusions

In this study, I explore the combined effects of plume-lithosphere interaction and magmatic heating of the lithosphere on the initiation of ridge jumps. I use a 2D model of visco-plastic mantle flow with a strain-history dependent yield criteria coupled to a simple description of melting and melt transport. I have quantified the effects of plate spreading rate, lithospheric age, plume temperature and buoyancy flux, heating rate and ridge migration rate.

A simple model of melt migration is used to predict heating of the lithosphere where magma passes through it. The melt transport equations simulate the average flow of melt in a layer of high porosity at the solidus, just beneath the lithosphere. The ability of magma to reach the seafloor depends on the characteristic porosity of the lithosphere controlled by a balance between the melt pressure at the solidus, the cohesive strength of the lithosphere, and the accumulated magmatic damage of the

lithosphere. This model results in focused regions of magmatic heating and eruptions over distances between ~10-20 km, consistent with the width of the neo-volcanic zone at many mid-ocean ridges [e.g. *Karsten et al.*, 1986] and the widths of individual volcanoes on the seafloor. In regions where magma passes through the lithosphere, the magma flux responds dynamically to changes in melt supply from below (e.g. as the plume migrates relative to the ridge axis).

Scaling of the model results shows general similarity to previous work examining the effect of magmatic heating [*Mittelstaedt et al.*, 2008]. The minimum value of the magmatic heating rate to initiate a ridge jump shows a non-linear relationship to the heating rate required to thin the lithosphere  $Q_{thin}$ . In all cases the time to a ridge jump decreases for larger values of the magmatic heating rate. The time to a jump for cases with a fixed heating zone is proportional to spreading rate, but in cases where melt migration governs magmatic heating it is inversely proportional to spreading rate. Another significant departure from cases with a fixed heating zone, is that the time to a ridge jump increases for smaller distances between the ridge and plume (at a constant lithospheric age) due to more melt being transported to the ridge and not off-axis.

The inclusion of a hot, plume-like upwelling introduces competing effects that both promote and inhibit ridge jumps as well as change the time to a jump. Larger values of the plume excess temperature result in weakening of the ridge axis making a ridge jump more difficult. However, a larger plume temperature also causes an increase in melt flux off-axis and promotes ridge jumps. Ridge jumps are also promoted by

increases in the volume flux of the plume due to both increases in melt flux and larger shear stresses on the base of the plate.

This model predicts repeat ridge jumps due to the relative motion of a plume and ridge for certain conditions. For cases with small values of the heating rate scale  $\beta$  or fast migration rates, the plume and ridge separate without a jump. Large values of  $\beta$  at intermediate migration rates result in the ridge being captured by the plume (immediately or after a single jump) and migrating across the model. Finally, intermediate values of  $\beta$ , for migration rates very close to the plate spreading rate, lead to repeat ridge jumps. Model results also suggest that magmatic heating of the lithosphere is a potential mechanism for lithospheric thinning above intra-plate hotspots such as Hawaii. Finally, the process of repeat ridge jumps and ridge capture might explain the observation that the majority of hotspots are located near ridges.

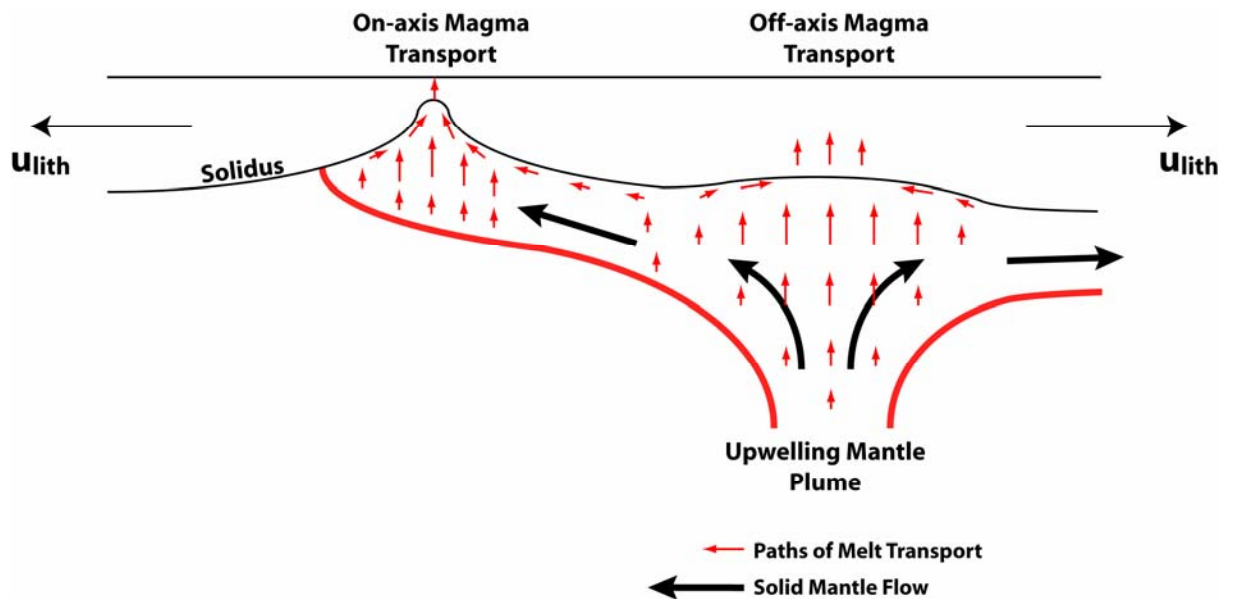


**Figure 1.** Conceptual model of an upwelling, near-ridge mantle-plume, melting, melt transport, and magmatic heating of the lithosphere. Melting occurs primarily beneath the ridge-axis and in the plume stem and the resultant melt is transported (red arrows) vertically through the mantle and along the solidus at the base of the lithosphere (inset). Melt travels up the slope of the solidus until it reaches an area of small slope or high porosity allowing magma transport through the lithosphere. Shear stresses are imposed upon the lithosphere due to the solid flow of the upwelling mantle plume (black arrows).

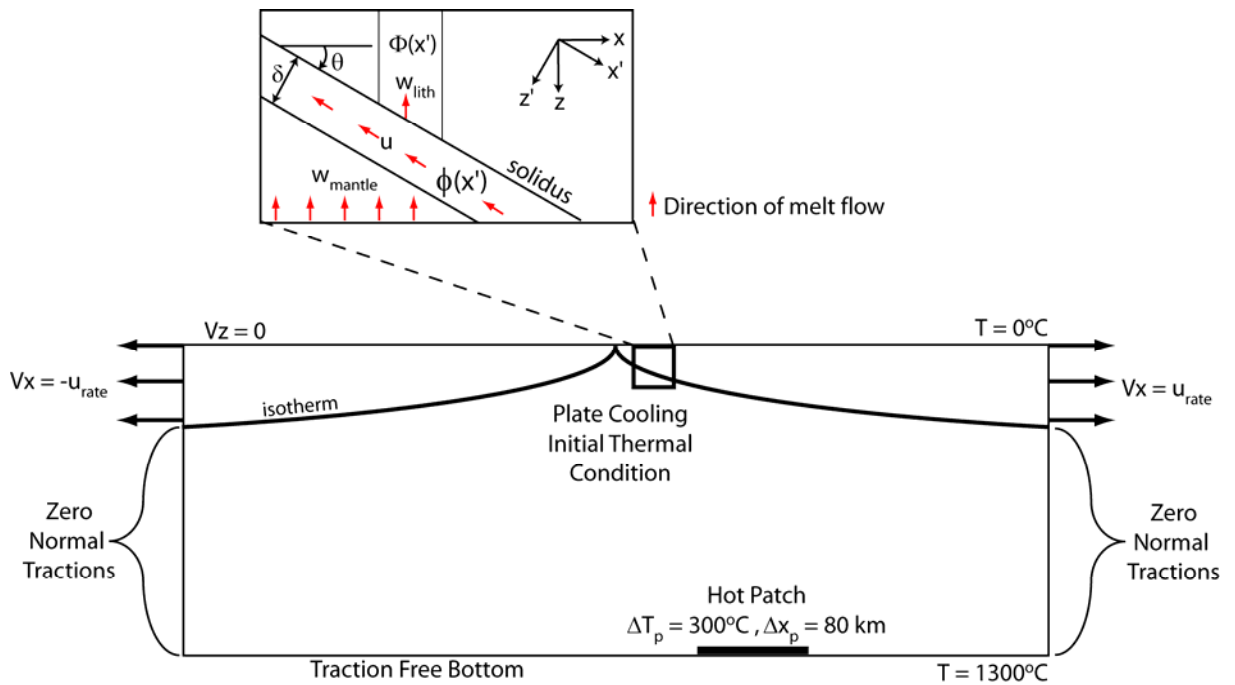


**Figure 2.** A cartoon of the boundary and initial conditions of the model and the geometry of melt transport. To simulate plate spreading, velocities in the x direction (black arrows) are imposed along the top 80 km of the left and right edges of the model domain. Below 80 km, normal tractions along the edges are set to zero. The bottom of the box is traction free while the top of the box is shear traction free and has a zero vertical velocity. The initial thermal condition is a plate cooling model (isotherm represented by curved black line) and an imposed hot patch (black box) with a maximum plume excess temperature of  $\Delta T_p = 300^\circ\text{C}$  multiplied by a Gaussian distribution 80 km wide at the bottom of the box to initiate a plume-like upwelling. (inset) Melt is transported vertically through the mantle ( $w_{mantle}$ ) until it encounters the solidus where it accumulates and travels up the slope of the lithosphere ( $\theta$ ). Melt flux through the lithosphere ( $w_{lith}$ ) is controlled by the porosity ( $\phi$ ) beneath the solidus and the average porosity of the lithosphere ( $\Phi$ ).

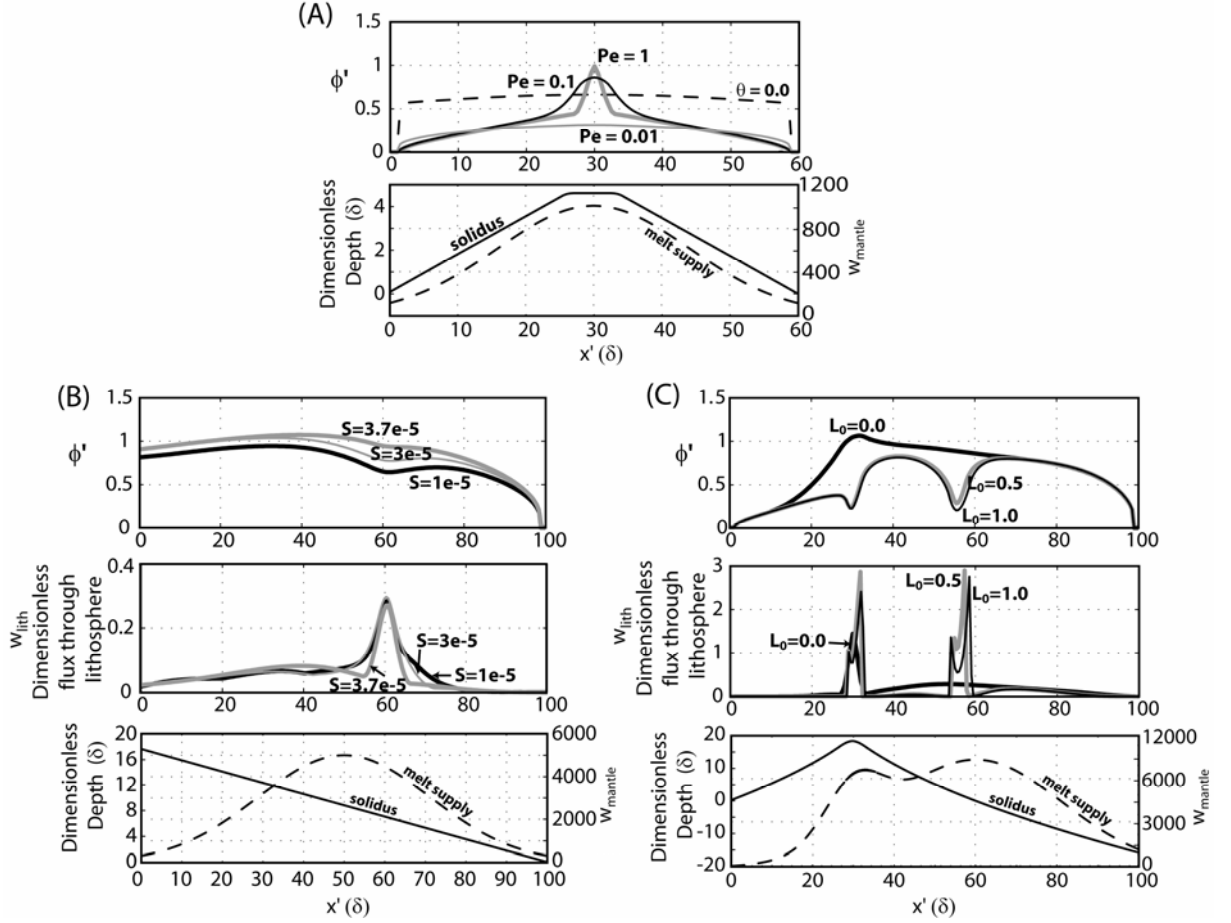


**Figure 3.** (A) The porosity beneath a solidus with a “ridge-axis”-like slope and a Gaussian melt flux from below (solid lines) strongly depends upon the Peclét number  $Pe$ . A solution for an impermeable, flat lithosphere (dashed line) is shown for reference. Other parameters are  $D = 0.313$ ,  $w_{l0}/w_{m0} = 7.84e4$ ,  $\phi_0 = 0.1$ ,  $H_0 = 1000$ ,  $S = 8e-5$ ,  $L_0 = 0.0$ . (B) The width of the region of melt flux through the lithosphere above a uniformly sloped solidus ( $10^\circ$ , down to the right) with a melt flux distributed in a Gaussian manner around  $x = 50$ , decreases with increasing values of the healing rate scale  $S$ . The peak in magma flux moves with damage as it is advected across the model. Melt is allowed to flow out the left boundary and porosity is set to 0 on the right edge. Other parameters are  $Pe = 0.022$ ,  $D = 0.46$ ,  $w_{l0}/w_{m0} = 3924$ ,  $\phi_0 = 0.1$ ,  $H_0 = 1000$ ,  $L_0 = 0.167$ . (C) Different values of  $L_0$  are shown for a case with a “ridge-axis”-like solidus slope and a melt flux from below equal to the sum of two Gaussian sources

centered at  $x = 30$  and  $x = 60$ . Other parameters are  $Pe = 0.1$ ,  $D = 0.25$ ,  $w_{10}/w_{m0} = 7.84e4$ ,  $\phi_0 = 0.1$ ,  $H_0 = 1000$ ,  $S = 6.5e-6$ .

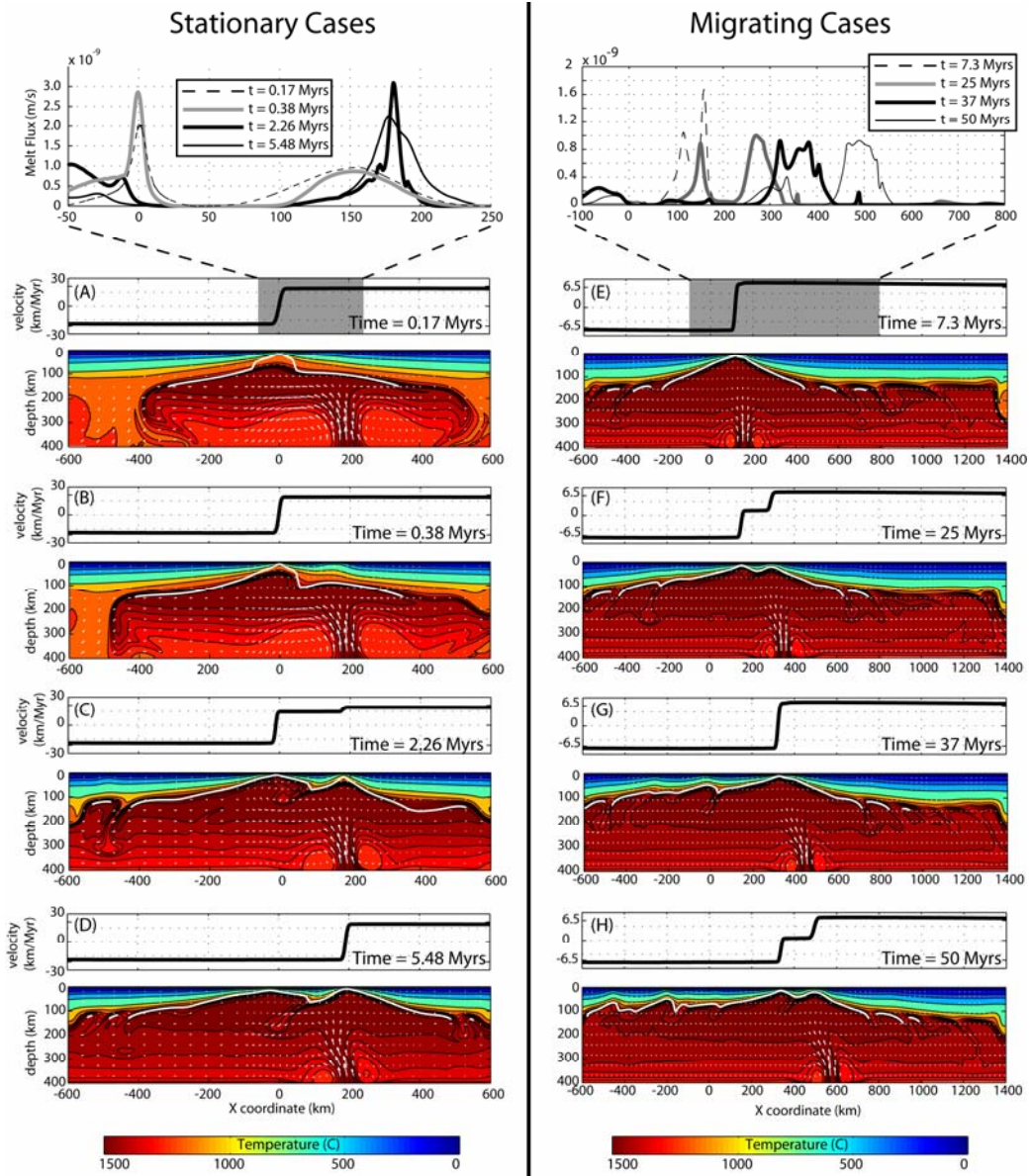


**Figure 4.** The temporal evolution of a case of Type 2 with a (left) fixed plume location ( $x=200$  km) for a half-spreading rate of 20 km/Myr and (right) with a plume migrating at 10 km/Myr for a half-spreading rate of 10 km/Myr. Colors show contours of temperature (see scales at bottom of the figure) with arrows representing mantle flow and a white contour marking the solidus at the top of the melting zone along which melt

from the mantle flows to where it penetrates the lithosphere. Velocities across the top of the model (thick black lines) are shown above each set of temperature contours. Boxes at the top show the magma flux crossing the solidus into the lithosphere in the region of interest for each case (line colors/styles correspond to the times marked for each panel).

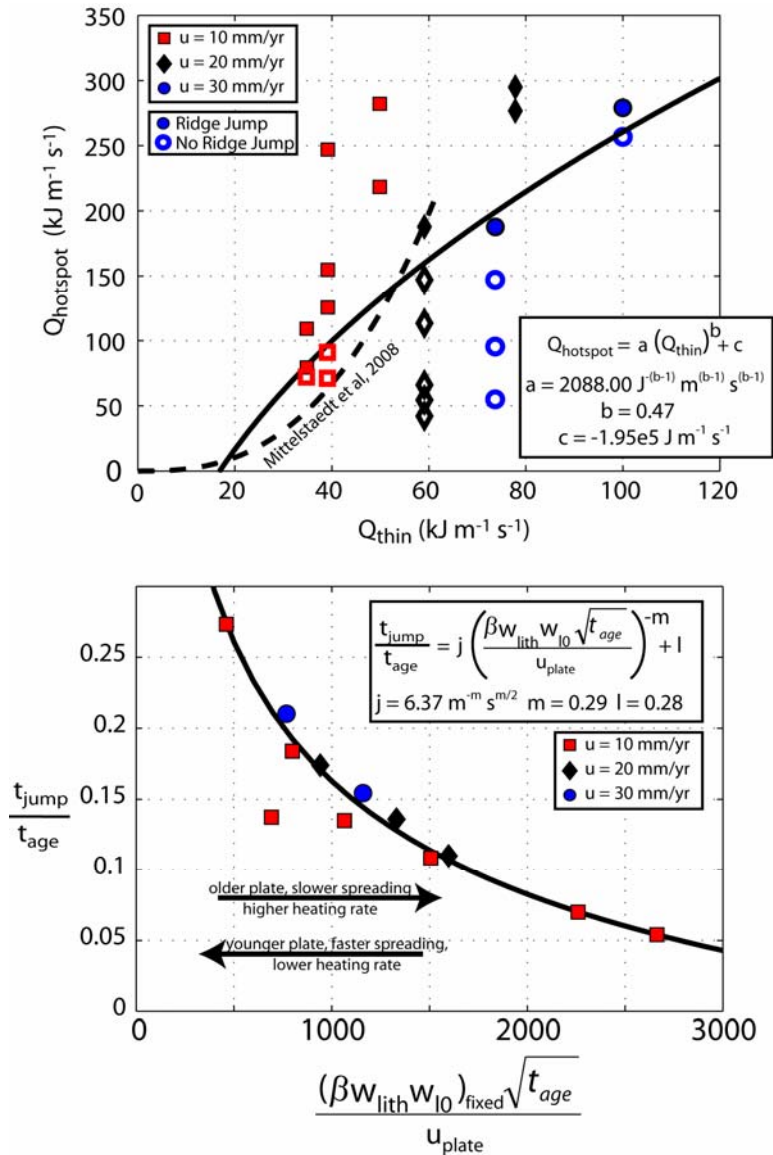


**Figure 5.** (top) Ridge jumps (solid symbols) in cases of Type 1 occur when the value of  $Q_{\text{hotspot}}$  is greater than  $AQ_{\text{thin}}^b + c$ , where  $a = 2088.00$ ,  $b = 0.47$ , and  $c = -1.95\text{e}5$  (solid black line), but not for values less than this (open symbols). Results include cases with

half-spreading rates of 10 km/Myr (red squares), 20 km/Myr (black diamonds) and 30 km/Myr (blue circles). Values of  $Q_{hotspot}$  are larger than that predicted by *Mittelstaedt et al.* [2008] (dashed line) partly due to warm plume material underlying and weakening the ridge axis (section 3.6). (bottom) The time to jump  $t_{jump}$  scaled by the age of the lithosphere  $t_{age}$  where a jump occurs is a function (black line) of the heating rate parameter ( $\beta w_{lith}$ ), the thickness of the lithosphere ( $z_{lith} \sim t_{age}^{1/2}$ ), and the advection of material through the heating zone ( $u_{rate}$ ).

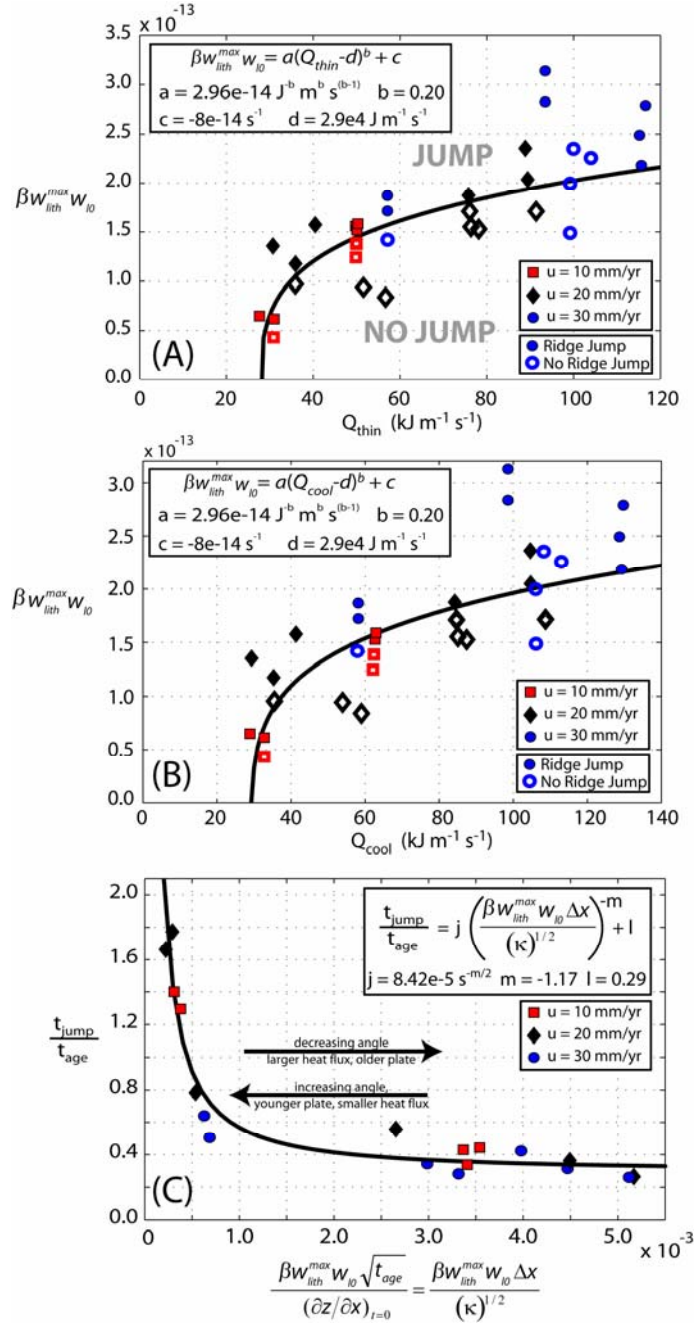


**Figure 6.** (A) Ridge jumps (solid symbols) for cases of Type 2 occur when the value of the maximum heating rate parameter  $\beta w_{lith}^{max} w_{l0} = A(Q_{thin} - d)^b + c$  where  $a = 2.96e-14 \text{ J}^{-b} \text{ m}^b \text{ s}^{b(b-1)}$ ,  $b = 0.2$ ,  $c = -8e-14 \text{ s}^{-1}$ , and  $d = 2.9e4 \text{ J m}^{-1} \text{ s}^{-1}$ , but not in general for values less than this (open symbols). Symbols for different spreading rates are as labeled. (B) The model results show a similar fit to the scaling law when plotted versus  $Q_{cool}$ , the time-

integrated surface heat loss of a mantle half-space used to estimate  $Q_{thin}$ . This relationship is used to calculate the curves in Figure 9. (C) The time to jump  $t_{jump}$  scaled by the age of the lithosphere to which the ridge jumps is a function of the maximum heating rate parameter  $\beta w_{lith}^{max}$ , the thickness of the lithosphere ( $z_{lith} \sim t_{age}^{1/2}$ ), and the slope of the lithosphere at time  $t = 0$  ( $dz_{lith}/dx = \partial/\partial x (f \sqrt{\kappa t_{age}})$ ).

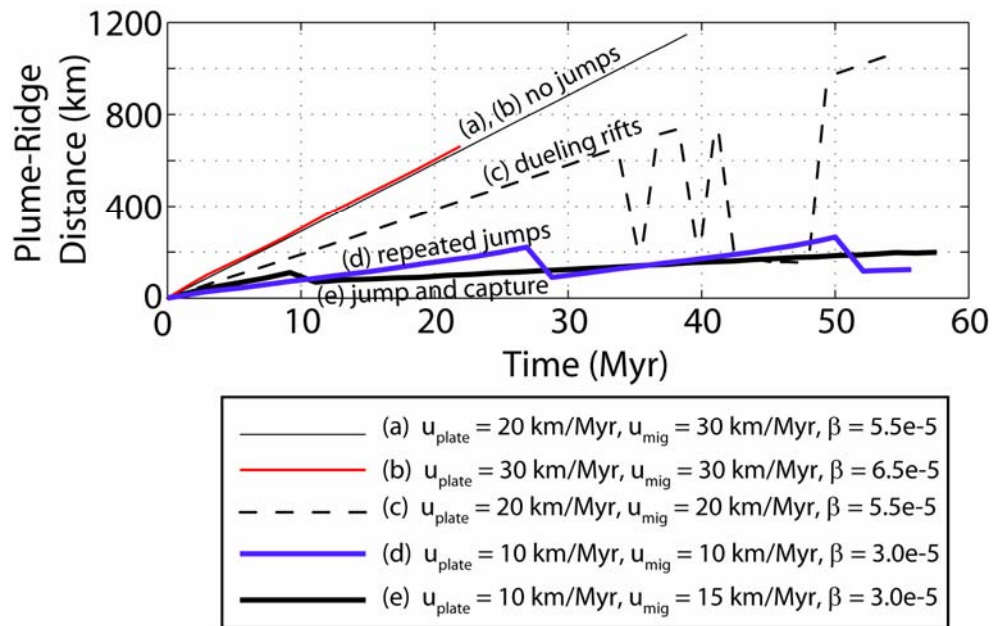


**Figure 7.** Models where the plume migrates relative to the ridge axis display a variety of behavior including (a, b) migration with no jumps, (c) two rifts with divergence shifting between them, (d) repeated ridge jumps, and (e) a single ridge jump followed by ridge capture.

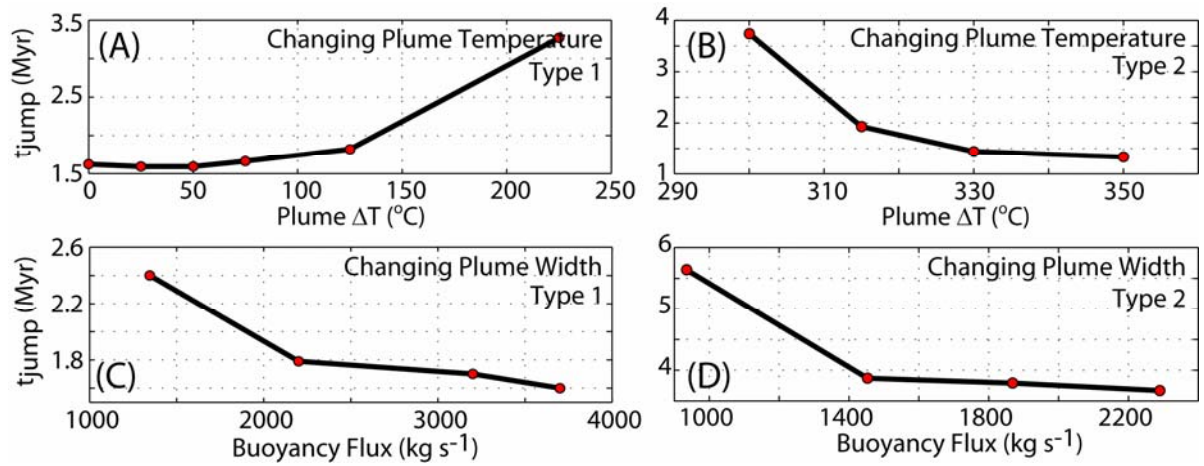


**Figure 8.** (A) Increasing plume temperature  $\Delta T_p$  for a case of Type 1 decreases the ridge-axis strength and results in larger values of  $t_{jump}$ . (B) Increases in  $\Delta T_p$  in Type 2 cases result in sharp decreases in  $t_{jump}$  due to increasing melt flux from the mantle at the hotspot. Increases in the buoyancy flux  $B$  at constant  $\Delta T_p$  (changes to plume conduit width) of both (C) Type 1 and (D) Type 2 cause a decrease in  $t_{jump}$ .

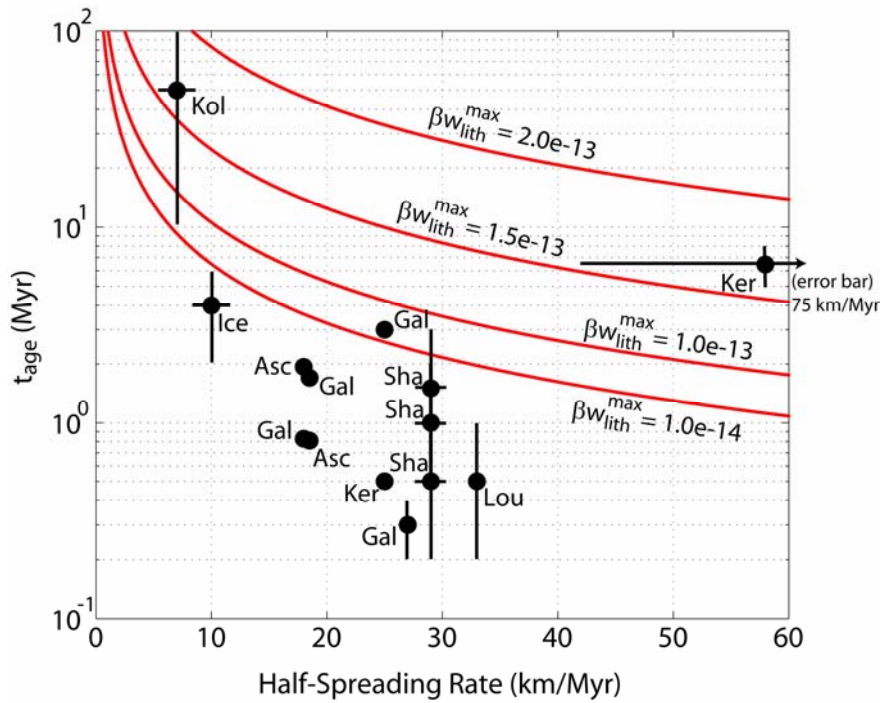


**Figure 9.** Observed half spreading rates and age of the lithosphere where jumps occurred  $t_{age}$  are shown (black circles) for several locations including the Ascension hotspot (Asc), the Galapagos hotspot (Gal), Iceland (Ice), the Kerguelen hotspot (Ker), the Kolbeinsey Ridge (Kol), the Louisville hotspot (Lou), and Shatsky Rise (Sha). Curves indicate the maximum value of  $t_{age}$  and spreading rate at the indicated value of  $\beta w_{lith}^{max}$  that jumps are predicted to occur (jumps are predicted to occur below these curves). Bars show the estimated observation error. For locations where no error bars are visible, errors are either smaller than the symbol or unknown. The Kolbeinsey ridge jumped into continental lithosphere and the values shown are estimated assuming that the depth of the lithosphere-asthenosphere boundary just prior to rifting [Mjælde et al., 2008] is the effective elastic thickness of the lithosphere. The age shown is the equivalent age of oceanic lithosphere with the same elastic thickness [Burov and Diament, 1995]. Data is from the following authors [Sæmundsson, 1974; Brozena and

*White, 1990; Krishna et al., 1995; Small, 1995; Wilson and Hey, 1995; Hardarson et al., 1997; Geli et al., 1998; Nakanishi et al., 1999; Krishna and Rao, 2000; LaFemina et al., 2005; Breivik et al., 2006; Desa et al., 2006; Mjelde et al., 2008].*

## Appendix A

Because the lithosphere is thickening approximately with the square-root of distance from the ridge, it accretes in a curved form. As the lateral extent is much larger than its thickness, the lithosphere can be approximated as a thin shell. The shape of a thin shell may be described in terms of two orthogonal coordinates,  $\alpha$  and  $\beta$ , which in general are curvilinear [Gould, 1988]. Infinitesimal changes in  $\alpha$  and  $\beta$  are related to changes in arc length along the mid plane of the shell,  $ds_\alpha$  and  $ds_\beta$ , according to

$$\begin{aligned} ds_\alpha &= A d\alpha \\ ds_\beta &= B d\beta \end{aligned} \quad (\text{A1})$$

where  $A$  and  $B$  are known as Lamé parameters and, for the lithosphere, I define  $d\alpha = dx_1$  and  $d\beta = dx_2$  (Fig. 2). Using this convention,  $B = 1$  (no curvature parallel to the ridge) and  $A$  is found to be

$$A = \left( 1 + \left( \frac{dx_3}{dx_1} \right)^2 \right)^{1/2} \quad (\text{A2})$$

where  $dx_3/dx_1$  describes the slope of the shell mid-plane. Using this curvilinear geometry, force equilibrium can be described in three orthogonal directions [Gould, 1988]

$$\left[ (BN_\alpha)_{,\alpha} + (AN_{\beta\alpha})_{,\beta} + A_{,\beta} N_{\alpha\beta} - B_{,\alpha} N_\beta \right] + Q_\alpha \frac{AB}{R_\alpha} + q_\alpha AB = 0 \quad (\text{A3})$$

$$\left[ (BN_{\alpha\beta})_{,\alpha} + (AN_\beta)_{,\beta} + B_{,\beta} N_{\beta\alpha} - A_{,\alpha} N_\alpha \right] + Q_\beta \frac{AB}{R_\beta} + q_\beta AB = 0 \quad (\text{A4})$$

$$\left[ (BQ_\alpha)_{,\alpha} + (AQ_\beta)_{,\beta} \right] - N_\alpha \frac{AB}{R_\alpha} - N_\beta \frac{AB}{R_\beta} + q_n AB = 0 \quad (\text{A5})$$

where partial derivatives are denoted by commas followed by coordinate directions (to be complete I show the terms involving derivatives of  $B$  even though they are zero).  $R_i$  is the radius of curvature in the  $i$  direction,  $Q_i$  is depth integrated transverse shear, and  $q_i$  are the loads on the plate. These equilibrium equations are coupled through the transverse shear term,  $Q_i$ , which also acts to couple them with the equations of angular momentum.

To simplify equations A3-A5, I determine the appropriate values of the Lamé parameter  $A$  and the radii of curvature of the unstressed lithosphere. Assuming the slope of the mid-plane ( $dx_3/dx_1$ , eq. A2) is parallel to the surface of the lithosphere, radius of curvature may be described by seafloor deepening due to plate cooling away from the ridge [Stein and Stein, 1992]

$$z = 2.60 + c\sqrt{x_1} \quad (\text{A6})$$

where  $c = \frac{0.365}{\sqrt{u}}$ ,  $u$  is the seafloor spreading rate, and  $x_1$  is the distance from the ridge.

Thus, equation A2 becomes

$$A = \left( 1 + \left( \frac{c^2}{4x_1} \right) \right)^{(1/2)} \quad (\text{A7})$$

For  $u = 30$  km/myr and  $x_1 = 10$ -100 km off axis,  $(c^2/4x_1)$  is of order  $10^{-4}$  to  $10^{-5}$  so  $A$  is very close to 1.

The radius of curvature in the ridge parallel direction,  $R_\beta$ , is infinite because I assume all curvature is parallel to plate spreading and radius of curvature due to uplift is large. The radius of curvature perpendicular to the ridge axis is

$$R_\alpha = \frac{\left[1 + \left(\frac{dx_3}{dx_1}\right)^2\right]^{(3/2)}}{\frac{d^2 x_3}{dx_1^2}}. \quad (\text{A8})$$

Again using  $u = 30$  km/myr and  $x_l = 10$  km, the radius of curvature near the ridge (0.33 m.y. old crust) is found to be  $R_\alpha > \sim 1900$  km. I expect the stress resultant terms in (A3) – (A5) to be of order  $N_{ij}/R_p$  where  $R_p \sim 10^2$  km is the characteristic radial extent that plume forces,  $q_i$ , act on the plate. Since  $R_\alpha \gg R_p$ , the terms involving  $R_\alpha^{-1}$  (and  $R_\beta^{-1}$ ) in (A3) – (A5) are negligible and the resulting linear momentum equations have a form similar to those of plane stress (with  $A = B = 1$ )

$$\left[ (N_\alpha)_{,\alpha} + (N_{\beta\alpha})_{,\beta} \right] + q_\alpha = 0 \quad (\text{A9})$$

$$\left[ (N_{\alpha\beta})_{,\alpha} + (N_\beta)_{,\beta} \right] + q_\beta = 0. \quad (\text{A10})$$

I use these equations of equilibrium to formulate a model of plume-ridge interaction.

## Appendix B

To derive the governing equation for a plate with thickness,  $h$ , that varies laterally, the constitutive equations (Eq. 3) are substituted into the equilibrium (Eq. 2) equations to yield

$$\frac{Eh}{(1-\nu^2)} \left[ \frac{\partial \varepsilon_{11}}{\partial x_1} + \nu \frac{\partial \varepsilon_{22}}{\partial x_1} \right] + \frac{Eh}{(1+\nu)} \frac{\partial \varepsilon_{12}}{\partial x_2} = - \left[ q_1 + \frac{\partial h}{\partial x_1} \frac{N_{11}}{h} + \frac{\partial h}{\partial x_2} \frac{N_{12}}{h} \right] = b_1, \quad (\text{B1})$$

$$\frac{Eh}{(1-\nu^2)} \left[ \frac{\partial \varepsilon_{22}}{\partial x_2} + \nu \frac{\partial \varepsilon_{11}}{\partial x_2} \right] + \frac{Eh}{(1+\nu)} \frac{\partial \varepsilon_{12}}{\partial x_1} = - \left[ q_2 + \frac{\partial h}{\partial x_2} \frac{N_{22}}{h} + \frac{\partial h}{\partial x_1} \frac{N_{12}}{h} \right] = b_2, \quad (\text{B2})$$

and compatibility (Eq. 4) equation to yield

$$(1-\nu) \left[ \frac{\partial^2 \frac{N_{11}}{h}}{\partial x_2^2} + \frac{\partial^2 \frac{N_{22}}{h}}{\partial x_1^2} \right] - \nu \left[ \frac{\partial^2 \frac{N_{22}}{h}}{\partial x_2^2} + \frac{\partial^2 \frac{N_{11}}{h}}{\partial x_1^2} \right] = 2 \frac{\partial^2 \frac{N_{12}}{h}}{\partial x_1 \partial x_2}. \quad (\text{B3})$$

Terms with gradients in thickness are placed on the right hand side (r.h.s.) of Equations (B1) and (B2) and are grouped as “fictitious” body forces into new variables,  $b_1$  and  $b_2$ , which also include the effects of plume shear and uplift ( $q_1$  and  $q_2$ , see Eq. 9). Formulation of the governing equation is achieved by combining the compatibility and equilibrium equations as is commonly done in elasticity theory. To facilitate this, derivatives of equations B1 and B2 are taken in the 1 and 2 directions respectively and the resulting equations are summed

$$-\frac{\partial^2 \frac{N_{11}}{h}}{\partial x_1^2} - \frac{\partial^2 \frac{N_{22}}{h}}{\partial x_2^2} - \left( \frac{\partial \frac{b_1}{h}}{\partial x_1} + \frac{\partial \frac{b_2}{h}}{\partial x_2} \right) = 2 \frac{\partial^2 \frac{N_{12}}{h}}{\partial x_1 \partial x_2} \quad (\text{B4})$$

Now I may solve for the general governing equation for an elastic plate of varying thickness by equating the r.h.s. of (B4) and (B3) and simplifying

$$\nabla^2(\bar{\sigma}_{11} + \bar{\sigma}_{22}) = -\frac{1}{(1-\nu)} \left[ \frac{\partial b_1}{\partial x_1} + \frac{\partial b_2}{\partial x_2} \right] \quad (\text{B5})$$

The governing equation relates the change in depth-averaged stresses ( $\bar{\sigma}_{ij} = N_{ij} / h$ ) in a plate of varying thickness to the imposed loads ( $q_i$ ), subject to specified (ridge axis) boundary conditions. The form of (B5) is identical in form to the governing equation for plane stress and allows the solution to be determined through the use of an Airy stress function method. Because the final value of the “fictitious” body force terms depend on the stress resultants, the equations are solved iteratively.

## Appendix C

### 1. Melt Transport Equations

#### 1.1 Equations of Two-Phase Flow

First introduced by *McKenzie* [1984], the following set of equations describe the conservation of mass and momentum of a buoyant, low viscosity fluid interacting with a deformable, porous, high-viscosity matrix; two-phase flow of melt through a viscous mantle. The two fluids are coupled by the melting rate of the matrix  $\Gamma$  and the flow of the melt through the matrix in response to gravity and viscous deformation

$$\frac{\partial \rho_m \phi}{\partial t} + \nabla \cdot (\rho_m \phi \mathbf{u}_m) = \Gamma \quad (\text{C1})$$

$$\frac{\partial \rho_s (1 - \phi)}{\partial t} + \nabla \cdot (\rho_s (1 - \phi) \mathbf{u}_s) = -\Gamma \quad (\text{C2})$$

$$\phi(\mathbf{u}_m - \mathbf{u}_s) = -\frac{\mathbf{k}}{\mu_m} [\nabla(P - \rho_m g z)] \quad (\text{C3})$$

$$\nabla P = \nabla \cdot \left( \eta [\nabla \mathbf{u}_s + \nabla \mathbf{u}_s^T] \right) + \nabla \cdot \left[ \left( \zeta - \frac{2}{3} \eta \right) \nabla \cdot \mathbf{u}_s \right] + \bar{\rho} g \quad (\text{C4})$$

where  $\rho$  is the density (subscripts refer to the melt  $m$ , and the solid  $s$ ),  $\mathbf{u}_m$  is the melt velocity vector,  $\mathbf{u}_s$  is the matrix velocity (bold symbols denote vector quantities),  $g$  is the acceleration of gravity,  $\mathbf{k}$  is the permeability tensor,  $\phi$  is the porosity of the solid,  $t$  is time,  $\mu_m$  is the viscosity of the melt,  $P$  is the fluid pressure,  $\eta$  and  $\zeta$  are the shear and “effective” bulk viscosities of the solid, and  $\bar{\rho} = \rho_m \phi + \rho_s (1 - \phi)$  is the average density of the system. The first two equations describe the conservation of mass of the melt and the solid respectively with the transfer of mass between the two phases being governed

by the melting rate  $\Gamma$ . Equation (C3) is a modified version of Darcy's law that describes the momentum conservation of the melt phase. Conservation of momentum of the solid matrix is given by equation (C4) where pressure gradients within the solid are balanced by viscous deformation and the buoyancy difference between the melt and the solid.

## 1.2 Simplified Equations

The location and magnitude of magma flux through the lithosphere (i.e. out of the mantle) is calculated by using a set of simplified equations of melt flow along the top of the melting zone (i.e. the solidus) and a parameterization for magma transport through the lithosphere. The major simplification I make here is that the pressure gradients associated with matrix shear and compaction are negligible compared to that associated with melt buoyancy (i.e. the zero compaction length approximation of *Spiegelman* [1993]). In this case, melt transport is decoupled from viscous flow of the solid. In addition, since the description of melt transport is 1D along the solidus, I define the melt supply from below  $w_{mantle}$  separately from the melt flux penetrating the lithosphere  $w_{lith}$  and approximate the gradient in vertical melt flux as  $(w_{lith} - w_{mantle})/\delta$ , where  $\delta$  is constant (1 km). With no melting at the solidus ( $\Gamma=0.0$ ), just below the lithosphere, I arrive at a description of the melt transport at the top of the melting zone,

$$\frac{\partial \rho_m \phi}{\partial t} + \rho_m \left( \frac{\partial \mathbf{u}}{\partial x'} + \frac{\partial \mathbf{w}}{\partial z'} \right) = 0 \quad (C5)$$

$$\mathbf{u} = \frac{-k_0 \phi^n}{\mu_m} (\rho_s - \rho_m) g \left[ \sin(\theta) + \Delta z \frac{\partial \phi}{\partial x'} \right] \quad (C6)$$

$$w_{mantle} = - \int_{z_{max}}^{z_{solidus}} \left( \frac{dF}{dP} \right) \rho_s g \mathbf{u}_z^s dz \quad (C7)$$

$$w_{lith} = \frac{-k_0 \Phi^n}{\mu_m} (\rho_s - \rho_m) g \cos(\theta) \quad (C8)$$

where  $k_0$  is the reference permeability,  $\mathbf{u}_z^s$  is the vertical velocity of the solid,  $\theta$  is the angle of the solidus relative to the horizontal, and  $\mathbf{u}$  is the average melt flux in the direction parallel to the solidus  $x'$ . Equation (C5) is the equation of conservation of mass; balancing the change in porosity with the divergence of melt flux. Equation (C6) is an extended form of Darcy's law describing the average melt flux parallel to the solidus where the driving forces are melt buoyancy and pressure gradients associated with lateral variations in porosity. The form of (C6) is based on the assumption that the melt pressure is equal to the average pressure in a layer below the solidus where porosity only varies laterally

$$P = \rho_s g z_{solidus} + (1 - \phi(x')) \frac{\rho_s g \delta}{2} + \phi(x') \frac{\rho_m g \delta}{2} \quad (C9)$$

where  $z_{solidus}$  is the depth to the solidus. Equation (C7) describes the melt supply from below and is equal to the depth integrated melting rate in the mantle. Equation (C8) is the melt flux penetrating the lithosphere in the direction perpendicular to the solidus  $z'$ . The flow of melt in the  $x'$  and  $z'$  directions depends on the porosity  $\phi$  at the solidus and the characteristic porosity  $\Phi$  in the overlying lithosphere respectively (Equations (C6) and (C8)). Calculation of the lithospheric porosity  $\Phi$  is discussed below.

Combining (C5-C8) yields the governing equation of the transport of melt along the solidus

$$\frac{\partial \phi}{\partial t} - \frac{\Delta \rho g k_0}{\mu_m} \frac{\partial}{\partial x} \left( \phi^n \sin(\theta) + \Delta z \phi^n \frac{\partial \phi}{\partial x} \right) = \frac{w_{mantle} - w_{lith}}{\delta} \quad (C10)$$

where primes indicating the solidus reference frame have been dropped. To isolate the fundamental parameters that control melt transport, I derive the non-dimensional form of Equation (C10) using the following scaling factors

$$\phi = \phi_0 \phi'; \quad x = \delta x'; \quad t = \tau t'; \quad k = k_0 \phi'^n; \quad \tau = \frac{\delta^2}{\kappa_0};$$

$$w_{mantle} = w_{m0} w'_{mantle}; \quad w_{m0} = \frac{\delta \phi_0}{\tau}; \quad u = u_0 \phi'^{n-1}; \quad u_0 = \frac{\Delta \rho g}{\mu_m} k_0 n \phi_0^{n-1};$$

$$\kappa_0 = \Delta z \frac{\Delta \rho g}{\mu_m} k_0 \phi_0^n; \quad w_{lith} = w_{l0} w'_{lith}; \quad w_{l0} = \frac{\Delta \rho g}{\mu_m} k_0 \left( \frac{\Phi_{max}}{2} \right)^n$$

where  $\Delta z$  is the length scale that controls lateral melt transport associated with gradients in  $\phi$ ,  $\phi_0$  is the reference porosity,  $u_0$  is the reference melt velocity,  $w_{l0}$  is the reference melt flux crossing the solidus,  $w_{m0}$  is the reference melt supply from below, and  $\tau$  is the time-scale (see table C1 for parameter definitions). Substituting these scaling factors into (C10) and dropping primes I am left with,

$$\frac{\partial \phi}{\partial t} - Pe \left[ \phi^{n-1} \sin(\theta) \frac{\partial \phi}{\partial x} - \frac{\phi^n}{n} \cos(\theta) \frac{\partial \theta}{\partial x} \right] - \frac{\partial}{\partial x} \left[ \phi^n \frac{\partial \phi}{\partial x} \right] = w_{mantle} - \frac{w_{l0}}{w_{m0}} w_{lith}. \quad (C11)$$

This transport equation is controlled by two parameters: the Peclet number  $Pe (= \delta u_0 / \kappa_0)$  controls the magnitude of melt transport along the sloping boundary driven by buoyancy relative to that driven by lateral porosity gradients (which behaves mathematically like diffusion); and  $w_{l0}/w_{m0}$ , describes the maximum melt flux through the lithosphere relative to that generated by melting below.

To complete the description of melt transport along the solidus, I must define the lithospheric porosity  $\Phi$ . Following a similar methodology to *Hieronymus and Bercovici* [2001], I assume that the change in energy associated with small changes in  $\Phi$  is controlled by energy inputs from changes to the excess melt pressure beneath the lithosphere  $\sigma_p$  and the change in damage (generally due to chemical, physical, and thermal processes) of the lithosphere caused by magma passing through it  $\varepsilon$ ,

$$Cd\Phi = d\sigma_p + B_0d\varepsilon, \quad (\text{C12})$$

where  $B_0$  is a prescribed constant and  $C$  controls the change in porosity due to the two factors  $\sigma_p$  and  $\varepsilon$  and is defined such that the porosities in the lithosphere vary between 0 and  $\Phi_{max}$ ,

$$C = \frac{C_0}{\Phi(\Phi_{max} - \Phi)}. \quad (\text{C13})$$

Substituting (C13) into (C12) and integrating yields an equation for lithospheric porosity

$$\Phi = \frac{\Phi_{max}}{2} \left( 1 + \tanh \left( \frac{A_0 \phi \cos(\theta) - \sigma_c + B_0 H_r}{2C_0 / \Phi_{max}} \right) \right). \quad (\text{C14})$$

The value of the characteristic lithospheric porosity described by (C14) is controlled by the balance between the melt driving pressure perpendicular to the solidus  $\sigma_p = A_0 \phi \cos(\theta)$ , the damage associated with erosion of the lithosphere as magma passes through it  $B_0 H_r$  where  $H_r$  is the “reduced” time-integrated melt flux (see below), and the intrinsic (constant) strength of the lithosphere described by cohesion  $\sigma_c$ . Thus, the lithospheric porosity increases in response to a combination of increasing melt pressures and time-integrated magmatic damage.

The “reduced” time-integrated magma flux is defined by a modified advection equation (dimensional)

$$\frac{\partial H_r}{\partial t} = w_{lith} w_{l0} - \frac{\partial(H_r u_{plate})}{\partial x} - \text{healing rate} \quad (C15)$$

where  $u_{plate}$  is the velocity of the overlying lithosphere. To define a healing rate, I assume that a continuously active magma conduit has a width  $w$  that is proportional to the time-integrated melt flux

$$w \propto H = \int w_{lith} w_{l0} dt .$$

If  $w$  describes the length scale for thermal diffusion in the magma conduit

$$\frac{\partial T}{\partial t} = \kappa \frac{\partial^2 T}{\partial x^2} \propto \frac{\Delta T}{w^2}$$

and the healing rate is proportional to  $dT/dt$ , I assume a healing rate proportional to the square of the “reduced”, time-integrated magma flux

$$\frac{S}{(H_r + H_0)^2} , \quad (C16)$$

where  $S$  is the healing rate scale. This relationship leads to larger healing rates for smaller integrated magma fluxes and a maximum healing rate defined by  $S/H_0^2$  which controls the minimum required magma flux necessary to damage the lithosphere and increase its porosity.

Finally, to define the reference melt flux through the lithosphere  $w_{l0}$ , I combine equations (C14) and (C8) with the following scaling factors (primes denote dimensionless parameters)

$$\sigma_p = \sigma_{p0} \phi' \cos(\theta); \quad \sigma_{p0} = A_0 \phi_0; \quad \sigma_c = \sigma_{p0} \phi'_{coh};$$

$$D = \frac{2C_0}{\Phi_{\max}} = \sigma_{p0} D'; \quad B_0 H_r = L_0 \sigma_{p0} H'; \quad H_r = H_0 H';$$

where  $L_0$  is a factor controlling the sensitivity of lithospheric porosity to damage,  $\sigma_{p0}$  is the melt pressure at the reference porosity  $\phi_0$ ,  $H_0$  is the reference integrated damage parameter, and  $A_0$  is a constant, to yield (dropping primes),

$$w_{lith} = \cos(\theta) \left[ 1 + \tanh \left( \frac{\phi \cos(\theta)}{D} - \frac{\phi_{coh}}{D} + \frac{L_0 H}{D} \right) \right]^n. \quad (C17)$$

This equation states that the flux of magma is controlled by the balance between the dimensionless melt porosity  $\phi$ , the dimensionless porosity required to overcome the strength of the lithosphere  $\phi_{coh}$ , and the effect of magmatic damage  $L_0 H$ . The magma flux through the lithosphere varies over a range of  $\phi \cos(\theta) - \phi_{coh} + L_0 H$ , controlled by the scale factor  $D$ , from 0 to its maximum value of  $4 \cos(\theta)$ .

### 1.3 Numerical Implementation

Equation (C11) describes advective and diffusive porosity transport with both a source and sink ( $w_{lith}$  and  $w_{mantle}$ ). Each of the spatial derivatives is approximated with a second order finite-difference approximation and time is advanced using a 1<sup>st</sup> order, explicit, Euler scheme with a time-step less than or equal to  $\frac{1}{2}$  of the Courant limit. The diffusive terms are approximated with centered differencing and the advective terms by upwind differencing. Equations (C11) is formulated in terms of the  $x'$  and  $z'$  directions which in detail vary along the solidus, but such changes introduce small terms in the conservation equations and are therefore neglected.

## 2. Benchmarks With Analytical Solutions

To verify the numerical solutions, I compare them to several simple, steady-state ( $\partial\phi/\partial t = 0.0$ ) analytical solutions which neglect either the terms associated with gradients in porosity ( $Pe = \text{large}$ ) or the terms accounting for the slope of the solidus ( $Pe = 0.0$ ). All cases are shown in Figure C1 with RMS values of the maximum difference between the numerical and analytical solution divided by the maximum porosity of the analytical solutions.

### 2.1 Flat Lithosphere, Uniform Melt Flux From Below ( $Pe=0.0$ , $w_{lith}=0.0$ , $\theta=0.0$ )

The first case is that of a flat solidus that is everywhere impermeable to melt with a uniform melt flux from below. The Peclet number is set to 0 so flow is controlled only by gradients in porosity (C11). Dimensionless porosity  $\phi$  is set to zero on both the left and right hand sides of the domain. The analytical solution is

$$\phi = \left( (n+1) \left[ \frac{-w_{mantle}x^2}{2} + \frac{w_{mantle}L}{2}x \right] \right)^{1/(n+1)} \quad (C18)$$

where the uniform melt flux from below  $w_{mantle}$  is balanced by the melt flux out the sides of the domain at  $x' = 0$  and  $x' = 100$ . Comparing this solution to the numerical method for  $n = 1, 2$ , and  $3$  results in a very close matches with  $RMS \leq 0.03$ .

### 2.2 Flat Lithosphere with Fixed $w_{lith}$ ( $Pe=0.0$ , $w_{lith}=\text{fixed @ } x=50$ , $\theta=0.0$ )

The second analytical solution is similar to that in 2.1, but a constant porosity flux  $Q$  is set on the left-hand boundary of the analytical solution. The analytical solution for  $n=1$  is

$$\phi = \left[ -w_{mantle}x^2 + (-Q^2L \pm QL\sqrt{1+w_{mantle}})x + \frac{(-Q^2L \pm QL\sqrt{1+w_{mantle}})^2}{2Q^2} \right]^{1/2}. \quad (C19)$$

To compare the numerical solutions to this case, the numerical domain is doubled in size and the vertical flux is set to 2\*Q at the center of the domain. This case is somewhat similar to a ridge with melt reaching the seafloor at the axis. The comparison of the two solutions shows an RMS error of 0.00223.

### 2.3 Sloped Lithosphere Without Diffusion ( $Pe=10$ , $w_{lith}=0.0$ , $\theta = \text{constant}$ )

When  $Pe$  is large, the diffusion term can be neglected and the analytical solution for buoyant melt traveling up a sloping lithosphere is straightforward. Solving the resulting first order equation with the boundary condition of  $\phi = 0.0$  on the right hand side of the domain yields

$$\phi = \left[ \frac{-nw_{mantle}}{Pe \sin(\theta)}(x - L) \right]^{1/n} \quad (C20)$$

Comparison with a numerical solution where melt is allowed to flow through the left hand boundary and porosity is 0 on the right edge for  $n=1, 2$ , and  $3$  and  $w_{mantle}/Pe = 500$  results in RMS errors smaller than 0.00665.

Table C1  
Scaling Parameters

Parameter	Description	Value	Units
$g$	Acceleration of gravity	9.81	$\text{m s}^{-2}$
$k_0$	Reference permeability	$1 \times 10^{-10}$	$\text{m}^2$
$n$	Exponent on porosity in the permeability	2	-
$u_0$	Lateral melt flux scale	-	$\text{m s}^{-1}$
$w_{l0}$	Scale parameter for the melt flux through the lithosphere	$1 \times 10^{-14}$	$\text{m s}^{-1}$
$w_{m0}$	Scale parameter for the melt supply from the mantle	$8 \times 10^{-8}$	$\text{m s}^{-1}$
$w_{\text{mantle}}, w_{\text{lith}}$	Melt flux from below, melt flux through the lithosphere	-	-
$\alpha$	Coefficient of thermal expansion	$3.5 \times 10^{-5}$	$\text{J } ^\circ\text{C}^{-1} \text{ kg}^{-1}$
$\delta$	Length scale	1000	km
$\mu_m$	Melt viscosity	1	Pa s
$\theta$	Angle of the solidus measured clockwise from the horizontal	-	-
$\kappa$	Thermal diffusivity	$3 \times 10^{-6}$	$\text{m}^2 \text{ s}^{-1}$
$\Delta\rho$	Difference between solid and melt densities	500	$\text{kg m}^{-3}$
$\sigma_p, \sigma_{p0}$	Melt pressure beneath the solidus, melt pressure at reference porosity	- , 2e7	Pa
$\sigma_c$	Inherent strength of lithosphere (constant)	-	Pa
$\varphi, \varphi_0$	Porosity along the solidus, reference porosity	- , 0.1	-
$\varphi_{\text{coh}}$	Scaled lithospheric strength	2.2	-
$\Phi, \Phi_{\text{max}}$	Characteristic porosity of the lithosphere, maximum lithospheric porosity	-	-
$\tau$	Time scale	-	s
$\Delta z$	porosity diffusion length scale	-	m

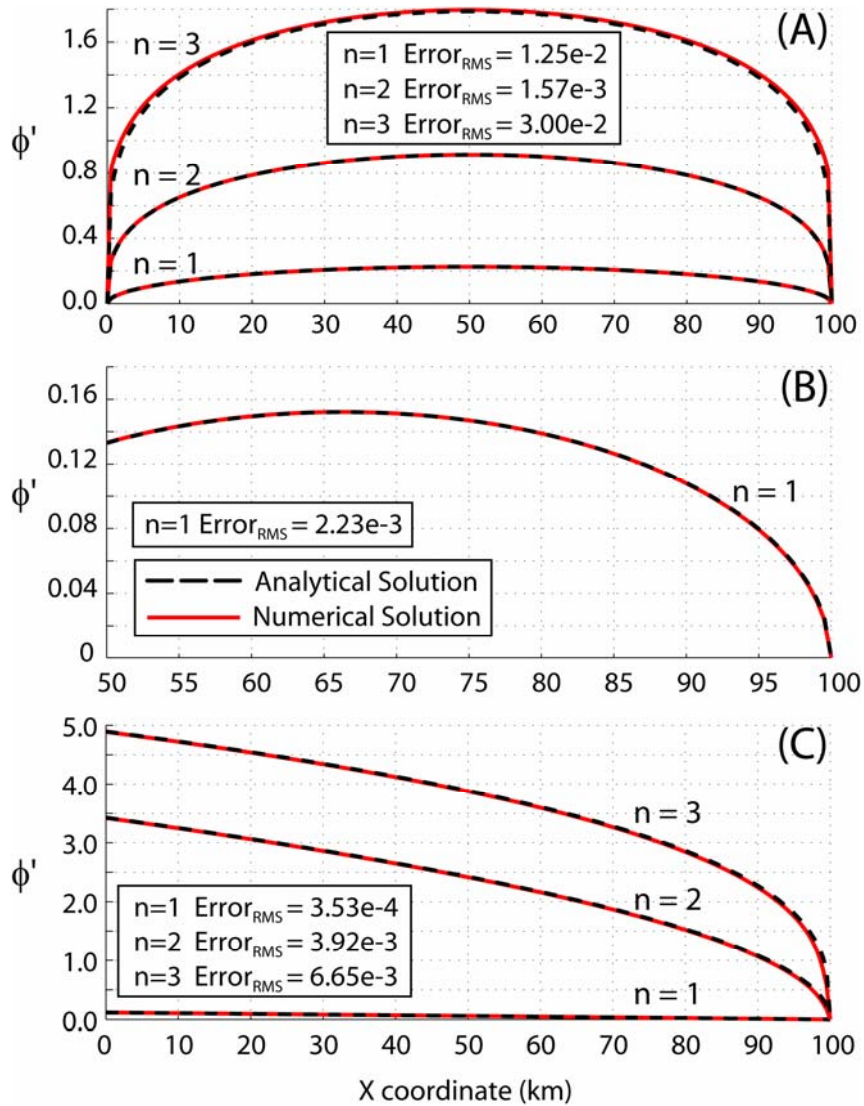


**Figure C1** (A) Comparisons of the dimensionless porosities between the analytical solution (dashed, black lines) and the numerical solution (red, solid lines; numerical grid spacing 0.5) for steady-state melt flow associated with gradients in porosity beneath a flat solidus and with the dimensionless porosity  $\phi'$  fixed at 0.0 on both ends. (B) Comparisons for a case with a fixed flux on the left-hand-side, a flat solidus, and  $\phi'$  fixed at 0.0 on the right-hand-side. The right half of the numerical domain is shown with the analytical solution shifted by 50 to the right for comparison. (C) Comparisons for a case dominated by buoyant melt flow up the slope of the solidus with  $w_{mantle}/Pe=$

500. In all cases, the errors shown are the root mean square of the difference between the analytical and numerical solutions divided by the maximum porosity of the analytical solution.

### 3. Melt Transport and Magma Flux Focusing

The following set of test cases examines the effects of the four principle parameters that control the porosity along the solidus as well as the where magma crosses the solidus and passes through the lithosphere:  $Pe$ ,  $D$ ,  $L_0$ , and  $S$ . Each section below describes an ideal case in which the solidus slope  $\theta$  and the melt supply from below  $w_{mantle}$  are held fixed.

#### 3.1 “Ridge-Axis” Solidus with a Gaussian Melt Flux from Below

In this section, I show the effect of  $Pe$  when the melt supply from below  $w_{mantle}$  varies laterally as a Gaussian function centered at  $x' = 30$  and the solidus slopes away from a central location similar to that of a ridge-axis (Figure C2C). Porosity is zero on the left and right edge in all cases. I examine two sets of cases: first, a case where magmatic damage is negligible ( $L_0=0$ ); and second, a case where  $w_{lith}$  is very sensitive to damage ( $L_0=1.25$ ) (C17). In the first case, the upslope flow of melt toward the ridge axis decreases with decreasing  $Pe$  because porosity gradients become more important in smoothing the local porosity high beneath the ridge axis (Figure C2A). For the second case, where  $w_{lith}$  is very sensitive to damage, high magma flux through the lithosphere at the center of the ridge axis locally drains melt and causes a dip in porosity (Figure

C2B). Decreasing  $Pe$  allows the steep gradients of the local dip to be smoothed by diffusion and enhance the melt flux through the lithosphere.

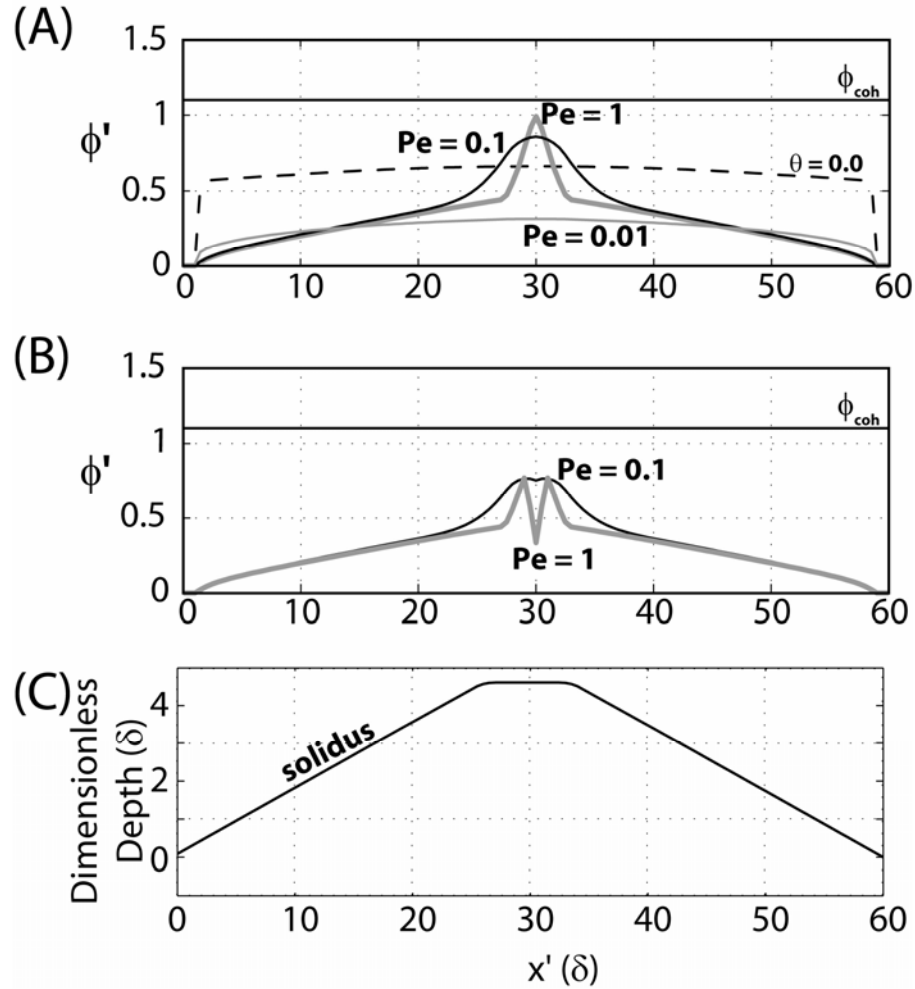


**Figure C2.** A set of cases with a steady melt supply from below  $w_{mantle}$ , both a flat solidus (dashed line) and a “ridge-axis” type sloped solidus, a melt flux that varies laterally in a Gaussian distribution centered at  $x' = 30$  (solid lines), and several values of Peclét number  $Pe$ . (A) Cases in which accumulated lithospheric damage by magmatism does not contribute to the vertical flux of melt ( $L_{\theta}=0.0$ ). (B) Cases where melt flux is very sensitive to the magmatic damage ( $L_{\theta}=1.25$ ). (C) The “ridge-axis” solidus used in the cases in (A) and (B) (absolute depth  $z'$  of the solidus is arbitrary and

does not affect the solutions, but its slope does). Horizontal, solid, black lines in (A) and (B) denote  $\phi_{coh}$ . The other parameters held constant for these cases are  $D = 0.313$ ,  $w_{l0}/w_{m0} = 7.84e4$ ,  $\phi_0 = 0.1$ ,  $H_0 = 1000$ ,  $S = 8e-5$ .

### 3.2 Uniformly Sloping Solidus with a Gaussian Melt Flux from Below

Here, I examine the porosity along a uniformly sloping solidus ( $10^\circ$ , down to the right) with a melt supply from below that varies as a Gaussian distribution centered at  $x' = 30$ . Melt is allowed to flow out the left hand side of the domain and the porosity  $\phi$  is set to zero on the right hand side. Accumulated magmatic damage is advected to the right at a constant plate velocity.

The region of magma flux through the lithosphere and the magnitude of that flux are strongly influenced by the sensitivity of lithospheric porosity to magmatic damage  $L_0$  and the healing rate scale  $S$ . Larger values of  $L_0$  cause a larger magma flux through the lithosphere for a smaller amount of accumulated magmatic damage (Figure C3). This larger magma flux then increases the rate of damage accumulation creating a positive feedback process that creates a localized peak in magma flux. A larger value of the healing rate scale also defines a larger maximum healing rate ( $S/H_0^2$ ) and results in a smaller region over which damage accumulates and a smaller value of the maximum magma flux (Figure C4). This reduction occurs because of a faster healing rate and because damage only accumulates over the region where magma flux  $w_{lith}$  surpasses the maximum healing rate ( $S/H_0^2$ ). For large  $L_0$ , the magma flux through the lithosphere can exceed that being supplied to a given point of the solidus (below and from the sides) and force a local decrease in porosity which (along with the advection of magmatic

damage at the plate velocity) causes the location of the peak magma flux to shift to the right toward zones of higher porosity (Figure C3). The peak in magma flux will continue (after 3Myr) to migrate to the right draining the melt from beneath the solidus until it passes out of the domain (out of the melting region).

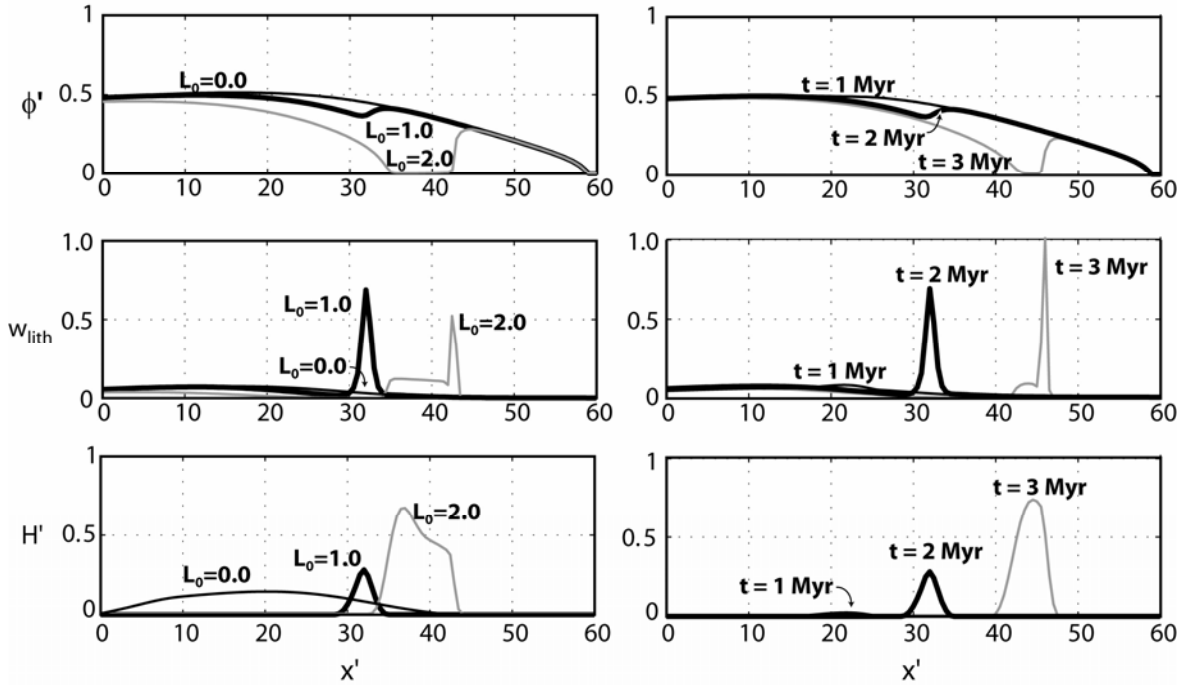


**Figure C3.** Two sets of cases where the solidus is sloping uniformly across the domain ( $10^\circ$ , down to the right). Porosity is set to 0.0 on the right boundary and melt is allowed to flow out the left boundary. (top row) Porosity is a strong function of the (middle row) melt flux through the lithosphere which increases with increasing values of (bottom row) magmatic damage. (left column) Cases showing the effect of three different values of  $L_0$  after 2 Myr. (right column) Porosity, melt flux and magmatic damage at three different times for  $L_0 = 1.0$ . The parameters held constant for these cases are  $Pe = 0.099$ ,  $D = 0.25$ ,  $w_{10}/w_{m0} = 7.84e4$ ,  $\phi_0 = 0.1$ ,  $H_0 = 1000$ ,  $S = 6.5e-6$ .

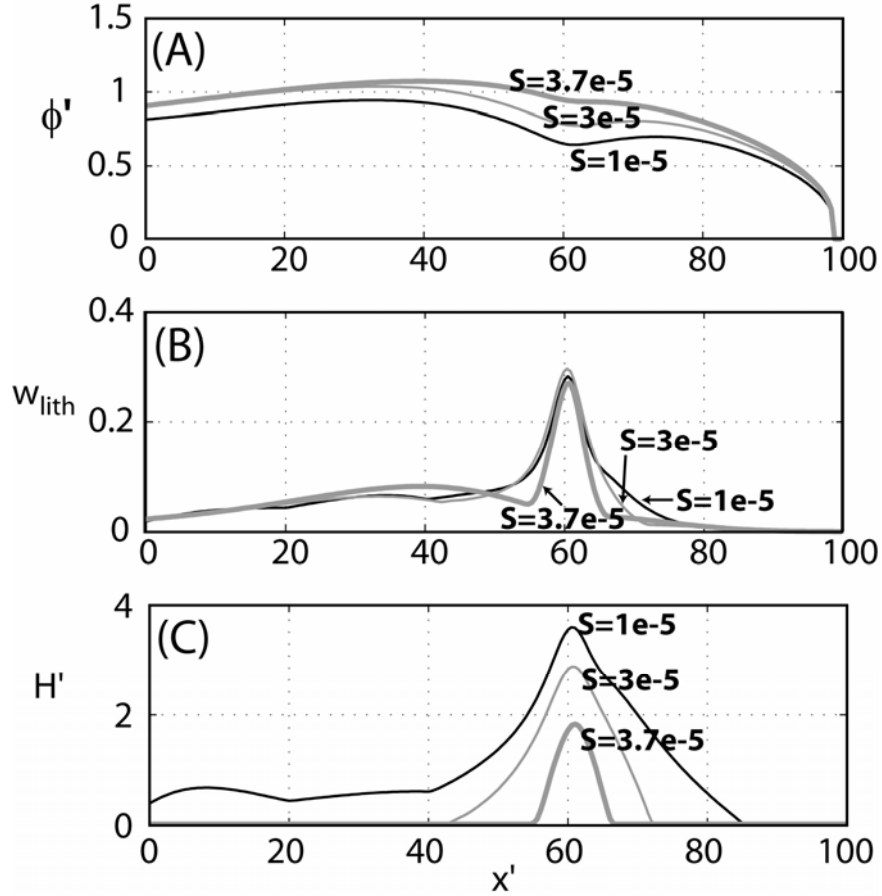


**Figure C4.** The (top) porosity, (middle) melt flux through the lithosphere, and the (bottom) time-integrated magmatic damage for a set of cases with a solidus slope and boundary conditions identical to the cases in figure C3. Variations in the healing rate  $S$  show that it controls the width of initial damage accumulation and the magnitude of the magma flux. The parameters held constant for these cases are  $Pe = 0.022$ ,  $D = 0.46$ ,  $w_{l0}/w_{m0} = 3924$ ,  $\phi_0 = 0.1$ ,  $H_0 = 1000$ ,  $L_0 = 0.167$ .

### 3.3 “Ridge-Axis” Solidus with a double-Gaussian Melt Flux from Below

In order to explore the behavior of a simple approximation to a hotspot near a ridge, as well as variations in the variable  $D$ , I present this final set of cases. The solidus is shallowest at a point centered at  $x' = 30$  and increases in depth as the square-

root of distance on either side of this point (Figure C5C). I approximate a “ridge and plume” melt flux from below as equal to the sum of two Gaussians centered at  $x' = 30$  and  $x' = 60$  (Figure C5D). For a range of parameters, the system produces a second, off-axis peak in magma flux, a necessary pre-requisite to initiate a ridge jump. The variable  $D$  controls the range of  $(\phi \cos(\theta) - \phi_{coh} + L_0 H)$  over which the melt flux  $w_{lith}$  varies from 0 to its maximum value  $(4\cos(\theta))$ . Larger values of  $D$  lead to a wider, less focused zone of magma flux through the lithosphere. Variations of  $L_0$  in these cases produce similar results as in section 3.2, but I show these results here to emphasize that these variables alter the focusing of magma flux at both the “ridge” and the “plume”.

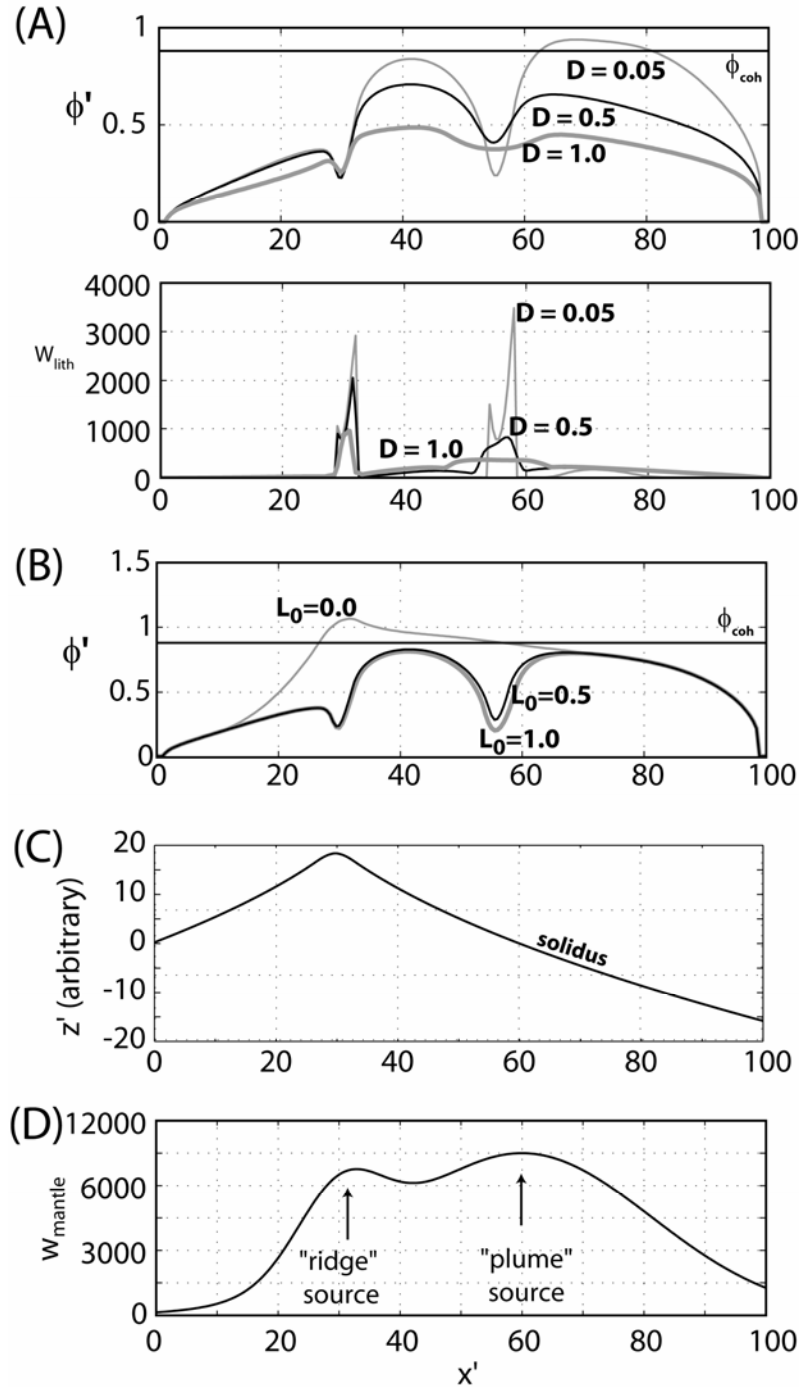


**Figure C5.** Cases with a (C) sloping solidus and a melt flux equal to the (D) sum of two Gaussian functions (a “ridge” and “plume” melt supply). (A) Variations in  $D$  control the range of porosity values for which magma can pass through the lithosphere. (B) Just as in figure A3, variations in  $L_0$  lead to different degrees of magmatic focusing

and reductions in the porosity. The parameters held constant for these cases are  $Pe = 0.0313$ , (B)  $D = 0.25$ ,  $w_{l0}/w_{m0} = 7.84e4$ ,  $\phi_0 = 0.1$ ,  $H_0 = 1000$ , (A)  $L_0 = 1.0$ .

## References Cited

- Allen, R. M., G. Nolet, W. J. Morgan, K. Vogfjord, M. Nettles, G. Ekstrom, B. H. Bergsson, P. Erlendsson, G. R. Foulger, S. Jakobsdottir, B. R. Julian, M. Pritchard, S. Ragnarsson, and R. Stefansson (2002), Plume-driven plumbing and crustal formation in Iceland, *J. Geophys. Res.*, *107* (B8).
- Asimow, P. D., J. E. Dixon, and C. H. Langmuir (2004), A hydrous melting and fractionation model for mid-ocean ridge basalts: Application to the Mid-Atlantic Ridge near the Azores, *Geochem. Geophys. Geosys.*, *5* (1).
- Asimow, P. D., M. M. Hirschmann, and E. M. Stolper (1997), An analysis of variations in isentropic melt productivity, *Philosophical Transactions of the Royal Society of London, Series A*, *355*, 255-281.
- Barber, J. R. (2002), *Elasticity*, pp. 185-187, Kluwer Academic Publishers.
- Behn, M. D., J. Lin, and M. T. Zuber (2002), Evidence for weak oceanic transform faults, *Geophys. Res. Lett.*, *29* (24), 2207.
- Bianco, T. A., G. Ito, J. van Hunen, and M. Ballmer (2007), Geochemical variations at a ridge-centered plume caused by variable melting of a veined mantle, *Eos Trans. AGU*, *88* (52), Fall Meet. Suppl., Abstract V33B-1389.
- Bianco, T. A., G. Ito, J. van Hunen, M. Ballmer, and J. Mahoney (2006), Geographic variations in hotspot geochemistry caused by 3D dynamics and melting of a heterogeneous mantle plume, *Eos Trans. AGU*, *87*(52), Fall Meet. Suppl., Abstract V13B-0667.
- Bohannon, R. G., and T. Parsons (1995), Tectonic implications of post-30 Ma Pacific and North American relative plate motions, *Geol. Soc. Amer. Bull.*, *107* (8), 937-959.
- Bonneville, A., J. P. Barriot, and R. Bayer (1988), Evidence from geoid data of a hotspot origin for the Southern Mascarene Plateau and Mascarene Islands (Indian Ocean), *J. Geophys. Res.*, *93* (B5), 4199 - 4212.
- Breivik, A. J., R. Mjelde, J. I. Faleide, and Y. Murai (2006), Rates of continental breakup magmatism and seafloor spreading in the Norway Basin - Iceland Plume interaction, *J. Geophys. Res.*, *111*, doi: 10.1029/2005JB004004.
- Briais, A., P. Patriat, and P. Tapponnier (1993), Updated interpretation of magnetic anomalies and seafloor spreading stages in the South China sea: implications for the Tertiary tectonics of Southeast Asia, *J. Geophys. Res.*, *98*, 6299-6328.
- Briais, A., and M. Rabinowicz (2002), Temporal variations of the segmentation of slow to intermediate spreading mid-ocean ridges 1. Synoptic observations based on satellite altimetry data, *J. Geophys. Res.*, *107* (B5).
- Brozena, J. M., and R. White (1990), Ridge jumps and propagations in the South Atlantic Ocean, *Nature*, *348*, p.149-152.
- Buck, W. R., and A. N. B. Poliakov (1998), Abyssal hills formed by stretching oceanic lithosphere, *Nature*, *392*, 272-275.
- Burov, E. B., and M. Diament (1995), The effective elastic thickness ( $T_e$ ) of continental lithosphere: What does it really mean?, *J. Geophys. Res.*, *100* (B3), 3905-3927.
- Canales, J. P., J. J. Danobeitia, R. S. Detrick, E. E. E. Hooft, R. Bartolome, and D. F. Naar (1997), Variations in axial morphology along the Galapagos spreading

- center and the influence of the Galapagos hotspot, *J. Geophys. Res.*, *102* (B12), 27,341-27,354.
- Canales, J. P., G. Ito, R. Detrick, and J. Sinton (2002), Crustal thickness along the western Galápagos Spreading Center and the compensation of the Galápagos hotspot swell, *Earth Planet. Sci. Lett.*, *203*, 311-327.
- Chen, Y., and W. J. Morgan (1990), A nonlinear rheology model for mid-ocean ridge axis topography, *J. Geophys. Res.*, *95* (B11), 17,583-17,604.
- Christensen, U. R. (1984), Convection with pressure- and temperature-dependent non-Newtonian rheology, *Geophys. J. R. Astron. Soc.*, *77*, 343-384.
- Christie, D. M., R. Werner, F. Hauff, K. Hoernle, and B. B. Hanan (2005), Morphological and geochemical variations along the eastern Galápagos Spreading Center, *Geochem. Geophys. Geosys.*, *6* (1), DOI:10.1029/2004GC000714.
- Coffin, M. F., M. S. Pringle, R. A. Duncan, T. P. Gladczenko, M. Storey, R. D. Muller, and L. A. Gahagan (2002), Kerguelen Hotspot magma output since 130Ma, *J. Petrol.*, *43* (7), 1121-1139.
- Cormier, M.-H., and K. C. Macdonald (1994), East Pacific Rise 18°-19°S: Asymmetric spreading and ridge reorientation by ultrafast migration of axial discontinuities, *J. Geophys. Res.*, *99* (B1), 543-564.
- Cosca, M. A., R. J. Arculus, J. A. Pearce, and J. G. Mirchell (1998), 40Ar/30Ar and K-Ar age constraints for the inception and early evolution of the Izu-Bonin-Mariana arc system, *The Island Arc*, *7*, 379-395.
- Crouch, S. L., and A. M. Starfield (1987), Boundary Element Methods in Solid Mechanics with applications in rock mechanics and geological engineering, pp. 45-47.
- Cullen, A., and A. R. McBirney (1987), The volcanic geology and petrology of Isla Pinta, Galapagos archipelago, *Geol. Soc. Amer. Bull.*, *98*, 294-301.
- Cundall, P. A. (1982), Adaptive density-scaling for time-explicit calculations, in *Int. Conf. Numerical Methods in Geomechanics*, pp. 23-26, Edmonton, Canada.
- Cushman, B., J. M. Sinton, and G. Ito (2004), Glass compositions, plume-ridge interaction, and hydrous melting along the Galapagos Spreading Center, 90.5°W to 98°W, *Geochemistry Geophysics Geosystems*, *5* (8).
- Darwin (1860), *The Voyage of the Beagle*, Penguin, USA.
- Davis, A. S., L. B. Gray, D. A. Clague, and J. R. Hein (2002), The Line Islands revisited: New <sup>40</sup>Ar/<sup>39</sup>Ar geochronological evidence for episodes of volcanism due to lithospheric extension, *Geochemistry Geophysics Geosystems*, *3* (2).
- Desa, M., M. V. Ramana, and T. Ramprasad (2006), Seafloor spreading magnetic anomalies south of Sri Lanka, *Marine Geology*, *229*, 227-240.
- Desonie, D. L., and R. A. Duncan (1990), The Cobb-Eickelberg Seamount Chain: Hotspot Volcanism with Mid-Ocean Ridge Basalt Affinity, *Journal of Geophysical Research*, *95* (B8), 12,697-12,711.
- Detrick, R., and S. T. Crough (1978), Island subsidence, hot spots, and lithospheric thinning, *J. Geophys. Res.*, *83*, 1236-1244.
- Detrick, R. S., J. M. Sinton, G. Ito, J. P. Canales, M. Behn, T. Blacic, B. Cushman, J. E. Dixon, D. W. Graham, and J. Mahoney (2002), Correlated geophysical,

- geochemical and volcanological manifestations of plume-ridge interaction along the Galápagos Spreading Center, *Geochem., Geophys., Geosys.*, 3(10), 8501, doi:10.1029/2002GC000350.
- Douglass, J., J. G. Schilling, and D. Fontignie (1999), Plume-ridge interactions of the Discovery and Shona mantle plumes with the southern Mid-Atlantic Ridge (40° - 55°S), *Journal of Geophysical Research*, 104 (B2), 2941-2962.
- Duncan, R. A. (1984), Age Progressive Volcanism in the New England Seamounts and the Opening of the Central Atlantic Ocean, *Journal of Geophysical Research*, 89 (B12), 9,980-9,990.
- Dyment, J. (1998), Evolution of the Carlsberg Ridge between 60 and 45 Ma: Ridge propagation, spreading asymmetry, and the Deccan-Reunion hotspot, *J. Geophys. Res.*, 103, 24,067-24,084.
- Ernst, R. E., and K. L. Buchan (1997), Giant radiating dyke swarms: Their use in identifying pre-Mesozoic large igneous provinces and mantle plumes, in *Large Igneous Provinces: Continental, Oceanic, and Planetary Flood Volcanism*, edited by J. Mahoney, and M.F. Coffin, AGU, Washington D.C.
- Faccenna, C., F. Funiciello, D. Giardini, and P. Lucente (2001), Episodic back-arc extension during restricted mantle convection in the Central Mediterranean, *Earth Planet. Sci Lett.*, 187, 105-116.
- Feighner, M. A., and M. A. Richards (1994), Lithospheric structure and compensation mechanisms of the Galapagos Archipelago, *J. Geophys. Res.*, 99 (B4), 6711-6729.
- Forsyth, D., and S. Uyeda (1975), On the Relative Importance of the Driving Forces of Plate Motion, *Geophys. J. R. Astron. Soc.*, 43, 163-200.
- Garcia, S., N. Arnaud, J. Angelier, F. Bergerat, and C. Homberg (2003), Rift jump processes in Northern Iceland since 10 Ma from 40Ar/39Ar geochronology, *Earth Planet. Sci Lett.*, 214, 529-544.
- Geist, D., A. R. McBirney, and R. A. Duncan (1986), Geology and petrogenesis of lavas from San Cristobal Island, Galapagos Archipelago, *Geol. Soc. Amer. Bull.*, 97, 555-566.
- Geist, D., W. White, T. Naumann, and R. Reynolds (1999), Illegitimate magmas of the Galapagos: Insights into mantle mixing and magma transport, *Geology*, 27 (12), 1103-1106.
- Geldmacher, J., and K. Hoernle (2000), The 72 Ma geochemical evolution of the Madeira hotspot (eastern North Atlantic): recycling of Paleozoic ( $\leq 500$  Ma) oceanic lithosphere, *Earth and Planetary Science Letters*, 183, 73-92.
- Geli, L., D. Aslanian, J. Olivet, I. Vlastelic, L. Dosso, H. Guillou, and H. Bougault (1998), Location of the Louisville hotspot and origin of Hollister Ridge: geophysical constraints, *Earth and Planetary Science Letters*, 164, 31-40.
- Glen, J. M. G., and D. A. Ponce (2002), Large-scale fractures related to inception of the Yellowstone hotspot, *Geology*, 30 (7), 647-650.
- Goetze, C., and B. Evans (1979), Stress and temperature in the bending lithosphere as constrained by experimental rock mechanics, *Geophys. J. R. Astron. Soc.*, 59, 463-478.
- Gould, P. L. (1988), *Analysis of Shells and Plates*, Springer-Verlag.

- Gudmundsson, A. (1995), Stress fields associated with oceanic transform faults, *Earth Planet. Sci Lett.*, 136, 603-614.
- Hall, P. S., and C. Kincaid (2003), Melting, dehydration and the dynamics of off-axis plume-ridge interaction, *Geochem. Geophys. Geosys.*, 4 (9), 10.1029/2003GC000567.
- Hall, P. S., and C. Kincaid (2004), Melting, dehydration, and the geochemistry of off-axis plume-ridge interaction, *Geochem. Geophys. Geosys.*, 5 (12), 10.1029/2003GC000667.
- Hanan, B. B., J. Blichert-Toft, R. H. Kingsley, and J.-G. Schilling (2000), Depleted Iceland mantle plume geochemical signature: Artifact of multicomponent mixing?, *Geochem., Geophys., Geosys.*, 1.
- Hanan, B. B., R. H. Kingsley, and J.-G. Schilling (1986), Pb isotope evidence in the South Atlantic for migrating ridge-hotspot interactions, *Nature*, 322.
- Hardarson, B. S., J. G. Fitton, R. M. Ellam, and M. S. Pringle (1997), Rift relocation - a geochemical and geochronological investigation of a paleo-rift in northwest Iceland, *Earth Planet. Sci Lett.*, 153, 181-196.
- Harpp, K., D. J. Fornari, D. Geist, and M. D. Kurz (2003), Genovesa Submarine Ridge: A manifestation of plume-ridge interaction in the northern Galapagos Islands, *Geochem., Geophys., Geosys.*, 4 (9).
- Harpp, K., and D. Geist (2002), Wolf-Darwin lineament and plume-ridge interaction in northern Galapagos, *Geochem., Geophys., Geosys.*, 3 (11), 1-19.
- Harpp, K., and R. White (2001), Tracing a mantle plume: Isotopic and trace element variations of Galapagos seamounts, *Geochem. Geophys. Geosys.*, 2, DOI:2000GC000137.
- Hekinian, R., P. Stoffers, D. Ackermann, S. Revillon, M. Maia, and M. Bohn (1999), Ridge-hotspot interaction: the Pacific-Antarctic Ridge and the foundation seamounts, *Marine Geology*, 160, 199-223.
- Hess, H. H. (1962), History of ocean basins, in *Petrologic Studies*, pp. 599, Geological Society of America, New York.
- Hey, R. N. (1977), Tectonic evolution of the Coco-Nazca spreading center, *Geol. Soc. Amer. Bull.*, 88, 1404-1420.
- Hey, R. N. (1998), Speculative propagating rift-subduction zone interactions with possible consequences for continental margin evolution, *Geology*, 26 (3), 247-250.
- Hieronymus, C. F., and D. Bercovici (2001), A theoretical model of hotspot volcanism: Control on volcanic spacing and patterns via magma dynamics and lithospheric stresses, *J. Geophys. Res.*, 106 (B1), 683-702.
- Hirth, G., and D. L. Kohlstedt (1995a), Experimental constraints on the dynamics of the partially molten upper mantle, 2. Deformation in the dislocation creep regime, *J. Geophys. Res.*, 100, 15,441-15,449.
- Hirth, G., and D. L. Kohlstedt (1995b), Experimental constraints on the dynamics of the partially molten upper mantle: Deformation in the diffusion creep regime, *J. Geophys. Res.*, 100, 1981-2001.
- Hirth, G., and D. L. Kohlstedt (1996), Water in the oceanic upper mantle: Implications for rheology, melt extraction, and the evolution of the lithosphere, *Earth Planet. Sci Lett.*, 144, 93-108.

- Huppert, H. (1982), The propagation of two-dimensional and axisymmetric viscous gravity currents over a rigid horizontal surface, *J. Fluid Mech.*, *121*, 43-58.
- Hussong, D. M., and S. Uyeda (1981), 54. Tectonic processes and the history of the Mariana Arc: A synthesis of the results of Deep Sea Drilling Project Leg 60, *Init. Rep DSDP*, *60*, 909-929.
- Ito, G. (2001), Reykjanes 'V'-shaped ridges originating from a pulsing and dehydrating mantle plume, *Nature*, *411*, 681-684.
- Ito, G., and J. Lin (1995), Oceanic spreading center-hotspot interactions: Constraints from along-isochron bathymetric and gravity anomalies, *Geology*, *23*, 657-660.
- Ito, G., J. Lin, and C. W. Gable (1997), Interaction of mantle plumes and migrating mid-ocean ridges: Implications for the Galapagos plume-ridge system, *J. Geophys. Res.*, *102* (B7), 15,403-15,417.
- Ito, G., J. Lin, and D. Graham (2003), Observational and theoretical studies of the dynamics of mantle plume-mid-ocean ridge interaction, *Rev. Geophys.*, *41* (4), 1017, doi:10.1029/2002RG000117.
- Ito, G., and J. Mahoney (2005), Flow and melting of a heterogeneous mantle: 1. Method and importance to the geochemistry of ocean island and mid-ocean ridge basalts, *Earth Planet. Sci Lett.*, *230*, 29-46.
- Jellinek, A. M., H. M. Gonnermann, and M. A. Richards (2003), Plume capture by divergent plate motions: Implications for the distribution of hotspots, geochemistry of mid-ocean ridge basalts, and heat flux at the core-mantle boundary, *Earth Planet. Sci Lett.*, *205*, 361-378.
- Jóhannesson, H. (1980), Jarðlagaskipan og þróun rekkelta á Vesturlandi (Evolution of rift zones in western Iceland), *Náttúrufræðingurinn*, *50* (1), 13-31.
- Jones, S. M. (2003), Test of a ridge-plume interaction model using oceanic crustal structure around Iceland, *Earth Planet. Sci Lett.*, *208* (3-4), 205-218.
- Jones, S. M., N. White, and J. Maclennan (2002), V-shaped ridges around Iceland: Implications for spatial and temporal patterns of mantle convection, *Geochem. Geophys. Geosys.*, *3* (10), 10.1029/2002GC000361.
- Jurine, D., C. Jaupart, G. Brandeis, and P. J. Tackley (2005), Penetration of mantle plumes through depeleted lithosphere, *J. Geophys. Res.*, *110*, 10.1029/2005JB003751.
- Karsten, J. L., S. R. Hammond, E. E. Davis, and R. G. Currie (1986), Detailed geomorphology and neotectonics of the Endeavour Segment, Juan de Fuca Ridge: New results from Seabeam swath mapping, *Geol. Soc. Amer. Bull.*, *97* (2), 213-221.
- Katz, R. F., M. Spiegelan, and C. H. Langmuir (2003), A new parameterization of hydrous mantle melting, *Geochem. Geophys. Geosys.*, *4* (9), doi:10.1029/2002GC000433.
- Kelemen, P. B., K. Koga, and N. Shimizu (1997), Geochemistry of gabbro sills in the crust-mantle transition zone of the Oman ophiolite: implications for the origin of the oceanic lower crust, *Earth Planet. Sci Lett.*, *146*, 475-488.
- Keller, R. A., M. R. Fisk, and W. M. White (2000), Isotopic evidence for Late Cretaceous plume-ridge interaction at the Hawaiian hotspot, *Nature*, *405*.
- Kendall, J. M., G. W. Stuart, C. J. Ebinger, I. D. Bastow, and D. Keir (2005), Magma-assisted rifting in Ethiopia, *Nature*, *433*, p.146-148.

- Kincaid, C., J.-G. Schilling, and C. W. Gable (1996), The dynamics of off-axis plume-ridge interaction in the uppermost mantle, *Earth Planet. Sci Lett.*, *137*, 29-43.
- Kopp, H., C. Kopp, J. P. Morgan, E. R. Flueh, W. Weinrebe, and W. J. Morgan (2003), Fossil hot spot-ridge interaction in the Musicians Seamount Province: Geophysical investigations of hot spot volcanism at volcanic elongated ridges, *J. Geophys. Res.*, *108* (B3).
- Krishna, K. S., and D. G. Rao (2000), Abandoned Paleocene spreading center in the northeastern Indian Ocean: evidence from magnetic and seismic reflection data, *Marine Geology*, *162*, 215-224.
- Krishna, K. S., D. G. Rao, M. V. Ramana, V. Subrahmanyam, K. V. L. N. S. Sarma, A. I. Pilipenko, V. S. Shcherbakov, and I. V. Radhakrishna Murthy (1995), Tectonic model for the evolution of oceanic crust in the northeastern Indian Ocean from the Late Cretaceous to the early Tertiary, *J. Geophys. Res.*, *100* (B10), 20011-20024.
- LaFemina, P. C., T. H. Dixon, R. Malservisi, T. Arnadottir, E. Sturkell, F. Sigmundsson, and P. Einarsson (2005), Geodetic GPS measurements in south Iceland: Strain accumulation and partitioning in a propagating ridge system, *J. Geophys. Res.*, *110*, 10.1029/2005JB003675.
- Lavier, L. L., and W. R. Buck (2002), Half graben versus large-offset low-angle normal fault: Importance of keeping cool during normal faulting, *J. Geophys. Res.*, *107* (B6), 10.1029/2001JB000513.
- Li, X., R. Kind, X. Yuan, I. Wolbern, and W. Hanka (2004), Rejuvenation of the lithosphere by the Hawaiian plume, *Nature*, *427*, doi:10.1038/nature02349.
- Lonsdale, P. (1988), Geography and History of the Louisville Hotspot Chain in the Southwest Pacific, *J. Geophys. Res.*, *93* (B4), 3078-3104.
- Macdonald, G. A. (1998), Linkages between faulting, volcanism, hydrothermal activity and segmentation on fast spreading centers, in *Faulting and Magmatism at Mid-Ocean Ridges*, edited by W.R. Buck, J.R. Delaney, J.A. Karson, and Y. Lagabriele, AGU, Washington D.C.
- Macdonald, G. A., D. S. Scheirer, and S. M. Carbotte (1991), Mid-ocean ridges: Discontinuities, segments and giant cracks, *Science*, *253*, 986-994.
- Macdonald, K. C., P. J. Fox, L. J. Perram, M. F. Eisen, R. M. Haymon, S. P. Miller, S. M. Carbotte, M.-H. Cormier, and A. N. Shor (1988), A new view of the mid-ocean ridge from the behaviour of ridge-axis discontinuities, *Nature*, *335*.
- Mackwell, S. J., M. E. Zimmerman, and D. L. Kohlstedt (1998), High-temperature deformation of dry diabase with application to tectonics on Venus, *J. Geophys. Res.*, *103* (B1), 975-984.
- Maclennan, J., D. McKenzie, K. Gronvöld, and L. Slater (2001), Crustal accretion under northern Iceland, *Earth Planet. Sci Lett.*, *191*, 295-310.
- Magde, L. S., and D. W. Sparks (1997), Three-dimensional mantle upwelling, melt generation, and melt migration beneath slow-spreading ridges, *J. Geophys. Res.*, *102* (B9), 20571-20583.
- Mammerickx, J., and D. T. Sandwell (1986), Rifting of old oceanic lithosphere, *J. Geophys. Res.*, *91*, 1975-1988.
- McBirney, A. R., and Williams (1969), *Geology and Petrology of the Galapagos Islands*, Geol. Soc. Am., Boulder.

- McKenzie, D. (1984), The generation and compaction of partially molten rock, *J. Petrol.*, 25, 713-765.
- Mittelstaedt, E., and G. Ito (2005), Plume-ridge interaction, lithospheric stresses, and the origin of near-ridge volcanic lineaments, *Geochem., Geophys., Geosys.*, 6 (6), 10.1029/2004GC000860.
- Mittelstaedt, E., G. Ito, and M. Behn (2008), Mid-ocean ridge jumps associated with hotspot magmatism, *Earth Planet. Sci Lett.*, 266 (3-4), doi:10.1016/j.epsl.2007.10.055.
- Mjelde, R., A. J. Breivik, T. Raum, E. Mittelstaedt, G. Ito, and J. I. Faleide (2008), Magmatic and tectonic evolution of the North Atlantic, *Journal of the Geological Society*, 165 (165), doi:10.1144/0016-76492007-018.
- Moore, W. B., G. Schubert, and P. Tackley (1998), Three-Dimensional Simulations of Plume-Lithosphere Interaction at the Hawaiian Swell, *Science*, 279.
- Moresi, L., and V. S. Solomatov (1995), Numerical investigation of 2D convection with extremely large viscosity variations, *Physics of Fluids*, 7 (9), 2154-2162.
- Morgan, W. J. (1971), Convection plumes in the lower mantle, *Nature*, 230, 42-43.
- Morgan, W. J. (1978), Rodriguez, Darwin, Amsterdam...A Second Type of Hotspot Island, *J. Geophys. Res.*, 83 (B11), 5355-5360.
- Muller, J. R., G. Ito, and S. J. Martel (2001a), Effects of volcano loading on dike propagation in an elastic half-space, *J. Geophys. Res.*, 106 (B6), 11,101-11,113.
- Muller, O., and D. Pollard (1977), The state of stress near Spanish Peaks, Colorado, determined from a dike pattern., *Pure and Applied Geophysics*, 115, 69-86.
- Muller, R. D., C. Gaina, W. R. Roest, and D. L. Hansen (2001b), A recipe for microcontinent formation, *Geology*, 29 (3), 203-206.
- Muller, R. D., W. R. Roest, and J. Royer (1998), Asymmetric sea-floor spreading caused by ridge-plume interactions, *Nature*, 396, 455-459.
- Muller, R. D., W. R. Roest, J. Royer, and L. A. Gahagan (1997), Digital Isochrons of the world's ocean floor, *J. Geophys. Res.*, 102 (B2), 3211-3214.
- Muller, R. D., J. Royer, and L. A. Lawver (1993), Revised plate motions relative to the hotspots from combined Atlantic and Indian Ocean hotspot tracks, *Geology*, 21, 275-278.
- Muller, R. D., M. Sdrolias, C. Gaina, and W. R. Roest (2008), Age, spreading rates, and spreading asymmetry of the world's ocean crust, *Geochem. Geophys. Geosys.*, 9 (doi:10.1029/2007GC001743).
- Nadin, P. A., N. J. Kusznir, and J. Toth (1995), Transient regional uplift in the Early Tertiary of the northern North Sea and the development of the Iceland Plume, *J. Geol. Soc. Lon.*, 152, 953-958.
- Nakanishi, M., W. W. Sager, and A. Klaus (1999), Magnetic lineations within Shatsky Rise, northwest Pacific Ocean: Implications for hotspot-triple junction interaction and oceanic plateau formation, *J. Geophys. Res.*, 104 (B4), p.7539-7556.
- Nicholson, C., C. C. Sorlien, T. Atwater, J. C. Crowell, and B. P. Luyendyk (1994), Microplate capture, rotation of the western Transverse Ranges, and initiation of the San Andreas transform as a low-angle fault system, *Geology*, 22, 491-495.

- Nielsen, T. K., H. C. Larsen, and J. R. Hopper (2002), Contrasting rifted margin styles south of Greenland: Implications for mantle plume dynamics, *Earth Planet. Sci Lett.*, *200*, 271-286.
- Novozhilov, V. V. (1959), *The Theory of Thin Shells*, 376 pp., P. Noordhoff LTD., Groningen.
- O'Connor, J. M., and R. A. Duncan (1990), Evolution of the Walvis Ridge-Rio Grande Rise Hot Spot System: Implications for African and South American Plate Motions Over Plumes, *J. Geophys. Res.*, *95* (B11), 17,475-17,502.
- O'Connor, J. M., and A. P. Roex (1992), South Atlantic hot spot-plume systems: 1. Distribution of volcanism in time and space, *Earth Planet. Sci Lett.*, *113*, 343-364.
- O'Connor, J. O., P. Stoffers, and M. O. McWilliams (1995), Time-space mapping of Easter Chain volcanism, *Earth and Planetary Science Letters*, *136*, 195-212.
- Ode, H. (1957), Mechanical Analysis of the Dike Pattern of the Spanish Peaks Area, Colorado, *Geol. Soc. Amer. Bull.*, *68*, 567-576.
- Olson, P. (1990), Hot spots, swells and mantle plumes, in *Magma Transport and Storage*, edited by M.P. Ryan, John Wiley and Sons Ltd.
- Pariso, J. E., J. C. Sempere, and C. Rommevaux (1995), Temporal and spatial variations in crustal accretion along the Mid-Atlantic Ridge (29°- 31°30'N) over the last 10 m.y.: Implications from a three-dimensional gravity study, *J. Geophys. Res.*, *100* (B9), 17,781-17,794.
- Parsons, B., and J. G. Sclater (1977), An analysis of the variation of ocean floor bathymetry and heat flow with age, *J. Geophys. Res.*, *82*, 803-827.
- Phipps Morgan, J., and E. M. Parmentier (1985), Causes and rate-limiting mechanisms of ridge propagation: a fracture mechanics model, *J. Geophys. Res.* (B10), 8603-8612.
- Poliakov, A. N. B., and W. R. Buck (1998), Mechanics of stretching elastic-plastic-viscous layers: Applications to slow-spreading mid-ocean ridges, in *Faulting and Magmatism at Mid-Ocean Ridges*, edited by W.R. Buck, P.T. Delaney, J.A. Karson, and Y. Lagabriele, pp. 305-323, AGU, Washington D. C.
- Poliakov, A. N. B., P. A. Cundall, Y. Y. Podladchikov, and V. A. Lyakhovskiy (1993), An explicit inertial method for the simulation of viscoelastic flow: An evaluation of elastic effects on diapiric flow in two and three layers models, in *Flow and Creep in the Solar System: Observations, Modeling and Theory*, edited by S.K. Runcorn, pp. 175-195, Kluwer Academic Publishers, Netherlands.
- Pollard, D., and A. Aydin (1988), Progress in understanding jointing over the past century, *Geol. Soc. Amer. Bull.*, *100*, 1181-1204.
- Pollard, D. D., and A. Aydin (1984), Propagation and linkage of oceanic ridge segments, *J. Geophys. Res.*, *89*, 10017-10028.
- Reinecker, J., O. Heidbach, M. Tingay, P. Connolly, and B. Muller (2004), The 2004 release of the World Stress Map (available online at [www.world-stress-map.org](http://www.world-stress-map.org)).
- Ribe, N. M. (1996), The dynamics of plume-ridge interaction 2. Off-ridge plumes, *J. Geophys. Res.*, *101* (B7), 16,195-16,204.

- Ribe, N. M., and U. R. Christensen (1994), Three-dimensional modelling of plume-lithosphere interaction, *J. Geophys. Res.*, *99*, 669-682.
- Ribe, N. M., and W. L. Delattre (1998), The dynamics of plume-ridge interaction, 3: The effects of ridge migration, *Geophysical Journal International*, *133*, 511-518.
- Richards, M. A., B. H. Hager, and N. Sleep (1988), Dynamically Supported Geoid Highs Over Hotspots: Observation and Theory, *J. Geophys. Res.*, *93* (B7), 7690-7708.
- Sæmundsson, K. (1974), Evolution of the axial rifting zone in Northern Iceland and the Tjörnes Fracture Zone, *Geol. Soc. Amer. Bull.*, *85*, 495-504.
- Schilling, J.-G. (1991), Fluxes and excess temperatures of mantle plumes inferred from their interaction with migrating mid-ocean ridges, *Nature*, *352*, 397-403.
- Schilling, J.-G., D. Fontignie, J. Blichert-Toft, R. Kingsley, and U. Tomza (2003), Pb-Hf-Nd-Sr isotope variations along the Galapagos Spreading Center (101-83W): Constraints on the dispersal of the Galapagos mantle plume, *Geochem., Geophys., Geosys.*, *4* (10).
- Schubert, G., and R. N. Hey (1986), Mantle Viscosity Beneath The Galapagos 95.5°W Propagating Rift, *Geophys. Res. Lett.*, *13* (4), 329-332.
- Sdrolias, M., W. R. Roest, and R. D. Muller (2004), An expression of Philippine Sea plate rotation: the Parece Vela and Shikoku Basins, *Tectonophysics*, *394*, 69-86.
- Searle, R. C., P. A. Cowie, N. C. Mitchell, S. Allerton, C. J. MacLeod, J. Escartin, S. M. Russell, P. A. Slootweg, and T. Tanaka (1998), Fault structure and detailed evolution of a slow spreading ridge segment: the Mid-Atlantic Ridge at 29°N, *Earth Planet. Sci Lett.*, *154*, 167-183.
- Sempéré, J. C., P. Blondel, A. Briais, T. Fujiwara, L. Geli, N. Isezaki, J. E. Pariso, L. Parson, P. Patriat, and C. Rommevaux (1995), The Mid-Atlantic Ridge between 29°N and 31°30'N in the last 10 Ma, *Earth Planet. Sci Lett.*, *130*, 45-55.
- Shaw, W. J., and J. Lin (1996), Models of ocean ridge lithospheric deformation: Dependence on crustal thickness, spreading rate, and segmentation, *J. Geophys. Res.*, *101* (B8), 17,977-17,993.
- Sibuet, J. C., S. K. Hsu, X. Le Pichon, J. P. Le Formal, T. B. Reed, G. Moore, and C. S. Liu (2002), East Asia plate tectonics since 15Ma: constraints from the Taiwan Region, *Tectonophysics*, *344*, 103-134.
- Sinton, C. W., D. M. Christie, and R. A. Duncan (1996), Geochronology of Galapagos Seamounts, *J. Geophys. Res.*, *101* (B6), 13689-13700.
- Sinton, J. M., and R. S. Detrick (1992), Mid-ocean ridge magma chambers, *J. Geophys. Res.*, *97*, 197-216.
- Sinton, J. M., R. S. Detrick, J. P. Canales, G. Ito, and M. Behn (2003), Morphology and Segmentation of the Western Galapagos Spreading Center, 90.5 - 98 W: Plume-Ridge Interaction at an Intermediate Spreading Ridge, *Geochem., Geophys., Geosys.*, *4* (12).
- Sleep, N. (1990), Hotspots and Mantle Plumes: Some Phenomenology, *J. Geophys. Res.*, *95* (B5), 6715 - 6736.
- Sleep, N. (2002), Ridge-crossing mantle plumes and gaps in tracks, *Geochem., Geophys., Geosys.*, *3* (12), 10.1029/2001GC000290.

- Small, C. (1995), Observations of ridge-hotspot interactions in the Southern Ocean, *J. Geophys. Res.*, *100*, 17931-17946.
- Smith, W. H. F., and D. T. Sandwell (1994), Bathymetric prediction from dense satellite altimetry and sparse shipboard bathymetry, *J. Geophys. Res.*, *99*, 21,803-21,824.
- Smith, W. H. F., and D. T. Sandwell (1997), Global seafloor topography from satellite altimetry and ship depth soundings, *Science*, *277*, 1957-1962.
- Sonne, S. P. o. c. S.-o. F. S. (1990), Active Pitcairn hotspot found, *Marine Geology*, *95*, 51-55.
- Sparks, D. W., and E. M. Parmentier (1991), Melt extraction from the mantle beneath spreading centers, *Earth Planet. Sci Lett.*, *105*, 368-377.
- Sparks, D. W., and E. M. Parmentier (1994), The generation and migration of partial melt beneath oceanic spreading centers, in *Magmatic Systems*, edited by M.P. Ryan, Academic Press.
- Spiegelman, M. (1993), Physics of melt extraction: Theory, implications and applications, *Philosophical Transactions of the Royal Society of London, Series A*, *342*, 23-41.
- Spiegelman, M., and D. McKenzie (1987), Simple 2-D models for melt extraction at mid-ocean ridges and island arcs, *Earth Planet. Sci Lett.*, *83*, 137-152.
- Steckler, M. S., and U. tenBrink (1986), Lithospheric strength variations as a control on new plate boundaries: Examples from the northern Red Sea region, *Earth Planet. Sci Lett.*, *79*, 120-132.
- Stein, C. A., and S. Stein (1992), A model for the global variation in oceanic depth and heat flow with lithospheric age, *Nature*, *359*.
- Taylor, B. (1992), Rifting and the volcanic-tectonic evolution of the Izu-Bonin-Mariana arc, in *Proc. Ocean Drilling Program, Sci. Res.*, edited by B. Taylor, et al., pp. 627-651, ODP, College Station, TX.
- Taylor, R. N., B. J. Murton, and M. F. Thirwall (1995), Petrographic and geochemical variation along the Reykjanes Ridge, 57<sup>0</sup>N - 59<sup>0</sup>N, *J. Geol. Soc. Lon.*, *152*, 1031-1037.
- tenBrink, U. (1991), Volcano spacing and plate rigidity, *Geology*, *19*, 397-400.
- Timoshenko, S. P., and J. N. Goodier (1934), *Theory of Elasticity*, pp. 127-132, McGraw Hill.
- Torsvik, T. H., J. Mosar, and E. A. Eide (2001), Cretaceous-Tertiary geodynamics: A North Atlantic exercise, *Geophys. J. Int.*, *146*, 850-867.
- Turcotte, D. L., and G. Schubert (2002), *Geodynamics*, 456 pp., Cambridge University Press, Cambridge.
- Vlastelic, I., L. Dosso, H. Guillou, H. Bougault, L. Geli, J. Etoubleau, and J. L. Joron (1998), Geochemistry of the Hollister Ridge: relation with the Louisville hotspot and the Pacific-Antarctic Ridge, *Earth and Planetary Science Letters*, *160*, 777-793.
- Vogt, P. R. (1971), Asthenosphere motion recorded by the ocean floor south of Iceland, *Earth Planet. Sci Lett.*, *13*, 153-160.
- Weis, D., F. Frey, R. Schlich, M. Schaming, R. Montigny, D. Damasceno, N. Mattielli, K. E. Nicolaysen, and J. S. Scoates (2002), Trace of the Kerguelen mantle plume: Evidence from seamounts between the Kerguelen Archipelago and Heard Island, Indian Ocean, *Geochemistry Geophysics Geosystems*, *3* (6).

- Werner, R., K. Hoernle, U. Barckhausen, and F. Hauff (2003), Geodynamic evolution of the Galapagos hot spot system (Central East Pacific) over the past 20 m.y.: Constraints from morphology, geochemistry, and magnetic anomalies, *Geochem., Geophys., Geosys.*, 4 (12).
- Westaway, R. (1993), Forces associated with mantle plumes, *Earth Planet. Sci Lett.*, 119, 331-348.
- White, R., D. McKenzie, and K. O'Nions (1992), Oceanic Crustal Thickness From Seismic Measurements and Rare Earth Element Inversions, *J. Geophys. Res.*, 97 (B13), 19683-19715.
- White, W. M., A. R. McBirney, and R. A. Duncan (1993), Petrology and Geochemistry of the Galapagos Islands: Portrait of a Pathological Mantle Plume, *J. Geophys. Res.*, 98 (B11), 19533-19563.
- Wilson, D. S., and R. N. Hey (1995), History of rift propagation and magnetization intensity for the Cocos-Nazca spreading center, *J. Geophys. Res.*, 100 (B6), 10,041-10,056.
- Wolfe, C., P. G. Okubo, G. Ekstrom, M. Nettles, and P. M. Shearer (2004), Characteristics of deep (>13km) Hawaiian earthquakes and Hawaiian earthquakes west of 155.55°W, *Geochem. Geophys. Geosys.*, 5 (4).
- Zhong, S., M. T. Zuber, L. Moresi, and M. Gurnis (2000), Role of temperature-dependent viscosity and surface plates in spherical shell models of mantle convection, *J. Geophys. Res.*, 105 (B5), 11063-11082.